

**CHARACTERISATION OF DRAWING PARAMETERS
FOR FABRICATION OF FLAT FIBERS**

KATRINA D. DAMBUL

**FACULTY OF ENGINEERING
UNIVERSITY OF MALAYA
KUALA LUMPUR**

2018

**CHARACTERISATION OF DRAWING PARAMETERS
FOR FABRICATION OF FLAT FIBERS**

KATRINA D. DAMBUL

**THESIS SUBMITTED IN FULFILMENT OF THE
REQUIREMENTS FOR THE DEGREE OF DOCTOR OF
PHILOSOPHY**

**FACULTY OF ENGINEERING
UNIVERSITY OF MALAYA
KUALA LUMPUR**

2018

UNIVERSITY OF MALAYA
ORIGINAL LITERARY WORK DECLARATION

Name of Candidate: **Katrina D. Dambul**

Matric No: **KHA110053**

Name of Degree: **Doctor of Philosophy**

Title of Project Paper/Research Report/Dissertation/Thesis ("this Work"):

Charaterisation of Drawing Parameters for Fabrication of Flat Fibers

Field of Study: **Wave and Propagation**

I do solemnly and sincerely declare that:

- (1) I am the sole author/writer of this Work;
- (2) This Work is original;
- (3) Any use of any work in which copyright exists was done by way of fair dealing and for permitted purposes and any excerpt or extract from, or reference to or reproduction of any copyright work has been disclosed expressly and sufficiently and the title of the Work and its authorship have been acknowledged in this Work;
- (4) I do not have any actual knowledge nor do I ought reasonably to know that the making of this work constitutes an infringement of any copyright work;
- (5) I hereby assign all and every rights in the copyright to this Work to the University of Malaya ("UM"), who henceforth shall be owner of the copyright in this Work and that any reproduction or use in any form or by any means whatsoever is prohibited without the written consent of UM having been first had and obtained;
- (6) I am fully aware that if in the course of making this Work I have infringed any copyright whether intentionally or otherwise, I may be subject to legal action or any other action as may be determined by UM.

Candidate's Signature

Date: 8th August 2018

Subscribed and solemnly declared before,

Witness's Signature

Date:

Name:

Designation:

CHARACTERISATION OF DRAWING PARAMETERS FOR FABRICATION OF FLAT FIBERS

ABSTRACT

In this thesis, drawing parameters involved in the fabrication of flat fibers were characterized. Two fundamental aspects of flat fiber fabrication were investigated, which were the effect of drawing parameters on the dimension of the flat fibers and the control of flat fiber dimensions. In the drawing of flat fibers, five parameters were identified to affect the final flat fiber dimension which were furnace temperature, preform wall thickness, draw speed, feed speed and vacuum pressure. Experimental results showed that higher furnace temperature, higher draw speed and lower feed speed resulted in capillaries with a reduced outer diameter, which led to flat fibers with reduced thickness. Preform wall thickness also influenced the thickness of the flat fibers where thin-walled preforms were more sensitive to temperature and vacuum pressure deviations due to having higher surface tension and higher viscosity. Another important finding was the furnace temperature and vacuum pressure, related to the surface tension and viscosity of the fiber being drawn, were a function of the preform material. In order to control the final flat fiber dimension, knowledge of the preform material was also essential. In single stage drawing, by varying the drawing parameters, control of capillary dimension was achieved when drawing to a diameter of 1.25 mm compared to 125 μm . Due to this, dual stage drawing technique was proposed for flat fiber fabrication. Flat fibers doped with germanium oxide were fabricated using both single and dual stage drawing, with results confirming that dual stage drawing achieved better control of the flat fiber dimension. Optical characterization performed on the doped flat fiber showed multimode propagation, a limitation due to the core dimension and to achieve single mode propagation, suitable preform core is required. It was also difficult to achieve the required flat fiber dimension using a thin-walled preform doped with germanium oxide and boron

trioxide due to effects of dopant diffusion. Fabrication of multicapillary flat fibers with its lack of light guidance led to the development of the improved doped flat fibers with dual airholes. A novel and improved fabrication technique was successfully demonstrated in the fabrication of doped flat fiber with dual airholes. The doped flat fiber with dual airholes had a dimension of $165\text{ }\mu\text{m} \times 33\text{ }\mu\text{m}$ and the airhole diameter measured was $10.8\text{ }\mu\text{m}$. Optical characterization demonstrated that the core was able to successfully guide light and the airholes were not collapsed. This significant fabrication technique uses only a drawing tower and eliminates the need for a clean room facility. The new fabrication technique is simple, cost-effective and allows a flexible core structure arrangement using glass rods and capillaries with different refractive indices. This flexibility allows a wide range of multistructured flat fibers to be fabricated without a doped preform and the ability to fabricate core dimensions with accuracy. The multistructured flat fibers that can be fabricated using the novel fabrication technique are single core flat fiber, dual core flat fiber, multicore flat fiber, multicapillary and multicore flat fiber and multi-index flat fiber.

Keywords: Flat fibers, fabrication, drawing parameters, multistructured flat fibers and multicore flat fibers.

PENCIRIAN PARAMETER TARIKAN UNTUK FABRIKASI GENTIAN OPTIK RATA

ABSTRAK

Dalam tesis ini, parameter tarikan yang terlibat dalam fabrikasi gentian optik rata telah dicirikan. Dua aspek asas fabrikasi gentian optik rata telah diselidiki, iaitu kesan parameter tarikan pada dimensi gentian optik rata dan kawalan dimensi gentian optik rata. Dalam fabrikasi gentian optik rata, lima parameter telah dikenalpasti untuk mempengaruhi dimensi akhir gentian optik rata iaitu suhu relau, ketebalan dinding preform, kelajuan tarik, kelajuan tolak dan tekanan vakum. Keputusan eksperimen menunjukkan bahawa suhu relau dan kelajuan tarik yang lebih tinggi dan kelajuan tolak yang lebih rendah menghasilkan kapilari dengan diameter luaran yang lebih rendah dan gentian optik rata dengan ketebalan yang lebih rendah. Ketebalan dinding preform juga mempengaruhi ketebalan gentian optik rata di mana preform berdinding nipis lebih sensitif terhadap suhu dan penyimpangan tekanan vakum kerana mempunyai ketegangan permukaan dan kelikatan yang lebih tinggi. Suhu relau dan tekanan vakum, yang berkaitan dengan ketegangan permukaan dan kelikatan gentian optik rata yang difabrikasi, adalah berkait rapat dengan bahan preform. Untuk mengawal dimensi akhir gentian optik rata, pengetahuan tentang bahan preform juga penting. Dalam fabrikasi tarikan peringkat tunggal, dengan memvarikan parameter tarikan, kawalan dimensi kapilari dicapai apabila difabrikasi ke diameter 1.25 mm berbanding dengan 125 μm . Disebabkan ini, teknik fabrikasi tarikan dwi peringkat dicadangkan untuk fabrikasi gentian optik rata. Gentian optik rata yang didopkan dengan germanium oksida telah difabrikasi menggunakan teknik fabrikasi tarikan peringkat tunggal dan dwi peringkat, dengan keputusan mengesahkan bahawa fabrikasi tarikan dwi peringkat mencapai kawalan yang lebih baik untuk dimensi gentian optik rata. Pencirian optik yang dilakukan pada gentian optik rata yang telah didop menunjukkan pembimbingan cahaya pelbagai

mod yang merupakan batasan kerana dimensi teras gentian optik rata. Untuk mencapai pembimbingan mod tunggal, teras preform yang sesuai diperlukan. Ia juga sukar untuk mencapai dimensi gentian optik rata yang diperlukan menggunakan preform berdinginding nipis yang didop dengan germanium oksida dan boron trioksida kerana kesan penyebaran dopan. Fabrikasi gentian optik rata pelbagai kapilari dengan ketiadaan bimbingan cahaya membawa kepada rekabentuk yang lebih baik iaitu gentian optik rata berdop dengan dua lubang udara. Satu teknik fabrikasi novel dan ditambahbaik telah berjaya didemonstrasikan dalam fabrikasi gentian optik rata berdop dengan dua lubang udara. Gentian optik rata berdop dengan dua lubang udara ini mempunyai dimensi $165\ \mu\text{m} \times 33\ \mu\text{m}$ dan diameter lubang udara yang diukur adalah $10.8\ \mu\text{m}$. Pencirian optik menunjukkan bahawa teras gentian optik rata berdop berjaya membimbing cahaya dan lubang udara tidak tertutup. Teknik fabrikasi yang penting ini hanya menggunakan menara tarikan dan tidak perlu menggunakan kemudahan bilik bersih. Teknik fabrikasi yang novel ini adalah mudah, kos efektif dan membolehkan susunan struktur teras yang fleksibel menggunakan batang kaca dan kapilari dengan indeks bias yang berlainan. Fleksibiliti ini membolehkan fabrikasi pelbagai struktur gentian optik rata tanpa preform berdop dan keupayaan untuk memfabrikasi dimensi teras dengan tepat. Gentian optik rata pelbagai struktur yang boleh difabrikasi menggunakan teknik fabrikasi baru ini adalah gentian optik rata dengan teras yang tunggal, gentian optik rata dengan dua teras, gentian optik rata dengan pelbagai teras, gentian optik rata dengan pelbagai kapilari dan pelbagai teras dan gentian optik rata pelbagai indeks.

Keywords: Gentian optik rata, fabrikasi, parameter tarikan, gentian optik rata pelbagai struktur dan gentian optik rata pelbagai teras.

ACKNOWLEDGEMENTS

In the name of Allah, Most Gracious and Most Merciful. Alhamdulillah, all praise is to Allah, for everything that He has given me.

During my studies, I am indebted to three main mentors for their technical knowledge, unwavering support and constant encouragement. They are:

1. My main supervisor, Prof. Faisal Rafiq Mahamd Adikan, for his supervision and insights, and help in solving my research problems.
2. My co-supervisor, Dr. Nizam Tamchek, for his advice and motivation, and review of my countless drafts.
3. Dr. Ghafour Amouzad Mahdiraji, for his guidance and all his fabrication help in the drawing tower.

I would like to acknowledge all current and past members of Integrated Lightwave Research Group in Faculty of Engineering, University of Malaya, who have helped me in one way or another, directly or indirectly, and play a role in my studies. Special thanks goes to Fatemeh, Fahmi, Soo Yong, Sarahah, Reza, Yeo, Wei Ru, Din Chai, Zahra, Rosdi, Desmond and Gabriel.

Thank you to the Ministry of Higher Education Malaysia for awarding me the MyPhD scholarship, my colleagues in Faculty of Engineering, Multimedia University, Cyberjaya, my friends, my family-in-laws (*Mak*) and last but not least, my family, for their endless encouragement and support.

This thesis is dedicated to my lifelong inspirations -

My husband and my parents, for their unconditional love

My four sons, who taught me how to love unconditionally

The loving memory of *Kimmes Masut*

TABLE OF CONTENTS

Abstract	iii
Abstrak	v
Acknowledgements	vii
Table of Contents	viii
List of Figures	xii
List of Tables	xvii
List of Appendices	xxii
 CHAPTER 1: INTRODUCTION	 1
1.1 Overview	1
1.2 Motivations	4
1.3 Objectives	6
1.4 Thesis Outline	7
 CHAPTER 2: FABRICATION OF OPTICAL FIBERS	 9
2.1 Introduction	9
2.2 Fabrication of Optical Fiber	11
2.2.1 Fiber drawing tower	11
2.2.2 Fiber drawing process	15
2.2.3 Neck down region	17
2.2.3.1 Heating zone length	18
2.2.3.2 Drawing process parameters	20
2.2.3.3 Physical and material properties of glass	21
2.3 Fabrication of Capillary	26
2.4 Fabrication of Flat Fiber	29

2.5	Practical Limitations in Flat Fiber Drawing	32
2.6	Summary	34

CHAPTER 3: EFFECT OF DRAWING PARAMETERS ON THE FABRICATION OF FLAT FIBERS 35

3.1	Introduction.....	35
3.2	Literature Review	37
3.2.1	Fused silica	37
3.2.2	Drawing parameters.....	38
3.3	Methodology.....	44
3.4	Results and Discussion	48
3.4.1	Furnace temperature	48
3.4.2	Preform wall thickness	50
3.4.3	Draw speed and feed speed	56
3.4.4	Vacuum pressure	60
3.5	Fabrication Repeatability.....	67
3.6	Summary.....	68

CHAPTER 4: CONTROL OF FLAT FIBER DIMENSIONS 71

4.1	Introduction.....	71
4.2	Literature Review	73
4.3	Fabrication of Doped Flat Fiber.....	76
4.3.1	GeO ₂ doped flat fibers using single stage drawing method.....	77
4.3.2	Single stage drawing method for specific diameter.....	85
4.3.2.1	Fabrication of 125 μ m capillary from 25 mm preform	86
4.3.2.2	Fabrication of 1.25 mm capillary from 25 mm preform	90

4.4	Dual Stage Drawing Method	93
4.5	Characterization of Doped Flat Fiber	97
4.5.1	Attenuation loss	99
4.5.2	Near field intensity distribution patterns	100
4.5.3	Theoretical framework	102
4.5.4	Discussion on characterization results	104
4.6	Fabrication of Multidopant Flat Fiber	106
4.7	Summary	109
 CHAPTER 5: NOVEL MULTISTRUCTURED FLAT FIBERS		111
5.1	Introduction	111
5.2	Fabrication of Multicapillary Flat Fiber	111
5.3	Fabrication of Multicore Flat Fiber	116
5.4	Fabrication of Doped Flat Fiber with Airholes	119
5.4.1	Simulation results	120
5.4.2	Fabrication framework	128
5.4.3	Experimental results	130
5.4.3.1	Proposed design	130
5.4.3.2	Fabrication results	133
5.4.3.3	Characterization results	140
5.4.3.4	Discussion on fabrication and characterization results	142
5.5	Potential Multistructured Flat Fibers	144
5.6	Potential Applications	147
5.7	Summary	149

CHAPTER 6: CONCLUSION AND FUTURE WORKS	150
6.1 Conclusions.....	150
6.2 Future Work.....	155
6.3 Outcome and Author's Achievements.....	157
References	159
List of Patents, Awards, Publications and Papers Presented.....	170
Appendix	172

LIST OF FIGURES

Figure 1.1: (a) Photonic crystal fiber (b) Elliptical core fiber (c) D-shaped fiber (d) Flat optical fiber.	1
Figure 1.2: (a) Flat fiber (b) Planar waveguide.	2
Figure 1.3: Flowchart of thesis outline.	8
Figure 2.1: Schematic diagram of drawing tower in Flat Fiber Laboratory, University of Malaya.	12
Figure 2.2: Actual photo of fiber drawing tower in Flat Fiber Laboratory, University of Malaya, Kuala Lumpur, Malaysia (a) Top floor (b) Lower floor (c) Furnace (d) Iris (e) Diameter gauge.	13
Figure 2.3: Three major zones during fiber drawing process.	16
Figure 2.4: The viscosity versus reciprocal of absolute temperature for pure silica and various doped silica fibers (Reproduced from Chen & Jaluria, 2009 with permission).	23
Figure 2.5: Viscosity (log) versus temperature (where A is the temperature range of 1900 °C to 2200 °C).	24
Figure 2.6: Physical model of the neck down profile for optical fiber drawing.	25
Figure 2.7: Physical model of the neck down profile for capillary drawing (Fitt <i>et al.</i> , 2001).	28
Figure 2.8: Preform tube dimensions and flat fiber dimensions (Webb, 2012).	31
Figure 3.1: General flowchart for the fabrication of pure silica capillary.	45
Figure 3.2: General flowchart for the fabrication of pure silica flat fiber.	46
Figure 3.3: Effect of furnace temperature on capillary outer diameter.	49
Figure 3.4: SEM image of the fabricated capillary cross section for (a) thick preform and (b) thin preform.	51
Figure 3.5: Effect of temperature on preform with different wall thickness.	52
Figure 3.6: Effect of temperature on the inner diameter of a capillary (thin preform). ..	54
Figure 3.7: Effect of temperature on the capillary thickness (thin preform).	54

Figure 3.8: Ratio OD/ID for thin capillary. The preform OD/ID was represented by the straight line.	56
Figure 3.9: Empirical constant, k	56
Figure 3.10: Effect of draw speed on the outer diameter of a capillary (thin and thick preform) at a feed rate of 2 mm/min.	59
Figure 3.11: Outer diameter (mm) versus draw speed (m/min) at a feed rate of 6.48 (mm/min).....	59
Figure 3.12: Effect of vacuum pressure on a thin preform at (a) 0.0 kPa, (b) 0.5 kPa, (c) 1.0 kPa, (d) 1.5 kPa, (e) 2.0 kPa, (f) 2.5, 5.0 and 10.0 kPa, (g) 20.0 kPa and (h) 40.0 kPa.	63
Figure 3.13: Effect of vacuum pressure on a thick preform at (a) 1.0 kPa, (b) 2.0 kPa, (c) 4.0 kPa, (d) 6.0 kPa, (e) 10.0 kPa, (f) 20.0 kPa, (g) 40.0 kPa and (h) 59.0 kPa.....	64
Figure 3.14: Eccentricity versus vacuum (kPa) for thick preform.	66
Figure 4.1: Flowchart for the fabrication of GeO ₂ doped flat fibers using single stage drawing method.....	78
Figure 4.2: Diameter x and y (in mm) during the drawing process (the x - axis represents the drawing time). Regions A-D show the changes in drawing conditions.	80
Figure 4.3: Microscope image of the cross section of fabricated flat fiber for vacuum settings of 0, 1.0, 1.5 and 2.0 shown in Figures 4.3 (a), (b), (c) and (d) respectively (Reproduced from Dambul <i>et al.</i> , 2011 with permission).....	81
Figure 4.4: Average eccentricity versus vacuum pressure (kPa) at 2100 °C.	82
Figure 4.5: Diameter x and y (in mm) versus drawing time with two regions of drawing conditions. Desired diameter was 125 μ m as shown in the straight line.	88
Figure 4.6: Diameter x and y (in mm) versus drawing time at a constant feed speed and draw speed.....	88
Figure 4.7: Diameter x and y (in mm) versus drawing time at a constant feed speed.....	89
Figure 4.8: Draw speed (m/min) versus drawing time at a constant feed speed of 6.5 mm/min.	90
Figure 4.9: Diameter x and y (in mm) versus drawing time at a constant feed speed of 6.5 mm/min.	92

Figure 4.10: Diameter x and y (in mm) versus drawing time (minutes) with feed speed of 2.6 mm/min and draw speed of 1 m/min.....	92
Figure 4.11: Diameter x and y (in mm) versus drawing time (minutes) with feed speed of approximately 5 mm/min and draw speed of 2 m/min.	93
Figure 4.12: Flowchart for the fabrication of flat fibers using two stage drawing method.	94
Figure 4.13: Cross section image of undoped flat fiber rod.....	95
Figure 4.14: Dimension x and y (in mm) versus drawing time (minutes) with feed speed of approximately 6 mm/min and draw speed of 2 m/min.	95
Figure 4.15: Dimension x and y (in mm) versus drawing time (minutes) with feed speed of approximately 8.5 mm/min and draw speed of 2.5 m/min.	96
Figure 4.16: Cross section of the flat fiber sample with 6 mol% of GeO ₂	97
Figure 4.17: Experimental setups for (a) insertion loss measurements and (b) near field measurement.....	98
Figure 4.18: Insertion loss measurements at 1550 nm.	100
Figure 4.19: 60 cm flat fiber at 635 nm under 2 launching conditions (left (a) and middle (b)).	101
Figure 4.20: 60 cm flat fiber at 1310 nm under 3 launching conditions (left (a), middle (b) and right (c)).	101
Figure 4.21: 60 cm flat fiber at 1550 nm under 3 launching condition (right (a), middle (b) and left (c)).	102
Figure 4.22: (a) Modal profile for 1 st order mode at (i) 635 nm, (ii) 1310 nm (iii) 1550 nm. (b) Modal profile for 5 th order mode at (i) 635 nm, (ii) 1310 nm (iii) 1550 nm. (c) Modal profile for higher order modes at (i) 635 nm, (ii) 1310 nm and (iii) 1550 nm.	105
Figure 4.23: (a) Deformed flat fiber rod obtained at a furnace temperature of 2100 °C and 2 kPa vacuum pressure (b) Large airholes at the sides of the flat fiber rod.	107
Figure 4.24: Flat fiber sample.	108
Figure 5.1: Microscope images of the capillary fabricated.....	113
Figure 5.2: Microscope images of the capillary fabricated.....	113

Figure 5.3: Microscope images of the capillary fabricated at vacuum of 25 kPa at various feed rate and draw speed setting.	113
Figure 5.4: Cross section of multicapillary fiber with (a) multiple rows of holes (b) one row of holes.	116
Figure 5.5: (a) Preparation of step index rods with hooks (b) Fusing of glass rods using silica bridges (c) Preform arrangement inside the mount (Reproduced from Mahdiraji <i>et al.</i> , 2014 with permission).	118
Figure 5.6: Cross section of the 6 core multicore flat fiber (Reproduced from Mahdiraji <i>et al.</i> , 2014 with permission).	118
Figure 5.7: Single airhole and doped core.	119
Figure 5.8: Two airholes in the core.	126
Figure 5.9: Single mode propagation in doped flat fiber with 2 airholes at wavelength of (a) 1310 nm and (b) 1700 nm.	126
Figure 5.10: Effective refractive index versus wavelength for single mode modal profile observed.	126
Figure 5.11: Three airholes in doped flat fiber.	127
Figure 5.12: Proposed design for fabrication.	131
Figure 5.13: Proposed preform structure. The black circle (including the capillary) represents aluminosilicate material which has a higher refractive index of 1.538 and the blue circle (including the 30 mm preform tube) represents borosilicate material which has a lower refractive index of 1.473.	131
Figure 5.14: Flowchart of fabrication of doped flat fibers with dual airholes.	133
Figure 5.15: Arrangement of the rod and capillaries linear array.	135
Figure 5.16: Applying bridges on linear array using hand torch.	135
Figure 5.17: Preform drawing for first stage drawing.	135
Figure 5.18: (a) Capillary with a dimension of 1.539 mm x 1.348 mm and airhole with a diameter of 0.117 mm. The two airholes were not closed. (b) Epoxy glue applied on top of the capillary.	136
Figure 5.19: Drawing of the fiber capillary for second stage drawing.	137

Figure 5.20: SEM image of flat fiber with dual airholes before vacuum pressure was applied. Airhole diameter was 12.1 μm and outer diameter was 163 μm	138
Figure 5.21: SEM image of flat fiber with dual airholes after vacuum pressure applied at 3 kPa. Airhole diameter was 11.2 μm and flat fiber was 237 μm x 51.8 μm . The width of the core was 109 μm . There were some holes at the sides of the flat fiber and interstitial holes between the cores. This image was taken before coating was applied.	138
Figure 5.22: SEM image of flat fiber with dual airholes after vacuum pressure applied at 6 kPa. Airhole diameter measured was 10.8 μm and flat fiber 165 μm x 33 μm . No more holes observed at the sides and smaller interstitial holes. This image was taken after coating was applied.	139
Figure 5.23: Flat fiber with dual airholes seen using microscope with applied light. Airholes remain as light does not pass the airholes.	139
Figure 5.24: Expected results from characterization.....	140
Figure 5.25: Actual experiment setup for near field characterization.....	141
Figure 5.26: Determination of optimized distance for coupling.	141
Figure 5.27: Optimized distance at 9 μm	141
Figure 5.28: CCD images at different launching conditions (a) left (b) middle and (c) right	142
Figure 5.29: Different flat fiber structure. (a) Single core flat fiber (b) Dual core flat fiber (c) Multicore flat fiber (d) Multicore and multicapillary flat fiber (e) Multi-index flat fiber	146

LIST OF TABLES

Table 3.1: Drawing process comparison.	36
Table 3.2: Softening temperature for pure silica with different water content.	37
Table 3.3: Summary of literature review for various drawing parameters.	41
Table 3.4: Summary of experimental work done in Chapter 3.	47
Table 3.6: Flat fiber width measurements.	68
Table 3.7: Flat fiber thickness measurements.	68
Table 3.8: General trend of drawing parameter studied in Chapter 3.	69
Table 3.9: Summary from effect of drawing parameters.	70
Table 4.1: Effect of drawing conditions on dopant diffusion.	74
Table 4.2: Changes in drawing conditions during the fabrication process. Regions A-D indicate the region where drawing conditions were changed.	80
Table 4.3: Flat fiber and its core dimensions.	83
Table 4.4: Summary of experimental work done in Section 4.3.2.	86
Table 4.5: Summary of experimental results.	91
Table 4.6: Flat fibers obtained using dual stage drawing.	96
Table 4.7: Core and cladding refractive index of the flat fiber.	103
Table 4.8: Initial drawing conditions.	106
Table 5.1: Effect of drawing conditions on the multicapillary flat fiber.	114
Table 5.2: Different core thickness at 1550 nm.	123
Table 5.3: Modal profile obtained at 1 mol% of GeO ₂ doped core at a core of 13.6 μm	124
Table 5.4: Modal profiles for 3 airholes at dopant concentration of 5 mol% of GeO ₂ for varying effective refractive index, n_{eff}	127
Table 5.5: Preform structure design.	132

LIST OF SYMBOLS AND ABBREVIATIONS

Symbols

$^{\circ}$:	Degree symbol
μ	:	Viscosity
μ_{Ge}	:	Viscosity of germanium oxide doped glass
μ_{Si}	:	Viscosity of pure silica glass
μ_o	:	Viscosity related constant
γ	:	Drawing tension
λ_0	:	Free space wavelength
λ	:	Wavelength
T	:	Temperature
w	:	Width
w_c	:	Width of the core
t	:	Thickness
t_c	:	Core thickness
L	:	Heating zone length
L_f	:	Length of fiber sample
A	:	Preform area
D_x	:	Diameter of axis X
D_y	:	Diameter of axis Y
F_t	:	Tangential force applied to two parallel planes
d	:	Distance
v	:	Relative velocity of the two planes
U_d	:	Draw speed
U_f	:	Feed speed

k	:	Constant derived from experiment
ΔH_{μ}	:	Activation energy for viscous flow
R	:	Gas constant
R_1	:	Preform outer radius
R_2	:	Fiber radius
F_{γ}	:	Force due to draw tension
F_g	:	Force due to gravity
F_u	:	Force due to viscous stress
F_{ζ}	:	Force due to surface tension
F_I	:	Force due to inertia
F_e	:	Force due to the shear force exerted by the external gas velocity
F_v	:	Force due to the vacuum pressure
C_r	:	Collapse ratio
$R_1(z)$:	Inner diameter neck down profile
$R_2(z)$:	Outer diameter neck down profile
R_{10}	:	Inner radius for the capillary
R_{20}	:	Outer radius for the capillary
h_1	:	Inner diameter of the capillary
h_2	:	Outer diameter of the capillary
h_{10}	:	Preform inner diameter
h_{20}	:	Preform outer diameter
B	:	$\log(U_d/U_f)$
β	:	$\ln(U_d/U_f)$
x	:	Distance along the axis of the capillary
N_c	:	Capillary number

D_r	:	Draw ratio
ε	:	Aspect ratio
OD	:	Outer diameter
ID	:	Inner diameter
OD_{fiber}	:	Outer diameter of the drawn fiber
$OD_{preform}$:	Outer diameter of the preform
S	:	Key parameter
D_0	:	Inert diffusion constant
E	:	Activation energy
k_B	:	Boltzmann constant
n_i	:	Refractive index of component i
c_i	:	Mass fraction of component i
ρ_i	:	Density of component i
c	:	Constant
χ	:	Mole fraction
Δ	:	Refractive index difference
A	:	Positive constant
d	:	Dopant concentration
n_1	:	Core refractive index
n_2	:	Cladding refractive index
P_0	:	Received power at the initial length
P_1	:	Received power at the final length

Abbreviations

Al ₂ O ₃	:	Aluminium oxide
B ₂ O ₃	:	Boron trioxide
CCD	:	Charge-coupled device
EDX	:	Energy dispersive X-ray Spectroscopy
FESEM	:	Field emission scanning electron microscope
GeCl ₄	:	Germanium tetrachloride
GeO ₂	:	Germanium dioxide
IL	:	Insertion loss
MCVD	:	Modified chemical vapour deposition
MMI	:	Multimode interference
NA	:	Numerical aperture
OVD	:	Outer vapour deposition
P ₂ O ₅	:	Phosphorus pentoxide
PCVD	:	Plasma-activated vapour deposition
pH	:	Potential of hydrogen
PMMA	:	Polymethylmethacrylate
RF	:	Radio frequency
SEM	:	Scanning electron microscope
SiCl ₄	:	Silicon tetrachloride
SiO ₂	:	Silicon dioxide
SMF	:	Single mode fiber
TiO ₂	:	Titanium dioxide
UV	:	Ultraviolet
VAD	:	Vapour axial deposition

LIST OF APPENDICES

Appendix A: Copyright and Permission from Journals

Appendix B: Modal analysis of flat fibers

University of Malaya

CHAPTER 1: INTRODUCTION

1.1 Overview

In 2000, the global specialty optical fiber market is at USD \$ 239 million (Méndez & Morse, 2011) and increased nearly threefold to USD \$ 639 million in 2010 (2015 Specialty Optical Fiber Industrial Report). A conservative estimate predicts the global market revenue for specialty optical fiber to be USD \$ 1763 million in 2020 (The World Market for Specialty Optical Fibers and Fiber Lasers). Specialty optical fibers are used to enable modern technologies such as applications in telecommunication, medical, industrial, military, security, sensing and automotive. Specialized optical fibers can be classified in terms of their material composition, waveguide design and coatings (Méndez & Morse, 2011). A few examples of specialty optical fiber that has unique waveguide design include photonic crystal fibers (Russell, 2003), elliptical core fibers (Dyott, 1995), D-shaped fibers (Cordaro *et al.*, 1994) and flat optical fibers (Webb *et al.*, 2007 and Adikan *et al.*, 2012). The schematic of the cross section view of these fibers is shown in Figure 1.1 (a) – (d). The fabrication of specialty optical fibers is an area of great research interest, as the technology is not as mature as the fabrication of optical fibers used for communication purposes such as single mode fibers.

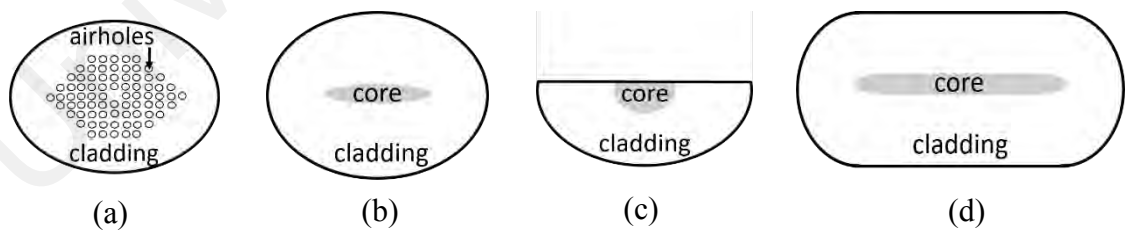


Figure 1.1: (a) Photonic crystal fiber (b) Elliptical core fiber (c) D-shaped fiber (d) Flat optical fiber.

Flat optical fibers, which will be termed as flat fibers throughout this thesis, are an area of significant research interest, due to the fact that it combines the functional advantages of a planar waveguide and the mechanical advantages of an optical fiber (Gawith *et al.*, 2007 & Materials World, 2007). At present, optical fibers widely used in the market have

a circular core and cladding but flat fibers have a planar core and cladding dimensions. The geometry of a flat fiber is almost similar to a planar waveguide, in particular buried channel waveguide, with a higher refractive index core layer at the inner/center section and a cladding surrounding layer. The refractive index in the core is always higher than the cladding layer to allow light to continuously propagate inside the flat fiber via total internal reflection phenomena (Buck, 1995 and Kasap, 2001). By utilizing this concept, theoretically the light always propagates in the core of the fiber so much that the length of the flat fiber can be endless, behaving like a conventional optical fiber (Kalli *et al.*, 2015). Figure 1.2 shows the difference in the geometry of a flat fiber (a) and planar waveguide (b).

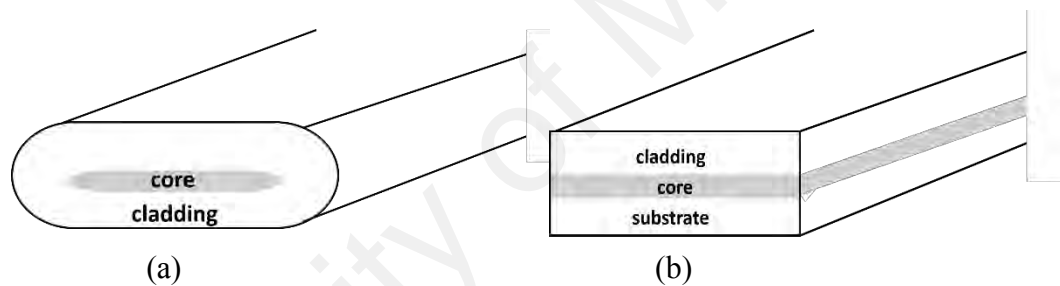


Figure 1.2: (a) Flat fiber (b) Planar waveguide.

Planar waveguides, which allows for light to be guided on defined paths on a planar substrate, are the basic component in the construction of many integrated optics devices including splitters, couplers, interferometers and gratings (Buck, 1995, Okamoto, 2006 & Saleh & Teich, 2007). Planar waveguide devices can be fabricated on the surface of a flat piece of material such as silica (Li & Henry, 1996), a wafer of silicon, semiconductor crystal or even a block of plastic (Dutton, 1998). Different fabrication methods that can be used to fabricate specific planar waveguide devices include lithography, etching and epitaxial growth (Singh, 1996 & Hunsperger, 2009). But these fabrication methods are expensive and often require a high degree of precision (Dutton, 1998). Planar waveguides are also mechanically rigid as it is commonly built on rigid planar substrates such as

silicon wafers and incur unwanted coupling loss when being pigtailed to optical fibers (Adikan, 2007).

Since the introduction of flat fibers in 2007, significant attention has been made to the development of integrated optics devices on flat fibers using fabrication methods commonly used on planar waveguides. Flat fibers were initially developed as alternatives to planar waveguides due to its low-cost fabrication technique (Webb *et al.*, 2007). In addition, the ribbon-like flat fiber can have extended length and are mechanically flexible when compared to planar waveguides (Adikan *et al.*, 2012).

Integrated optics devices can be fabricated directly on the flat fiber using methods such as micromachining (Ambran *et al.*, 2012) and femtosecond laser inscription (Kalli *et al.*, 2015). A precision micromachining method can be done on a flat fiber substrate by micromachining two air trenches on the flat fibers (Ambran *et al.*, 2012). Using low index contrast materials, the micromachining method can be used to fabricate multimode interference (MMI) devices such as a 1 x 3 splitter device (Ambran *et al.*, 2012). In femtosecond laser inscription method, a tightly focused beam from a femtosecond laser is translated into a bulk transparent material which caused the refractive index of the core material to increase due to the non-linear absorption process (Kalli *et al.*, 2015). This technique can be used to produce channel waveguides with a high refractive index contrast (Davis *et al.*, 1996) and has also been demonstrated in active media (Thomson *et al.*, 2006). Using femtosecond laser inscription, inscription of Bragg gratings, ring resonator, disc resonator, Mach-Zehnder interferometer and microfluidic channel has been demonstrated on a flat fiber (Kalli *et al.*, 2015).

Addition of a photosensitive core to the flat fiber, by doping the core with Germanium and/or Boron, allows fabrication of UV-written devices using methods such as direct UV writing (Adikan, 2007) and direct grating writing (Webb *et al.*, 2007). Direct UV writing

method is used to define waveguide structures in the photosensitive core of the flat fibers (Holmes *et al.*, 2008 and Adikan, 2007). The direct UV writing process inscribes a pre-designed waveguide structure by translating the photosensitive sample beneath a focused laser beam (Webb *et al.*, 2007). Straight channels and y-splitters (Ambran *et al.*, 2011) have been defined on the flat fiber core layer via single beam direct UV writing (Adikan, 2007). Evanescent field sensors have also been demonstrated on flat fibers by writing Bragg gratings on the core of the fiber and using the principle of shifting the Bragg wavelength (Holmes *et al.*, 2008).

1.2 Motivations

Flat fibers are fabricated using a conventional fiber drawing tower. Currently, optical devices fabricated on flat fibers require additional technology such as micromachining to fabricate trenches on the flat fiber (Ambran *et al.*, 2012), direct UV writing and femtosecond laser inscription to perform direct inscription on the flat fibers by inducing a change in the refractive index of the sample (Webb *et al.*, 2007 and Kalli *et al.*, 2015). Micromachining technique, a type of microfabrication method, require clean room facilities and has multiple fabrication processing steps (Davim *et al.*, 2017). Direct UV writing method, which produces UV induced refractive index changes on the sample, requires the samples to be photosensitive and the magnitude of refractive index change is small (Watts, 2002). Femtosecond laser inscription does not require the samples to be photosensitive and thus can produce waveguides in three dimensions, but also require a high precision process (Sugioka & Cheng, 2014).

In addition to directly modifying the core refractive index of the flat fiber through microfabrication techniques, modification of the flat fiber design and structure itself (for example in Poh *et al.*, 2017) may result in changes during the detection and measurement

of its absorption, fluorescence, light evanescent field and material refractive index properties.

There is a research gap here and this is an area to be explored, as each of these changes allow for specific application for the flat fiber. The potential application to society is vast, as each specialized fiber can have different applications that can be used in sensing, medical, industrial, communications and so on. There is also a potential for multiple functionality in a single flat fiber, as flat fibers have a wide, planar surface area which can be exploited. For example, multiple cores can be fabricated on the flat fiber core (Mahdiraji *et al.*, 2014), allowing for multiple channels transmission, which may increase the bandwidth demand for communication purposes. At present, innovative flat fiber technology is needed to cope with the exponential increase of internet traffic growth due to the digital age of mobile users and a lifestyle that is increasingly dependent on the internet (Gubbi *et al.*, 2013). In order to achieve this, it is clear that fundamental research on flat fiber fabrication is required.

This thesis focuses on the characterization of drawing parameters for the fabrication of flat fibers. By characterizing the drawing parameters during the fabrication of a flat fiber, a general fabrication mechanism that can be applied to any type of fiber fabrication design can be formulated. This knowledge can be used to gain an understanding on how to proceed with the design and fabrication of different types of flat fiber applications and different types of specialty optical fiber fabricated using a fiber drawing tower, with no additional technology required. This method will be simple and cost effective, results in faster production and do not require a clean room environment. Moreover, characterization of the fiber drawing parameters can potentially result in improved flat fiber properties, and improved fabrication process, in particular for the fabrication of specialty optical fibers. By understanding the fabrication process for a conventional flat

fiber, the knowledge can be extended to fabricate other types of specialty optical fiber with specific application, including micro capillary, photonic crystal fiber, multicore flat fiber, multicapillary flat fiber, tapered flat fiber and other waveguide designs.

This thesis provides the fabrication methodologies, experimental process and characterization results for flat fibers and multistructured flat fibers. Contributions from this thesis to the current body of knowledge are analysis of effect of drawing parameters on the fabrication of flat fibers and control of flat fiber dimensions, an improved flat fiber fabrication methodology, a new type of multistructured flat fiber and a new and improved fabrication technique to fabricate multistructured flat fibers with better control.

1.3 Objectives

This thesis focuses on the characterization of drawing parameters for the fabrication of flat fibers, which subsequently lay the foundation for the design and fabrication of a new design of multistructured flat fiber. The objectives of this thesis are as follows:

1. To propose and fabricate flat fibers (with no core) with different thickness in order to investigate and characterize related drawing parameters (furnace temperature, draw speed, feed speed and vacuum pressure);
2. To propose and fabricate doped flat fibers in order to investigate and characterize related drawing parameters (furnace temperature, draw speed, feed speed and vacuum pressure);
3. To propose and fabricate a new type of multistructured flat fiber including multicore flat fiber;
4. To propose and demonstrate improved fabrication technique for fabrication of multistructured flat fibers including multicore flat fibers.

1.4 Thesis Outline

This thesis consists of six chapters including this introductory chapter. The main content of each chapter is briefly described as below:

Chapter 1 provides an overview of the research work done in this thesis, including the research objectives, motivation and thesis outline.

Chapter 2 introduces optical fiber drawing and gives an overview of the fiber drawing tower, the fiber drawing process and the neck down region. The factors affecting neck down region such as heating zone length, drawing process parameters and physical and material properties of glass are discussed. The fabrication of capillary and flat fibers is described. Practical limitations during fiber drawing process are also presented.

The drawing parameters for the fabrication of capillary and flat fiber using a pure silica preform tube (F300 Suprasil glass tubes) were studied and investigated in **Chapter 3**. The fabrication parameters studied were preform wall thickness, furnace temperature, draw speed, feed speed, and vacuum pressure. Two types of preform were used (thin and thick) and their fabrication results were characterized in terms of its dimension.

In **Chapter 4**, the fabrication of doped flat fibers were studied and investigated. The effect of the drawing parameters on the fabricated flat fibers were discussed. The investigation on control of flat fiber dimension were done by performing single stage drawing for two specific diameters. Dual stage drawing was also discussed in this chapter. The near field characteristics of flat fibers for varying wavelengths were investigated.

Chapter 5 presents the fabrication of multistructured flat fibers including multicapillary flat fiber and multicore flat fiber. A new multistructured flat fiber design (doped flat fiber with airholes) is proposed. Simulation was done to optimize the design of the new multistructured flat fiber and fabrication was performed as a proof-of-concept.

A new and improved fabrication technique was proposed and demonstrated in this chapter. Potential multistructured flat fibers that can be fabricated using the new fabrication technique are also proposed. Finally, **Chapter 6** concludes all the important findings in this thesis and discusses possible future work that can be done.

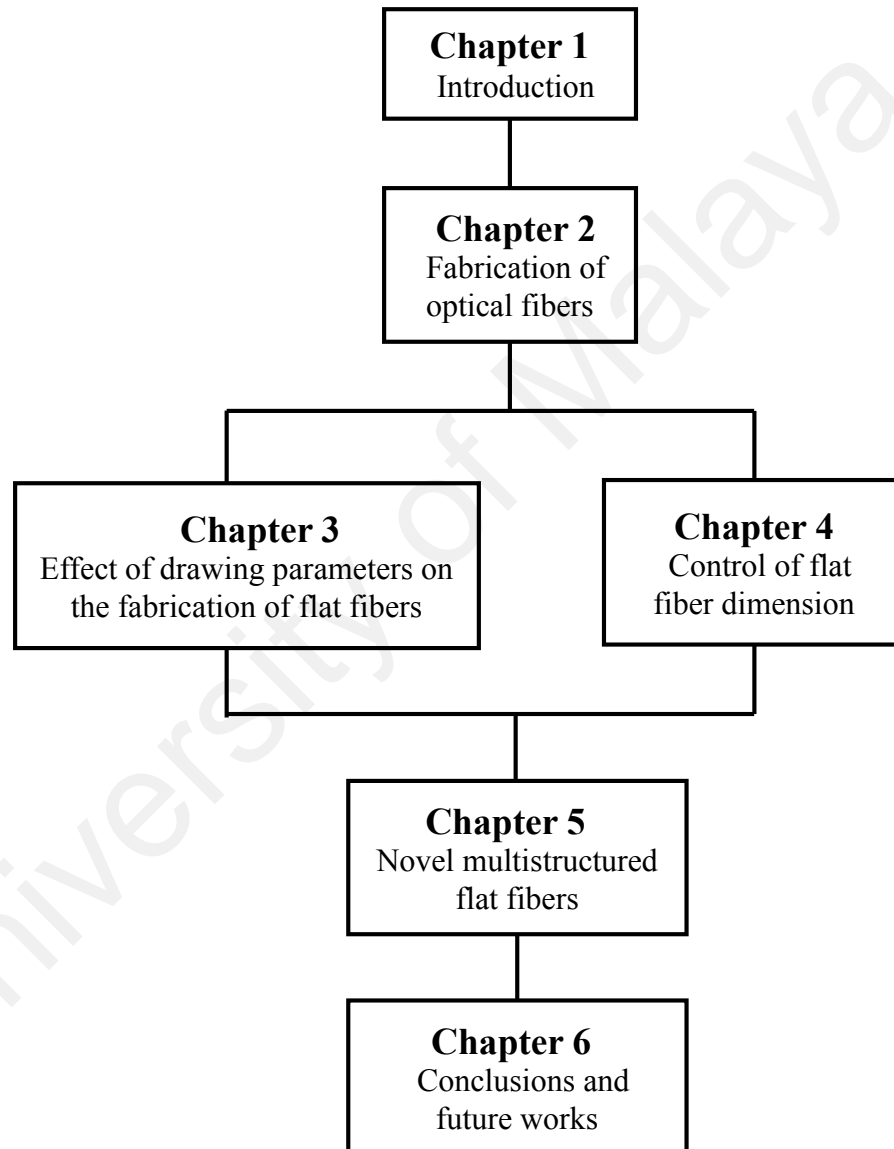


Figure 1.3: Flowchart of thesis outline.

CHAPTER 2: FABRICATION OF OPTICAL FIBERS

2.1 Introduction

In 1970, researchers from Corning Glass Works (now known as Corning Incorporated) demonstrated the first low loss optical fiber with a loss of 17 dB/km (Keck, 2000). With this breakthrough, the fabrication of optical fibers has been extensively studied, where the initial motivation was to reduce the attenuation loss for communication purposes, to improve fabrication methods for mass production of optical fibers and to reduce fiber manufacturing costs. Nowadays, single mode fibers such as Corning's SMF-28 fiber can achieve a loss of ≤ 0.18 dB/km at a wavelength of 1550 nm (Corning SMF-28 data sheet). The interest is now focused on fabrication of specialty optical fibers for a wide range of optical devices and applications.

Historically, early optical silica fibers are fabricated using the double-crucible method, where fibers are formed by directly dipping a glass rod into a melt and quickly pulling it out (Shelby, 2005). In this method, the main source of contamination comes from the furnace environment and the crucible used (Keiser, 2000). Most optical fibers are now fabricated using the preform method. A direct method to fabricate a preform is by placing a rod of the core glass into the tube of the fiber cladding and heating this configuration to fuse the two glasses together (Shelby, 2005). But this method does not guarantee the quality and pureness of the optical fiber.

Thus, most preforms are formed using vapour phase manufacturing techniques. In vapour phase manufacturing, oxidation of precursor gas mixtures forms the material layer for the preform (Buck, 1995) before it is being pulled into a fiber during the drawing process. For example, in liquid vapour phase oxidation process, vapours of metal halides (e.g. SiCl_4 and GeCl_4) react with oxygen to form a white powder of SiO_2 particles (soot) (Keiser, 2010). Vapour deposition methods to produce preforms are outer vapour

deposition (OVD), modified chemical vapour deposition (MCVD) (Nagel, 1982), plasma-activated chemical vapour deposition (PCVD) and vapour axial deposition (VAD) (Izawa & Sudo, 1986). Currently, the most effective technique to fabricate optical fiber preform is using vapour from liquid sources where dopant impurity can be found to be less than 1 ppm (Hoskova & Vydra, 1999). In addition, preforms fabricated using MCVD have lower OH impurity contamination and the deposition occurs in a very clean environment (in an enclosed reactor) (Senior & Jamro, 2009). The fabrication of preforms is beyond the scope of this thesis.

Once the preform is fabricated, the next stage is the drawing of the optical fiber from the preform. The parameters involved in the preform fabrication and fiber drawing are strictly controlled to achieve specific core and cladding refractive indices and fiber dimensions. In order to achieve the required refractive index profile, the dopant materials introduced into the silica preform (during preform fabrication process) are carefully chosen and their concentration is precisely controlled (Buck, 1995). The dopant materials can be used to increase or decrease the refractive index of the core material. For light transmission in optical communication systems, the core and cladding materials should be able to guide light within the major operating wavelengths (800 nm to 1700 nm) and must have low optical attenuation (i.e. low intrinsic absorption and scattering losses) (Senior & Jamro, 2009). As the attenuation is due to the material's absorption and scattering coefficient, maintaining the purity of the preform during the deposition of the core materials is important.

Specific fiber dimensions can be obtained during the fiber drawing process, where the dimensions are controlled by the drawing conditions and material properties (Xue *et al.*, 2005). The drawing conditions can be controlled by the drawing tower's furnace temperature, feed speed and draw speed. The physical and material properties of the

preform such as preform dimension, surface tension and viscosity also affect the final fiber dimension. The preform deformation to fiber mainly occurs at the neck down region, which is the heating region inside the drawing tower furnace.

This chapter reviews the process of optical fiber fabrication, specifically on fiber drawing fabrication. For fiber drawing, a more detailed discussion is given on the drawing tower and parameters affecting the neck down region of the preform. Next, the fiber drawing process for capillaries and flat fibers are also discussed. Finally, the conclusion is presented.

2.2 Fabrication of Optical Fiber

2.2.1 Fiber drawing tower

After preform fabrication, the next stage of the optical fiber fabrication is the drawing of the fiber preform. In this work, all the fiber drawing fabrication experiments were performed using an optical fiber drawing tower at Flat Fiber Laboratory, Department of Electrical Engineering, University of Malaya, Kuala Lumpur, Malaysia. The tower has a height of 5 meters and encompass two floors in the laboratory. The height 5 meters for the drawing tower is deemed sufficient for drawing optical fibers used for research purposes, as productivity and high-speed fabrication is not a main concern. High speed fabrication of commercial optical fibers can have drawing towers of up to 38 meters (OFC 20, Nextrom Drawing Tower).

The schematic diagram of the drawing tower is shown in Figure 2.1 and the actual drawing tower in the Flat Fiber Laboratory is shown in Figure 2.2. Figure 2.1 shows that the fiber drawing tower consists of a motorized preform chuck (feed unit), furnace, diameter gauge, tractor, UV curing lamp, capstan and drum winder. As shown in Figure 2.2 (a), the preform chuck and the furnace are located at the top floor of the Flat Fiber Laboratory. The tractor, UV lamp and the capstan are located at the lower floor of the

Flat Fiber Laboratory as seen in Figure 2.2 (b). Figure 2.2 (c) shows the furnace of the drawing tower, Figure 2.2 (d) shows the iris on the furnace and Figure 2.2 (e) shows the diameter gauge of the drawing tower.

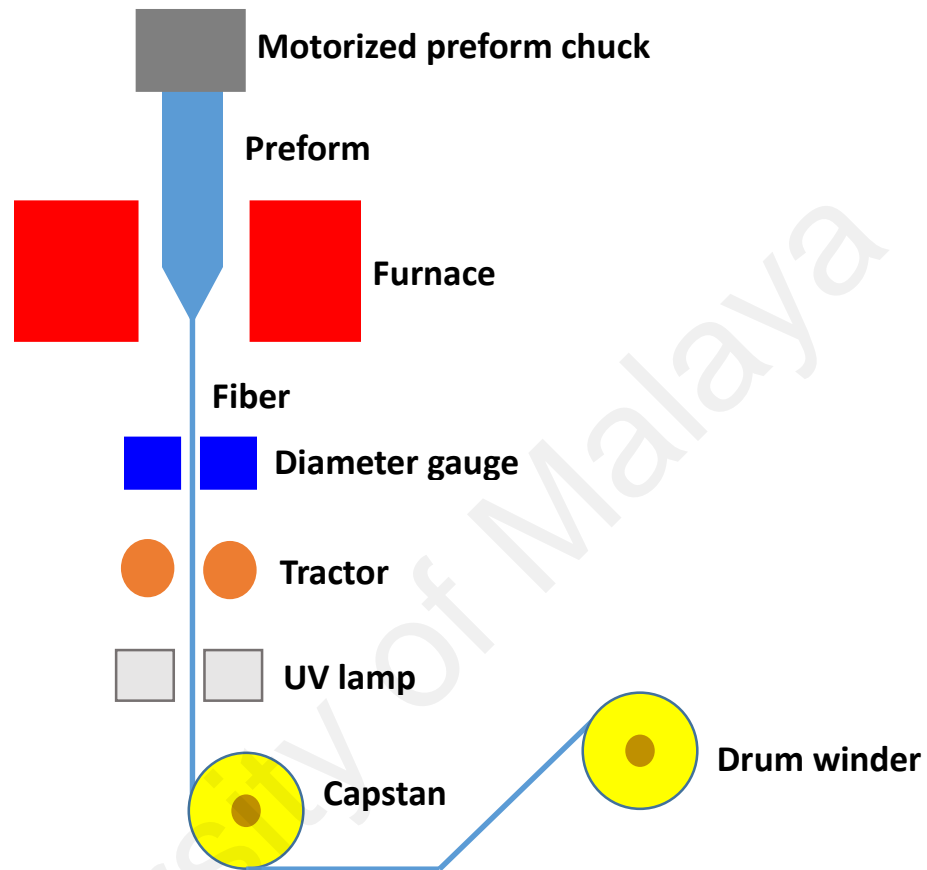


Figure 2.1: Schematic diagram of drawing tower in Flat Fiber Laboratory, University of Malaya.

The feed unit is located at the top of the drawing tower and include a motorized preform chuck. The preform chuck is used to hold the preform as it is fed into the furnace at the required feed speed. There is a high precision motorized stage to control the feed speed and preform position. The feed speed can be varied from 0.01 mm/min to 20.00 mm/min with a resolution of 0.01 mm/min. The position (transverse x and y) and load distance of the preform into the furnace can be adjusted manually using the motorized feed unit.

The cylindrical furnace is used to heat up the preform until it reaches a temperature that allows it to be drawn. The furnace uses graphite heating element that is capable of heating the preform up to 2500 °C. Graphite is used due to its thermal and mechanical properties, high thermal shock resistance, good strength at high temperatures and high emissivity (Payne & Gambling, 1976).

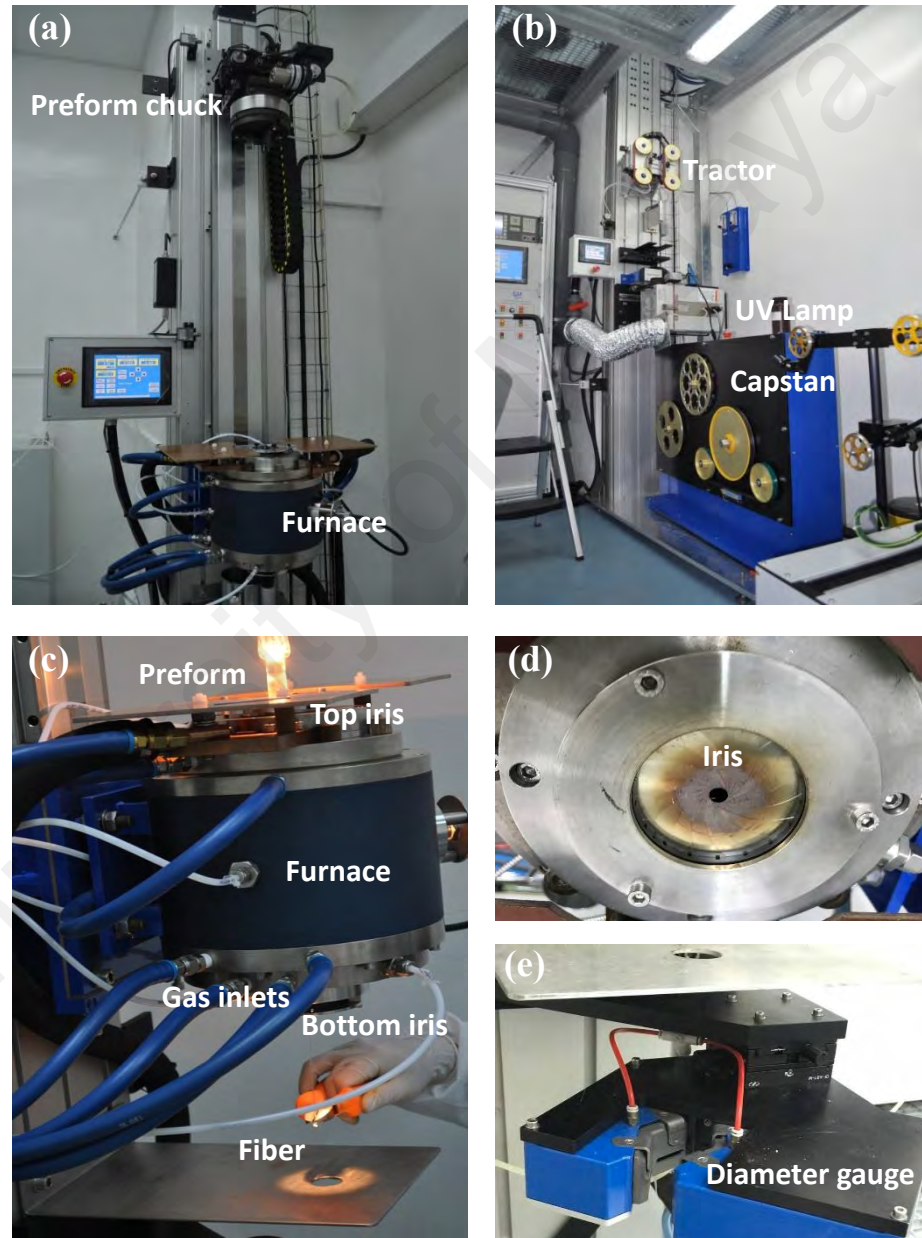


Figure 2.2: Actual photo of fiber drawing tower in Flat Fiber Laboratory, University of Malaya, Kuala Lumpur, Malaysia (a) Top floor (b) Lower floor (c) Furnace (d) Iris (e) Diameter gauge.

However, graphite has a high rate of oxidation at high temperature so it requires an oxygen free atmosphere (Payne & Gambling, 1976). To ensure an inert atmosphere inside the furnace, argon gas is used to purge the furnace in order to prevent any impurities and oxides built-up in the furnace (Barton *et al.*, 2005). Since any dust inside the furnace may cause surface flaws on the preform, the atmosphere inside the furnace should be maintained clean (Izawa & Sudo, 1987 & Kurkjian *et al.*, 1989). Inside the furnace, energy transport is done through radiative and convective heat exchange between the furnace wall and the preform (Barton *et al.*, 2005).

The preform is loaded into the furnace through its top iris, which is an opening on top of the furnace that can be adjusted according to the preform size. The furnace length is approximately 210 mm with the graphite heating element measuring 80 mm. Inside the furnace, the heating zone is approximately located from 120 mm to 154 mm when measured from the top iris, making the length of heating zone approximately 34 mm. The argon gas is flowed into the furnace via a side inlet and the furnace temperature is measured from a pyrometer mounted at the side of the furnace. The pyrometer has a temperature range of 350 °C – 2500 °C with a resolution of 1 °C. It should be noted that the furnace temperature measured through the pyrometer is not the absolute temperature but is dependent on the emissivity of the preform material and the alignment of the pyrometer (Furusawa, 2003). It is important to ensure that the furnace temperature is relatively accurate and stable, as any temporal variation may affect the final diameter of the fiber.

As the fiber exits the furnace through the bottom iris, the diameter of the bare fiber is measured using a high precision laser diameter measurement system by Zumbach (ODAC 15XY-J) that is mounted under the furnace. The measurement system has dual axis

scanners (USYS 2100) which can measure two diameters at a perpendicular direction from 0.10 mm (100 μ m) to 16.00 mm.

Next, the fiber is coated by acrylic polymer at the coating assembly unit which consists of a stainless-steel coating die set (which allows a maximum diameter of 375 μ m) and UV lamp (where the maximum temperature of its heating circuit is 80 °C). The coated polymer is then cured by a UV curing system (Fusion VPS 600). The power of the curing system can be varied from 25% to 100%. The fiber is then pulled into the tractor at the draw speed specified during the drawing process. The fiber capstan and drum winder unit are used to wind the fiber into a spool. There is a built-in tension monitor in the capstan. In addition, the drawing tower is also equipped with extra pipe inlets for vacuum and nitrogen gas.

2.2.2 Fiber drawing process

The processes in a fiber drawing can be divided into three major zones, which are heating zone, cooling zone and coating zone as shown in Figure 2.3 (Paek, 1999, Oh & Paek, 2012 & Jaluria, 2018). The study of the heating zone allows us to characterize the drawing parameters for flat fiber fabrication. Further details on the heating zone is discussed in Section 2.2.3.

The cooling and coating zones are only briefly described in this thesis as they are more relevant for commercial optical fiber fabrication which require high speed drawing for volume production. The cooling zone can further be divided into natural cooling and forced cooling (Vaskopoulos *et al.*, 1995 & Mawardi & Pitchumani, 2010). The temperature of the fiber in the cooling zone play a role in the quality of the coating (Paek, 1999, Yoo & Jaluria, 2006 & Oh & Paek, 2012). Thus, there must be a sufficient distance between the furnace and the coating applicator to allow the fiber to be effectively cooled before reaching the fiber coating applicator (Paek, 1999 & Oh & Paek, 2012). For high

speed fiber production, a higher draw tower allows for sufficient cooling period. In the cooling zone, the fiber strength weakened when the draw speed increased and this may be due to generation of defects on the glass surface by the cooling process (Kamo *et al.*, 2006).

Fiber coating is used to add physical protection to the fiber (Skutnik, 1989). It also adds tensile strength to the fiber (Paek, 1986) and is necessary to protect the fiber surface from contamination and damage (Paek, 1999). The draw speed during the drawing process is limited by the coating speed (Izawa & Sudo, 1987).

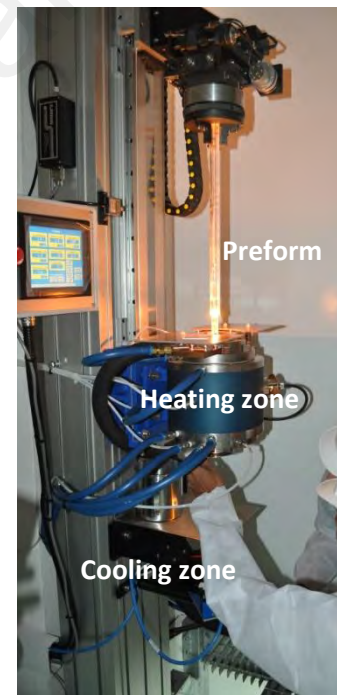
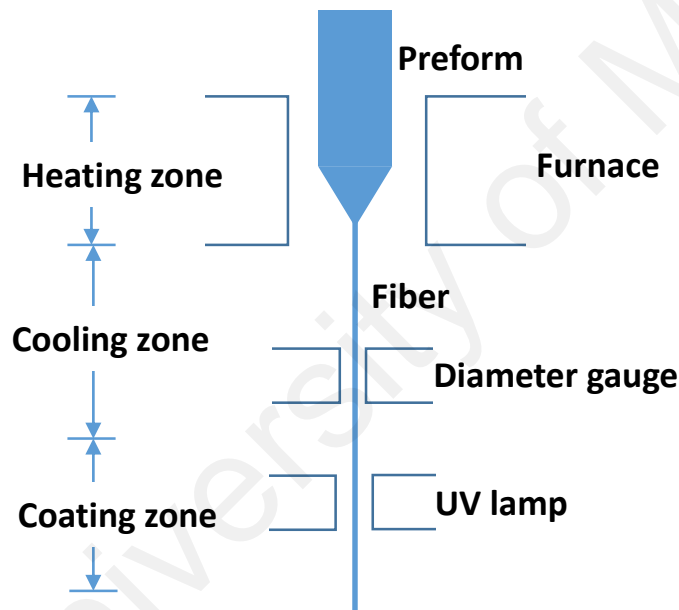


Figure 2.3: Three major zones during fiber drawing process.

The fiber drawing process starts with the heating of a preform inside a furnace. This is done by loading the preform vertically in the furnace with a temperature that is suitable to soften the preform. The furnace temperature chosen is dependent on the preform material and the type of dopant material used for the fiber core as the temperature affects the viscosity of the preform material. Viscosity is used to describe resistance to flow of melted glass and will be further discussed in Section 2.2.3.3 on the physical and material

properties of glass. For simplification, the analysis in this chapter assumes a silica based preform unless otherwise stated. Silica glass is an amorphous solid material that exhibits glass transition, which is a condition that allows a change from a hard state into a viscous state as the temperature of the material is increased (Shelby, 2005).

Inside the furnace in the heating zone, the preform is peripherally heated and drawn along its axial direction (Paek & Runk, 1978 and Cheng & Jaluria, 2004). When the preform passes through the heating zone, the surface temperature of the preform is increased, causing its viscosity and surface tension to decrease (Yin & Jaluria, 2000). The preform then reaches its softening temperature, causing the viscosity to decrease dramatically (Paek & Runk, 1978). The softening of the preform and the deformation caused by the draw tension will gradually reduce the preform diameter and shape inside the furnace. As the surface temperature of the preform exceeds the softening temperature of the preform material (Choudhury & Jaluria, 1998a), the necking process begins. With the low viscosity, together with the extensional deformation caused by the draw tension, the preform shape will narrow down sharply to yield a neck down profile (Paek & Runk, 1978, Lee & Jaluria, 1997, Choudhury & Jaluria, 1998a, Choudhury & Jaluria, 1998b Cheng & Jaluria, 2004 and Mawardi *et al.*, 2010). The final diameter and shape of the drawn optical fiber are regulated by the law of mass conservation (Paek & Ruck, 1978 and Mawardi & Pitchumani, 2010).

2.2.3 Neck down region

The neck down region is studied in detail in this thesis as this is where the critical deformations during fiber drawing occurs. The neck down profile is an important consideration in the fiber drawing process as it determines the overall quality (mechanical and optical characteristics) of a fabricated fiber such as diameter uniformity, strength, refractive index profile and light attenuation (Paek & Runk, 1978 and Cheng & Jaluria,

2004). In addition, the defect concentrations in a fiber is also dependent on the thermal and material flow process in this neck down region. The neck-down profile is governed by:

1. Heating zone length (Choudhury & Jaluria, 1998a, Cheng & Jaluria, 2002 and Cheng & Jaluria, 2005).
2. Drawing process parameters, namely furnace temperature, preform feed speed (speed of the preform entering the furnace) and optical fiber draw speed (speed of the optical fiber exiting the furnace). These parameters will be studied in detail in this thesis in Chapter 3.
3. Physical and material properties of the silica glass which affects the glass viscosity (Yin & Jaluria, 2000). The viscosity depends on the temperature profile and the external gas flow velocity in the furnace (Paek & Runk, 1978 and Choudhury & Jaluria, 1998b).

Each of these will be discussed in more detail in the next sub-sections.

2.2.3.1 Heating zone length

The heating zone length is affected by the furnace design, namely its geometry (length and diameter), type and length of heating element, number and position of irises on the furnace. The study of the furnace design parameters affecting the heating zone length are beyond the scope of this thesis as the heating zone length and heating element type are fixed in this research work. The furnace design directly influences the temperature profile of the furnace and the neck down region (Choudhury & Jaluria, 1998a, Cheng & Jaluria, 2002 and Cheng & Jaluria, 2005). In addition, the neck shape in the neck down region is also affected by different temperature distributions which occur due to different draw speed (Paek & Runk, 1978). The shape of the neck down region is partly controlled by the furnace temperature, which has a specific temperature profile depending on the

furnace type and geometry and heating element used. To simplify this analysis, it is assumed that the temperature profile is Gaussian (Paek & Runk, 1978 and Choudhury & Jaluria, 1998a) which means that the peak temperature occurs at half of the neck down length of the furnace. Knowledge of the temperature profile is important as the fiber geometry is sensitive to the temperature profile (Voyce *et al.*, 2009).

The findings from Paek & Runk, 1978 on the temperature profile in a furnace are:

1. The temperature profile obtained for a heating element using radiative transfer is assumed to be a measure of the relative heat flux distribution along the center of the furnace and can be approximated as Gaussian distribution.
2. The temperature distributions along the neck down region changes according to the draw speed. The neck down length for three different draw speeds also varies, with the highest draw speed giving the longest neck down length.

Cheng & Jaluria, 2004 studied the parabolic and Gaussian temperature profile of a furnace. Their findings are:

1. Based on the parabolic temperature distribution, the maximum draw speed at a given maximum furnace temperature could be restricted by heating zone length inside furnace because the temperature must be higher than the softening point in the neck down region. High draw tension will cause viscous rupture as the glass tension is higher than the viscous strength of the fiber.
2. The Gaussian temperature distribution was also studied. It was found that a higher draw temperature is needed for fiber drawing at higher draw speeds when compared to the parabolic temperature distribution.

In Choudhury & Jaluria, 1998a, for comparison with experimental results, the furnace is assumed to have a Gaussian temperature profile using a cylindrical graphite furnace.

The maximum temperature is referred as the furnace temperature. For this type of furnace, the two major parameters affecting fiber drawing are fiber draw speed and furnace temperature. In this work, the temperature profile for the furnace design is assumed to be Gaussian temperature profile.

2.2.3.2 Drawing process parameters

The neck down profile is a function of the drawing conditions and may vary substantially for typical conditions over which optical fibers are drawn (Yin & Jaluria, 2000). Paek & Runk, 1978 investigated the neck-down profile during an optical fiber drawing and concluded that the parameters affecting diameter variations in the neck down region are furnace temperature profile and viscosity of glass distribution, neck down shape and fiber drawing tension. The main findings from the neck-down process by Paek & Runk, 1978 are:

1. The neck shape can be numerically predicted using an iterative scheme by solving the mass conservation equation and it is a function of the drawing tension, viscosity and velocity distribution along the axial direction.
2. As the molten glass preform is pulled down from the furnace, the fiber tension, γ experienced by the glass is defined as:

$$\gamma = 3\mu A \frac{\delta U_d}{\delta d} \quad (2.1)$$

where μ is the viscosity, A is the cross-section area of the preform, U_d is the draw speed of the fiber and d is a given arbitrary axial location.

The main findings on the neck-down process by Choudhury & Jaluria, 1998a which are related to this work are:

1. The necking shape can be determined by the location of the heating gas flow entrance and the overall energy transport process. The surface temperature distribution decreases with increasing velocity which causes the preform to reach its softening temperature much later.
2. The detailed discussion on forces at the neck down region during the drawing process can be referred to Choudhury & Jaluria, 1998a. At the beginning of the neck down region, the force (mainly due to gravity) is significant.
3. There is a practical range of draw speeds and furnace temperature conditions for feasible fiber drawing. This range is dependent on the size of the required fiber diameter.

The drawing parameters affecting the neck down region such as draw speed, feed speed and furnace temperature will be discussed in more detail in Chapter 3.

2.2.3.3 Physical and material properties of glass

When forming glasses, viscosity is an important parameter to determine the melting conditions for a bubble-free, homogeneous melt that is also free from internal stress (Shelby, 2005). Viscosity, μ can be defined as the ratio of applied shearing force and the liquid rate of glass and is given by Equation 2.2 (Shelby, 2005).

$$\mu = \frac{F_t d}{A v} \quad (2.2)$$

where F_t is the tangential force applied to two parallel planes of area A which are separated by a distance d and v is the relative velocity of the two planes. For the drawing of an optical fiber, Equation 2.2 is modified to Equation 2.3.

$$\mu = k \frac{\gamma L}{A U_d} \quad (2.3)$$

where μ is the viscosity (in Pa. s), γ is the drawing tension (in N), L is the heating zone length (in m), A is the preform area in the heating zone (in m²) and U_d is the draw speed (in m/s) while k is a constant derived from experiment. The temperature dependence of viscosity can be derived by an Arrhenian equation as shown in Equation 2.4 (Shelby, 2005).

$$\mu = \mu_o e^{\Delta H_\mu / RT} \quad (2.4)$$

where μ_o is a viscosity constant, ΔH_μ is the activation energy for viscous flow, R is the gas constant and T is the temperature in K. This equation is limited for the viscosity range of 10⁹ Pa.s. to 10¹³ Pa.s. For an equation that fits the whole viscosity range, the Fulcher equation, shown in Equation 2.5 (Doremus, 1994 and Shelby, 2005) is more commonly used.

$$\mu = \mu_o e^{B/(T-T_o)} \quad (2.5)$$

where μ_o and B are not dependent on temperature. B was used to replace ΔH_μ in Equation 2.4.

Equation 2.5 can also be written in the form shown in Equation 2.6 (Shelby, 2005).

$$\log \eta = -A + \frac{B \times 10^3}{T - T_o} \quad (2.6)$$

where the constant A replaces μ_o and T and T_o are in Celcius.

For a fused silica, the viscosity based on Equation 2.5 is modified to become Equation 2.7 (Xue *et al.*, 2006 and Bansal & Doremus, 1986). The following equation is true for fused silica with less than 10 ppm of water and for absolute temperature of 1600 °C to 2500 °C.

$$\log_{10} \mu \approx -6.24 + \frac{26900}{T} \quad (2.7)$$

where T is the absolute temperature (in K).

At a lower absolute temperature of 1000 °C to 1400 °C, the following viscosity equation applies (Bansal & Doremus, 1986):

$$\log_{10} \mu \approx -12.5 + \frac{37300}{T} \quad (2.8)$$

Figure 2.4 shows viscosity (log) versus reciprocal temperature for pure silica and various doped silica fibers.

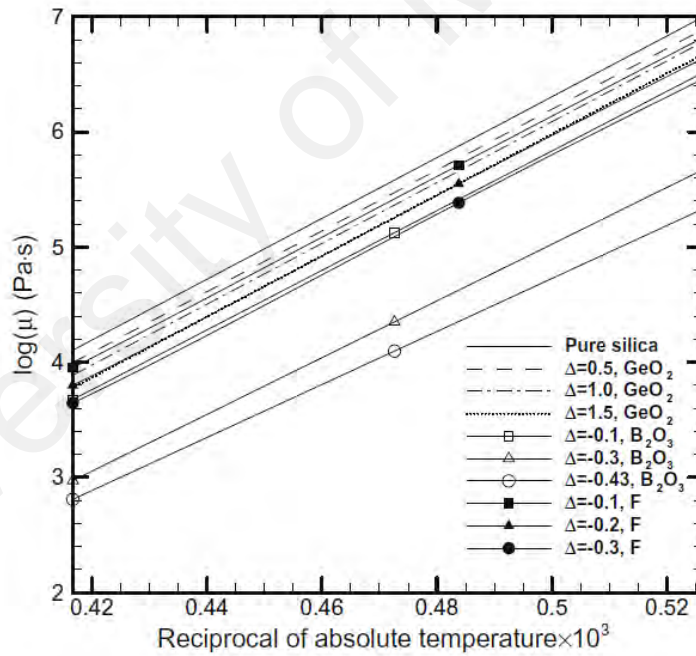


Figure 2.4: The viscosity versus reciprocal of absolute temperature for pure silica and various doped silica fibers (Reproduced from Chen & Jaluria, 2009 with permission).

The viscosity of the preform material can be used to estimate a suitable furnace temperature during the drawing process. During optical fiber drawing, the viscosity of fused silica is recommended to be between 10^3 Pa.s and $10^{6.6}$ Pa.s (Shelby, 2005). Beyond this range, the glass is found to be too hard and difficult to work on.

Figure 2.5 shows the viscosity versus temperature for a fused silica, calculated using Equation 2.8. The suitable fiber drawing temperature range for a fused silica preform is estimated to be from 1900 °C to 2200 °C. The viscosity varies from $10^{3.64}$ Pa.s to $10^{5.14}$ Pa.s for this temperature range.

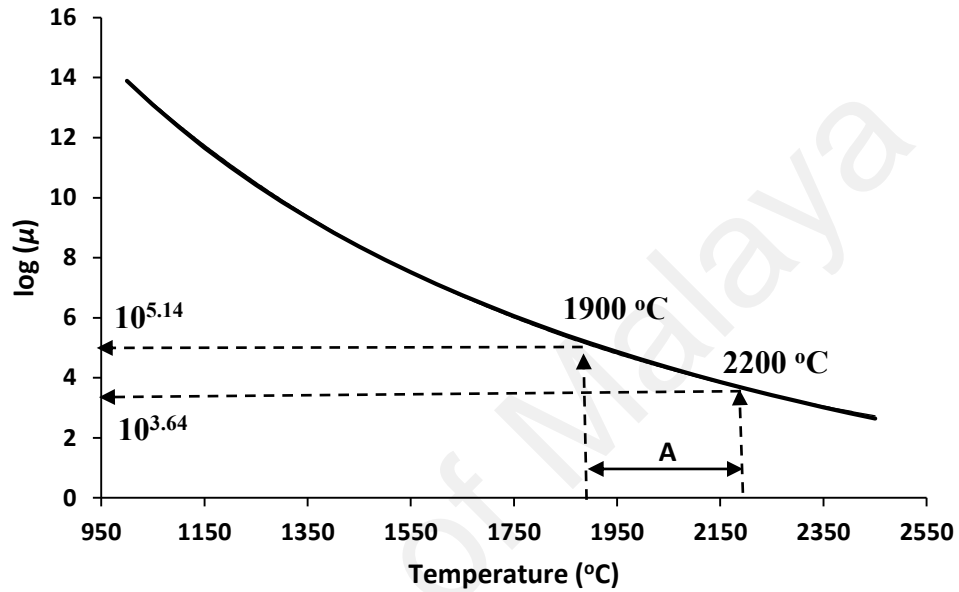


Figure 2.5: Viscosity (log) versus temperature (where A is the temperature range of 1900 °C to 2200 °C).

The neck down shape, $R(z)$ can be predicted by solving the mass, momentum and energy equations simultaneously (Oh & Paek, 2012). The energy and momentum equations are coupled by the viscosity equation of silica glass which is a function of temperature (Paek, 1999). The boundary conditions for the neck down region are the two points where the deformation of the preform begins and ends (Paek, 1999).

The numerical approach to solve the neck down profile governing equations is beyond the scope of this thesis. Further analysis on the equations including its physical model, boundary conditions and solutions can be found in Paek & Runk, 1978, Paek, 1999, Cheng & Jaluria, 2004, Cheng & Jaluria, 2005, Yang & Jaluria, 2009, Cheng & Jaluria, 2002, Mawardi & Pitchumani, 2010 and Oh & Paek, 2012.

From the conservation of mass, the neck down shape $R(z)$ as illustrated in Figure 2.6 can be iteratively defined using computational methods as (Paek, 1999):

$$R(z) = R_1 \sqrt{\frac{U_f}{U_z}} \quad (2.9)$$

where R_1 is the preform outer radius, U_f is the feed speed and U_z is the speed at z . Figure 2.6 shows the physical model of the neck down profile where R_2 is the fiber radius, L is the heating zone length and U_d is the draw speed. The end of the neck down region occurs when the diameter reaches 5% of the original preform diameter (Cheng & Jaluria, 2002). After that, the region is called as draw down region and has a more gradual reduction (Cheng & Jaluria, 2002).

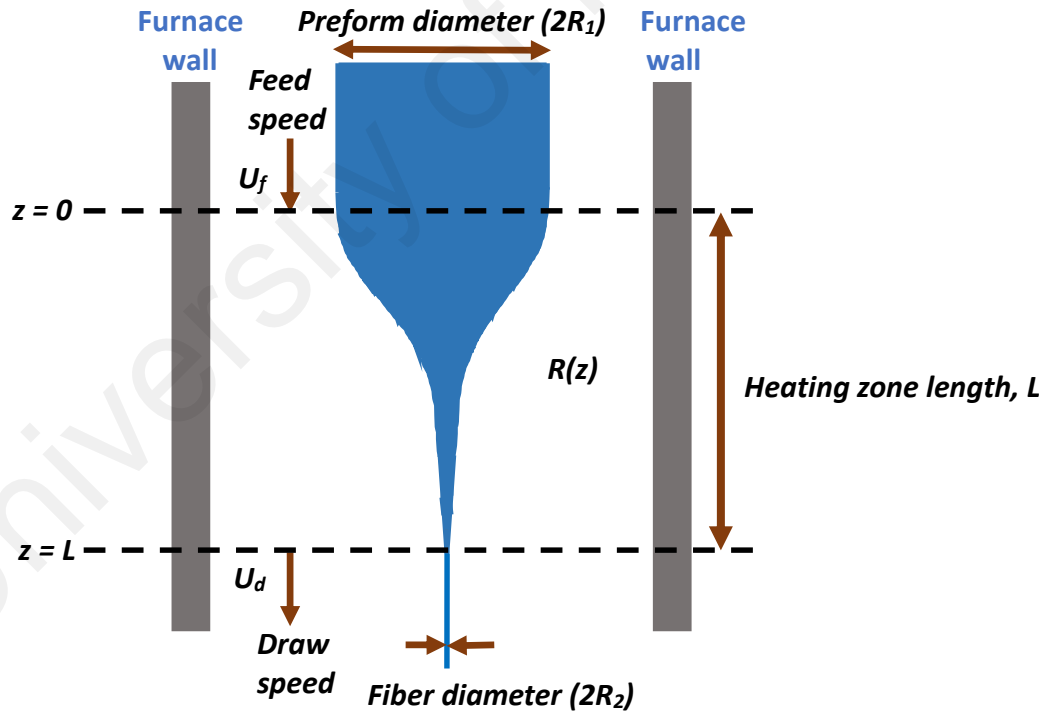


Figure 2.6: Physical model of the neck down profile for optical fiber drawing.

As the preform softened, the fiber is drawn down due to its reduced viscosity and the forces acting on it. The following force balance equation (based on mass conservation

law) describes the forces that act on the fiber at a particular axial location z as shown in Figure 2.6 (Choudhury & Jaluria, 1998a):

$$F_\gamma + F_g = F_\mu + F_\zeta + F_I + F_e \quad (2.10)$$

where F_γ is the draw tension, F_g is the force due to gravity, F_μ is the force due to viscous stress, F_ζ is the force due to surface tension, F_I is the force due to inertia and F_e is the force due to the shear force exerted by the external gas velocity. Choudhury & Jaluria, 1998a summarized the forces that act on the fiber in the neck down region as:

1. The force due to shear force is small and therefore can be neglected.
2. Viscous stress force is not constant throughout the axial direction z .
3. The force due to inertia is almost negligible and the surface tension force is very small.
4. The force due to gravity is important and cannot be ignored.

Therefore, considering this finding, the main forces acting on the fiber that allows it to be drawn down in the neck down region is the force due to gravity and draw tension. These two forces, combined with the reduced viscosity of the silica glass, cause preform deformation to occur and allows the fiber to be pulled down from the lower iris of the furnace.

2.3 Fabrication of Capillary

Capillaries are the building blocks for microstructured fibers, also known as holey fibers. In microstructured fibers, a pattern of holes run along the length of the fibers and varying these patterns allow a variety of optical effects to be produced (Xue *et al.*, 2005). One of the optical effects that can be produced is endlessly single mode where only a single mode is transmitted regardless of the wavelength (Fitt *et al.*, 2002). The

microstructured fibers are fabricated by stacking dozens to hundreds of capillaries inside a hollow preform, before drawing it into a cane and finally drawing the cane to a fiber (Laegsgaard & Bjarklev, 2006 and Luzi *et al.*, 2012). This method is known as the stack-and-draw method.

For optical fiber drawing, a solid, collapsed preform is used. The fiber diameter can be predicted accurately for optical fiber drawing based on mass conservation law. In order to draw capillaries, hollow preform tubes must be used. The general drawing steps for a capillary is similar to the drawing process of an optical fiber. The preform used for capillary drawing can either be silica or polymer such as polymethylmethacrylate (PMMA) (Fitt *et al.*, 2002, Barton, 2004 and Xue *et al.*, 2005). For capillary drawing, a two-stage drawing process may be employed to have better control of the final capillary diameter (Xue *et al.*, 2005). In a two-stage drawing, the first stage involved drawing the hollow preform to an intermediate cane and the dual stage involved drawing the cane to a final fiber dimension (Xue *et al.*, 2005 and Argyros, 2009).

The complete mathematical and numerical modelling for the fabrication of capillaries is beyond the scope of this thesis. Further analysis can be found in Fitt *et al.*, 2001, Fitt *et al.*, 2002, Xue *et al.*, 2005, Yang & Jaluria, 2009, Voyce *et al.*, 2009, Luzi *et al.*, 2010, Luzi *et al.*, 2011 and Kostecki *et al.*, 2013. A summary of the mathematical modelling taken from Fitt *et al.*, 2002 is given next to present readers with a general understanding of parameters that can be controlled during the fabrication process of capillaries.

The main findings from Fitt *et al.*, 2002 are:

1. The mathematical modelling (using fluid-mechanics model) for the fabrication of capillaries begins with the Navier-Stokes (Fitt *et al.*, 2002) and convection-diffusion equations (Fitt *et al.*, 2002). The flow of the molten glass is assumed to

be axisymmetric and linear incompressible liquid. The heat transfer is through diffusive and convective processes. The boundary conditions assume that the thermal conductivity of air is much lower than the thermal conductivity of glass so the fiber is essentially insulated on its inner surface. Without surface tension and internal hole pressurization, the initial fiber geometry can be preserved. The model gives a prediction for viscosity dominated parameters such as the inner and outer diameter of the capillary and the speed during the drawing process.

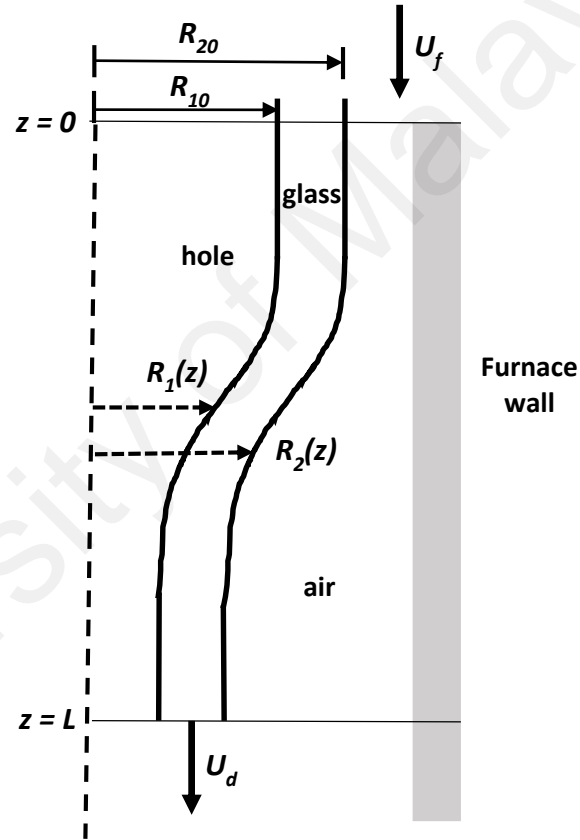


Figure 2.7: Physical model of the neck down profile for capillary drawing (Fitt *et al.*, 2001).

During the capillary drawing process, the relative dimensions and geometry changes can be deduced by ratio of the preform radius (ratio of hole radius to outer radius). The collapse ratio, C_r can be described as (Fitt *et al.*, 2001):

$$C_r = 1 - \frac{R_1(z)/R_2(z)}{R_{10}/R_{20}} \quad (2.11)$$

where $R_1(z)$ is the inner radius neck down profile as seen in Figure 2.7, $R_2(z)$ is the outer radius neck down profile, R_{10} is the inner radius for the capillary and R_{20} is the outer radius for the capillary. The forces that act at a horizontal cross-section of the preform/fiber in the neck down region is defined as (Yang & Jaluria, 2009):

$$F_\gamma = F_\mu + F_\zeta + F_I - F_g \quad (2.12)$$

where F_γ is the draw tension, F_μ is the force due to viscous stress, F_ζ is the force due to surface tension over two free surfaces, F_I is the force due to inertia and F_g is the force due to gravity. The draw tension is important to determine the final characteristics (fiber strength and optical quality) and geometry of the final capillary.

The draw tension and force due to gravity represents the pulling force exerted at the capillary specifically at the neck-down region when the diameter deformation occurs due to the lower glass viscosity. If the draw tension is not kept under a suitable threshold, fiber breakage may occur. One of the parameters during the fiber fabrication process, draw speed, is linearly proportional to the draw tension. Different draw speed gives different temperature distributions, causing different neck down shapes. A low draw speed (which causes low draw tension) in combination with a high temperature (low viscosity) may result in fiber break because of the mobile state of glass and capillary instability. Further details on the drawing parameters affecting the fabrication of capillaries will be discussed in Chapter 3.

2.4 Fabrication of Flat Fiber

The initial drawing steps to draw a flat fiber is similar to the drawing process of a capillary because the preform structure is the same, which is hollow. The hollow preform is then heated in the furnace at its softening temperature. Once the preform has softened, the drop down occurs and capillary is then pulled down from the bottom of the furnace.

When the drawing process has stabilized in terms of the feed speed and draw speed producing the desired diameter, the air in the hollow preform is pumped out by a vacuum pump which is connected to the top of the hollow preform.

For flat fibers, the forces that act at a horizontal cross-section of the preform/fiber in the neck down region is defined as:

$$F_\gamma = F_\mu + F_\zeta + F_I + F_v - F_g \quad (2.13)$$

where F_γ is the draw tension, F_μ is the force due to viscous stress, F_ζ is the force due to surface tension over two free surfaces, F_I is the force due to inertia, F_g is the force due to gravity and F_v is the force due to the vacuum pressure.

As discussed previously in Section 2.2.3, the resultant force exerted on the glass surface particularly at the neck-down region where the viscosity is low, deformed the profile of the neck-down region. This profile deformation is highly dependent on the glass viscosity. For flat fiber drawing, there is an additional force due to vacuum acting on the fiber as shown in Equation 2.13 and the resultant forces acting on the capillary (together with the low viscosity) flatten the drawn fiber.

The force due to vacuum pressure is more significant than the other forces. When vacuum is applied to the capillary, the air pressure inside the preform becomes lower than the outer layer. The sudden loss of air inside the capillary hole will cause the capillary to collapse, forming a fiber with a planar geometry as the glass exits the furnace. However, if the force due to vacuum pressure is higher than the draw tension, it can cause the capillary to over-collapse, giving a deformed shape instead of a planar shape. Thus, the vacuum pressure should be controlled to ensure that it is just sufficient to collapse the capillary.

In this case, the flat fiber is defined when the cross section of the drawn optical fiber changes from circular to planar in shape. Usually, the fabricated flat fiber is slightly elliptical in shape since the original preform is circular. The flat fiber is commonly fabricated using a single-stage drawing. The flat fiber dimensions can be approximated from its preform tube dimensions. Assuming a preform tube with an inner diameter ID and an outer diameter OD as shown in Figure 2.8 (a), the ideal flat fiber dimensions (with w_c as the width of the core, w as the width of the flat fiber and t as the thickness of the flat fiber) as shown in Figure 2.8 (b) can be described by the following equations (Webb, 2012):

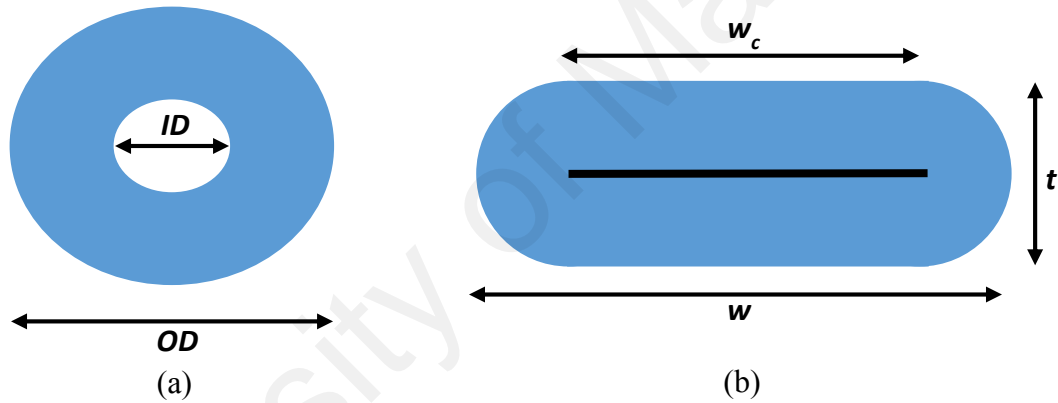


Figure 2.8: Preform tube dimensions and flat fiber dimensions (Webb, 2012).

$$t = D_o - D_i \quad (2.14)$$

$$w_c = \frac{\pi}{2} \times D_i \quad (2.15)$$

$$w = w_c + t \quad (2.16)$$

For Equations 2.14 – 2.16, the core thickness is approximated as zero for simplicity (Webb, 2012). Thus, in a doped preform, the core thickness may affect the final flat fiber dimension.

2.5 Practical Limitations in Flat Fiber Drawing

In the fabrication of flat fibers, it is important to control and minimize fiber deformations. The types of flat fiber defects that can occur during the drawing process are brittleness which causes fibers to break during the fabrication process, non-uniform fiber dimension, surface defects on the fiber, excessive collapse of the fiber, holes in the flat fiber and deformed flat fiber. Brittle fiber is defined as a fiber that breaks easily when stress is applied. This happened due to surface flaws on the fiber (Paek, 1986).

The defects in the flat fiber occur due to a number of reasons including non-optimized furnace temperature, non-optimized vacuum pressure, non-optimized draw speed and feed speed, defects in preform and sealing issues for the vacuum pressure. Experimental work to obtain optimized drawing parameters for fibers are time consuming and expensive (Cheng & Jaluria, 2005). In Yang & Jaluria, 2009, a numerical model was developed to identify the feasible domain for drawing process where the geometry of the fiber is maintained from collapse and rupture. The ability to control and prevent the fiber deformations allows us to produce, on a repeatable basis, good quality flat fiber samples.

In general, Choudhury & Jaluria, 1998a has identified several reasons that may cause defects in optical fibers (the analysis may also be used for defects in capillaries and flat fibers), which are:

1. Fiber may break due to viscous rupture, which occurs due to lack of material flow.

This lack of material flow occurs at high viscosity whenever the furnace temperature is below the glass softening temperature. Viscosity may increase tremendously when the surface temperature decreases and goes below softening point. The viscosity fluctuation is caused by an increase in the draw speed.

2. At very high temperature above the softening temperature together with low speed drawing process, the draw tension becomes very small due to low value of

viscosity. This causes fiber to break into drops, a process called capillary instability. Unexpected variations in the drawing parameters may also result in large changes in the drawing process.

3. Defect concentrations is high at high draw speeds and furnace temperature.

Chen & Jaluria, 2009 has explained further about E' defects, which are:

1. The E' defect is a point defect, which is generated at a high temperature furnace during the drawing process and causes transmission loss and mechanical strength degradation. The E' defects are mainly generated at the upper neck down region where the temperature undergoes a drastic increase.
2. Fiber quality is degraded with increase in refractive index difference between core and cladding in terms of E' defects. The concentration of E' defects is highly non-uniform in the cross section, where it is larger in the core and smaller in the cladding.

Yin & Jaluria, 2000 also provided an extensive explanation on defects in optical fibers, which are:

1. During the fiber drawing process, point defects are generated at high temperatures and frozen in the fibers during the cooling process. Point defects cause transmission loss in the fiber and lower the mechanical strength of the fiber.
2. One drawing induced defect is the E' defect, which depend on the drawing temperature, draw speed and fiber diameter.
3. In silica glass, every oxygen site is a potential precursor and can lead to an E' defect. For pure silica, the initial concentration of E' defect is assumed to be zero. When one Si-O band is broken, one precursor diapers and one E' defect is generated.

4. The concentration of E' defects mainly occurs in the upper neck down region where the temperature undergoes a significant increase.
5. Concentration of E' defects increase with a decrease in the draw speed. This is due to the preform temperature being higher for lower draw speed. There is higher defect generation at higher temperature.
6. For low defect concentration, lower temperature level in the preform/fiber is necessary. Low temperature level can be achieved with higher draw speed and smaller preform diameter.

Further details on the thermodynamic behavior of point defects during the drawing process can be found in Hanafusa *et al.*, 1985.

2.6 Summary

The aim of this chapter was to provide the readers with a theoretical background on the fundamentals of optical fiber fabrication, specifically on optical fiber drawing. The fabrication of preforms was beyond the scope of this thesis. For optical fiber drawing, a detailed discussion was given on the components of the drawing tower, optical fiber fabrication process and the factors affecting the neck down region in the furnace. The three main factors affecting the neck down region are heating zone length, drawing process parameters and physical and material properties of glass. The mathematical and numerical modelling of the drawing process in the neck down region for optical fibers and capillaries was not discussed in detail as it was beyond the scope of this thesis. The fiber drawing process for capillaries and flat fibers were also presented. Finally, practical limitations in flat fiber drawing was discussed. In the next chapter, the effects of drawing parameters for flat fiber fabrication using a pure silica preform tube will be investigated.

CHAPTER 3: EFFECT OF DRAWING PARAMETERS ON THE FABRICATION OF FLAT FIBERS

3.1 Introduction

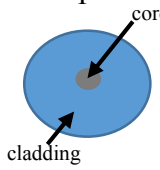

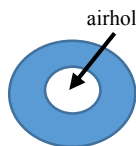

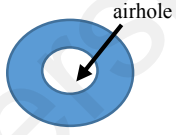
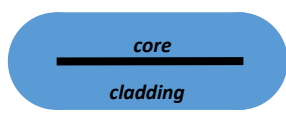
In Chapter 2, an introduction to the optical fiber drawing process had been given and fabrication parameters that can be controlled during an optical fiber drawing, namely furnace temperature, feed speed and draw speed had been identified. In this chapter, a pure fused silica preform tube will be used to investigate the effects of these fabrication parameters on the final fabricated fibers. In addition, other parameters specific to flat fiber drawing such as vacuum pressure and preform wall thickness will also be investigated. Preform wall thickness, which is the physical property of the preform, also affects the neck down profile as has been discussed in Section 2.2.3. At present, there is no known study on the effect of preform wall thickness on the fabrication of capillaries and flat fibers. The control of these parameters, in particular preform thickness, is important in order to fabricate flat fibers with a specific size and dimension.

The ability to accurately fabricate flat fibers of a certain dimension would ensure the required optical and mechanical properties are achieved. Although using a pure silica preform would mean that there is no core in these flat fibers, it can still be used for sensor applications and others (i.e. dosimetry purposes (Alawiah *et al.*, 2015)). More importantly, the results can be used as the fabrication stepping stone for fabrication using doped silica preform tube.

To begin this study, a brief introduction to fused silica is given including its properties, to give the reader an understanding of why fused silica preform is chosen. Next, the fabrication parameters for a silica based optical fiber and capillary drawing are studied since there is no known literature on the detailed fabrication study of flat fiber. Some of the fabrication parameters (including any constraints and limitations) for optical fiber and

capillary drawing is similar to flat fiber drawing since the preform material (silica) is the same. The flat fiber will initially be in capillary form before vacuum is applied to flatten it. Thus, the initial study of fabrication parameters affecting capillary drawing is useful for flat fiber fabrication. The basic differences between optical fiber drawing, capillary drawing and flat fiber drawing are summarized in Table 3.1.

Table 3.1: Drawing process comparison.

Drawing type	Preform geometry	Drawing parameters	Fabricated fiber
Optical fiber drawing	Solid preform 	<ul style="list-style-type: none"> Furnace temperature Draw speed Feed speed 	Optical fiber 
Capillary drawing	Preform tube 	<ul style="list-style-type: none"> Preform wall thickness Furnace temperature Draw speed Feed speed 	Capillary 
Flat fiber drawing	Preform tube 	<ul style="list-style-type: none"> Vacuum pressure Preform wall thickness Furnace temperature Draw speed Feed speed 	Flat fiber 

In this chapter, the literature review of the fabrication parameters affecting optical fiber and capillary drawing are given. Detailed methodology of the experimental work is presented. Next, the experimental results and discussion on the fabrication parameters involved are presented. The parameters investigated in this chapter are preform wall thickness, furnace temperature, draw speed, feed speed and vacuum pressure.

3.2 Literature Review

3.2.1 Fused silica

Fused silica (also known as vitreous silica) with the structure silicon dioxide (SiO_2) is the basic material used in the fabrication of optical fibers due to its high purity, high temperature stability, low thermal shock, low electrical conductivity and dielectric loss, high chemical durability and high optical transparency (Bansal & Doremus, 1986). It is also the material most commonly used in optical fibers for telecommunication purposes due to its low transmission loss (Chen & Jaluria, 2009). Pure vitreous silica with different water content gives rise to different softening temperature (Hetherington *et al.*, 1964). Table 3.2 illustrates the softening temperature for pure silica with different wt% of hydroxyl (Hetherington *et al.*, 1964). A pure silica preform with a higher water content requires a lower softening temperature. However, a preform with a lower water content is desirable to reduce the effects of extrinsic absorption, which causes attenuation in optical fiber communication systems (Senior & Jamro, 2009). Optical fiber drawing becomes impossible if it is drawn below the softening temperature (Yin & Jaluria, 2000). This is because the fiber drop down process does not occur below the softening temperature.

Table 3.2: Softening temperature for pure silica with different water content.

Hydroxyl (wt%)	0.0003	0.04	0.12
Softening Temperature (°C)	1670	1596	1594

For all the experiments in this chapter (unless otherwise stated), Suprasil F300 (Heraeus) preform tubes, a high purity synthetic fused silica substrate tube (with no added dopants) were used. The Suprasil® 300x family of materials has the combination of ultra-low total metal impurities (< 1 ppm) and low OH (< 1 ppm) that result in no absorption

bands from the visible to the IR spectral region (Heraeus data sheet). The softening temperature for Suprasil F300 is approximately 1600 °C (Heraeus data sheet).

3.2.2 Drawing parameters

Cheng & Jaluria, 2004 investigated the feasible combinations of drawing parameters during optical fiber drawing process using a cylindrical graphite furnace. The three important drawing parameters are furnace temperature, draw speed and heating element length. The boundaries of the domain are determined by viscous rupture and flow instability.

Other than that, the effects of draw speed and furnace temperature on the fiber diameter and draw tension were also numerically studied by Mawardi *et al.*, 2010. They found that a higher furnace temperature and a higher draw speed decreased the fiber diameter. However, the draw tension increased with draw speed and decreased with higher furnace temperature.

According to Fitt *et al.*, 2001, the geometry of a capillary can be modified by controlling the parameters used in the drawing process which are temperature of the furnace, feed speed and draw speed. When high temperatures and low draw speed are used, air holes in the cladding reduce in size and may close completely due to surface tension effects. Fitt *et al.*, 2001 have developed a mathematical model for capillary drawing which includes effects of surface tension, viscosity and internal hole overpressure. The simplified solutions (derived from Navier-Stokes equations) that govern the drawing of a capillary when considering time-independent solutions and flow that is viscosity dominated are shown in Equations 3.1, 3.2 and 3.3 (Fitt *et al.*, 2001).

$$u_0 = u_f e^{\beta x/L} + \frac{2\gamma L e^{\beta x/L}}{3\mu\beta(h_{20}-h_{10})} \times \left[e^{-\beta x/2L} - 1 + \left(\frac{x}{L}\right) \left(1 - e^{-\beta/2}\right) \right] \quad (3.1)$$

$$h_1 = h_{10}e^{-\beta x/2L} + \frac{\gamma L e^{-\beta x/L}}{3\mu\beta U_f(h_{20}-h_{10})} \times \left[(3h_{20} - h_{10}) \left(1 - e^{\beta x/2L} \right) + \left(\frac{h_{10}x}{L} \right) e^{\beta x/2L} \left(e^{-\beta/2} - 1 \right) \right] \quad (3.2)$$

$$h_2 = h_{20}e^{-\beta x/2L} + \frac{\gamma L e^{-\beta x/L}}{3\mu\beta U_f(h_{20}-h_{10})} \times \left[(3h_{10} - h_{20}) \left(1 - e^{\beta x/2L} \right) + \left(\frac{h_{10}x}{L} \right) e^{\beta x/2L} \left(e^{-\beta/2} - 1 \right) \right] \quad (3.3)$$

where u_0 is the draw speed, h_1 is the inner diameter of the capillary, h_2 is the outer diameter of the capillary, h_{10} is the preform inner diameter, h_{20} is the preform outer diameter, U_f is the feed speed, U_d is the draw speed at L , L is the heating zone length, β is $\ln(U_d/U_f)$, μ is the glass viscosity, γ is the surface tension and x is the distance along the axis of the capillary.

Fitt *et al.*, 2001 shows that reduced capillary inner and outer dimensions are achieved at faster draw speed, higher temperature and lower feed speed. At a fixed furnace temperature, the model can predict the capillary diameter as a function of draw and feed speed. To predict the collapse of the holes, the collapse ratio, C as shown in Equation 3.4 can be used where $C = 1$ represent the capillary being fully collapsed to a solid rod while $C = 0$ represent the capillary geometry being completely preserved. They also found that the collapse ratio is sensitive to a temperature deviation of about 10 °C (Fitt *et al.*, 2001).

$$C = \frac{\gamma L}{\mu U_f \ln(U_d/U_f)} \left[\frac{h_{10} + h_{20}}{h_{10} h_{20}} \right] \quad (3.4)$$

Hole deformation patterns which is due to initial preform imperfection may occur during the drawing of microstructured optical fibers and may alter the fiber's optical properties include hole collapse, hole expansion, hole enlargement and hole shape changes (Xue *et al.*, 2006). These deformations can be controlled by the capillary

number, N_c , draw ratio, D_r and aspect ratio (ratio of preform radius over the neckdown length), ε as defined in Equations 3.5, 3.6 and 3.7 respectively (Xue *et al.*, 2006).

$$N_c \equiv \frac{\mu U_f}{\gamma} \quad (3.5)$$

$$D_r \equiv \frac{U_d}{U_f} \quad (3.6)$$

$$\varepsilon \equiv \frac{h_{20}}{L} \quad (3.7)$$

where γ is the surface tension coefficient of the material. The draw ratio shows the overall contraction in size while the aspect ratio shows the overall rate of deformation. Typical values for silica are 10^4 for draw ratio and $0.2 \sim 0.25$ for aspect ratio (Xue *et al.*, 2006).

In addition to drawing conditions, material properties can also affect changes in the hole shape. It is found that when silica was used (compared to PMMA), hole collapse is more dominant than hole expansion. During hole collapse, the hole is contracting faster than the surrounding preform and this difference caused stretching forces around the holes (Xue *et al.*, 2006).

Chen *et al.*, 2013 reported a model for predicting the hole sizes in fibers without knowledge of viscosity distribution along the neck down region. The outcome can be predicted based on pressure in the holes, drawdown ratio (fixed by the ratio of the preform feed rate and the fiber draw speed) and the draw stress in the fiber, with the surface tension as the sole material constant. A suitable choice of pressure and draw tension can produce holes of desired different sizes from a preform.

A summary of the literature review done on the fabrication parameters that affect the drawing conditions of optical fibers and capillaries is shown in Table 3.3.

Table 3.3: Summary of literature review for various drawing parameters.

Reference	Methodology	Type	Objective	Drawing parameters
Paek & Runk (1978)	Numerical modelling	Optical fiber (silica)	Maintain uniform fiber diameter	Temperature and viscosity distributions within the neck down region, neck down shape and draw tension
Choudhury & Jaluria (1998a)	Numerical modelling and experimental verification	Optical fiber (silica)	Identify practical ranges for draw speeds and furnace temperature	Draw tension, draw speed (6 m/s) and furnace temperature (1650 °C)
Paek (1999)	Numerical modelling	Optical fiber (silica)	Fiber drawing for large size preform and high speed drawing	Temperature distribution, draw speed and draw tension
Yin & Jaluria (2000)	Numerical modelling	Optical fiber (silica)	Numerical modelling for large diameter preforms and high draw speed (20 m/s)	Draw speed, neck down profile and furnace temperature
Fitt <i>et al.</i> , (2001)	Numerical modelling and experimental verification	Capillary (silica)	Modelling the fabrication of capillary	Furnace temperature (1900 °C, 1950 °C and 2000 °C), feed speed (2 mm/min, 4 mm/min and 8 mm/min) and draw speed (0.6 m/min – 1.2 m/min)
Fitt <i>et al.</i> , (2002)	Numerical modelling and experimental verification	Capillary (silica)	Modelling the fabrication of capillary	Furnace temperature (1900 °C, 1950 °C and 2000 °C), feed speed (2 mm/min, 4 mm/min and 8 mm/min) and draw speed (0.6 m/min – 1.2 m/min)

Table 3.3: Summary of literature review for various drawing parameters (continued).

Reference	Methodology	Type	Objective	Drawing parameters
Cheng & Jaluria (2002)	Numerical modelling	Optical fiber (silica)	Effect of draw furnace geometry for high speed drawing	Temperature profile and draw speed
Wei <i>et al.</i> , (2004)	Numerical modelling	Optical fiber (silica)	Optimization of high speed draw process with large diameter preforms	Neck down profile and temperature
Cheng & Jaluria (2004)	Numerical modelling	Optical fiber (silica)	Effect of length of furnace and furnace temperature distribution	Furnace temperature and draw speed
Cheng & Jaluria (2005)	Numerical modelling	Optical fiber (silica)	Optimization the thermal system for fiber drawing	Furnace temperature and draw speed
Xue <i>et al.</i> , (2004) and Xue <i>et al.</i> , (2006)	Numerical modelling and experimental verification	Capillary (silica and PMMA)	Effect of different materials and drawing condition	Draw speed (1 m/min) and feed speed (2.3 mm/min)
Voyce <i>et al.</i> , (2009)	Numerical modelling and experimental verification	Capillary (silica)	Modelling the self-pressurizing mechanism in capillaries	Pressure, draw speed (15 m/min), feed speed (1.5 mm/min) and furnace temperature (1460 °C – 1840 °C)
Yang & Jaluria (2009)	Numerical modelling	Capillary (silica)	Optimization of capillary drawing process	Furnace temperature, draw speed and feed speed
Yang & Jaluria (2009)	Numerical modelling	Capillary (silica)	Effect of fabrication parameters on temperature and velocity distributions and draw tension	Furnace temperature, draw speed and feed speed

Table 3.3: Summary of literature review for various drawing parameters (continued).

Reference	Methodology	Type	Objective	Drawing parameters
Mawardi <i>et al.</i> , (2010)	Numerical modelling	Optical fiber (silica)	Effect of fabrication parameters on fiber radius and draw tension	Draw speed, furnace temperature and furnace length
Luzi <i>et al.</i> , (2011)	Numerical modelling and experimental verification	Capillary (silica)	Effect of surface tension and inner pressure	Pressure (9 mbar), draw speed (0.04 m/sec), feed rate (6 mm/min) and furnace temperature (1900 °C - 2050 °C)
K. Kim <i>et al.</i> , (2012)	Numerical modelling	Optical fiber (silica)	Effect of gas flow in furnace on neck down profile and draw tension	Draw speed and furnace temperature
Chen & Birks (2013)	Numerical modelling	Capillary (silica)	Prediction of capillary holes	Pressure, feed speed and draw speed
Kostecki <i>et al.</i> , (2013)	Numerical modelling and experimental verification	Capillary (silica)	Prediction of drawing condition for microstructured fiber	Furnace temperature and pressure
S. Xue <i>et al.</i> , (2017)	Numerical modelling and experimental verification	Capillary (metamaterials – indium core with PMMA cladding)	Analysis of capillary instability	Furnace temperature (473 K and 503 K), feed speed (2 mm/min and 6 mm/min) and draw speed (0.8 m/min, 1.8 m/min and 5 m/min)
Y. K. Kim <i>et al.</i> , (2017)	Numerical modelling	Optical fiber (silica)	Drawing of large sized silica preform	Furnace temperature and draw tension

3.3 Methodology

The methodology for the fiber drawing process (including drawing of capillary and flat fiber) has been described in detail in Chapter 2, 2.3 (Fabrication of Capillary) and 2.4 (Fabrication of Flat Fiber). The general flowchart for each of the fabrication methodology is shown in Figures 3.1 and 3.2.

For the fabrication of capillary, firstly the preform is placed on the preform chuck. Then, the furnace temperature is set and fiber drop down occurs. Fiber drop down is defined when the fiber drops from the furnace due to gravitational force and draw tension after a suitable softening temperature has been reached. Depending on the mass per unit length of the preform and the draw speed, the time for the preform drop to exit the furnace's bottom iris may vary. Higher mass per unit length indicates more time is needed to heat the preform to its softening temperature and higher draw speed indicates faster time for the fiber to exit from the furnace.

If the capillary or flat fiber breaks in the middle of the experimental run at any stage of the process, the whole fabrication process has to be repeated again and a new drop down for the fiber needs to be obtained. If the capillary does not break, the desired feed speed and draw speed will be set. Diameter of the capillary will be measured. If the desired diameter has been obtained, capillaries will be cut and collected. If not, the draw speed and feed speed will be adjusted accordingly. In flat fiber fabrication, once the capillary dimension is achieved, vacuum pressure is applied to flatten the flat fiber. If the desired dimension is not achieved, the vacuum will be adjusted accordingly. Once the dimensions are obtained, the flat fibers will be cut and collected. In the fabrication of an optical fiber, a solid preform is fed into a furnace at the preform's melting temperature and drawn to a fiber which has a much smaller diameter.

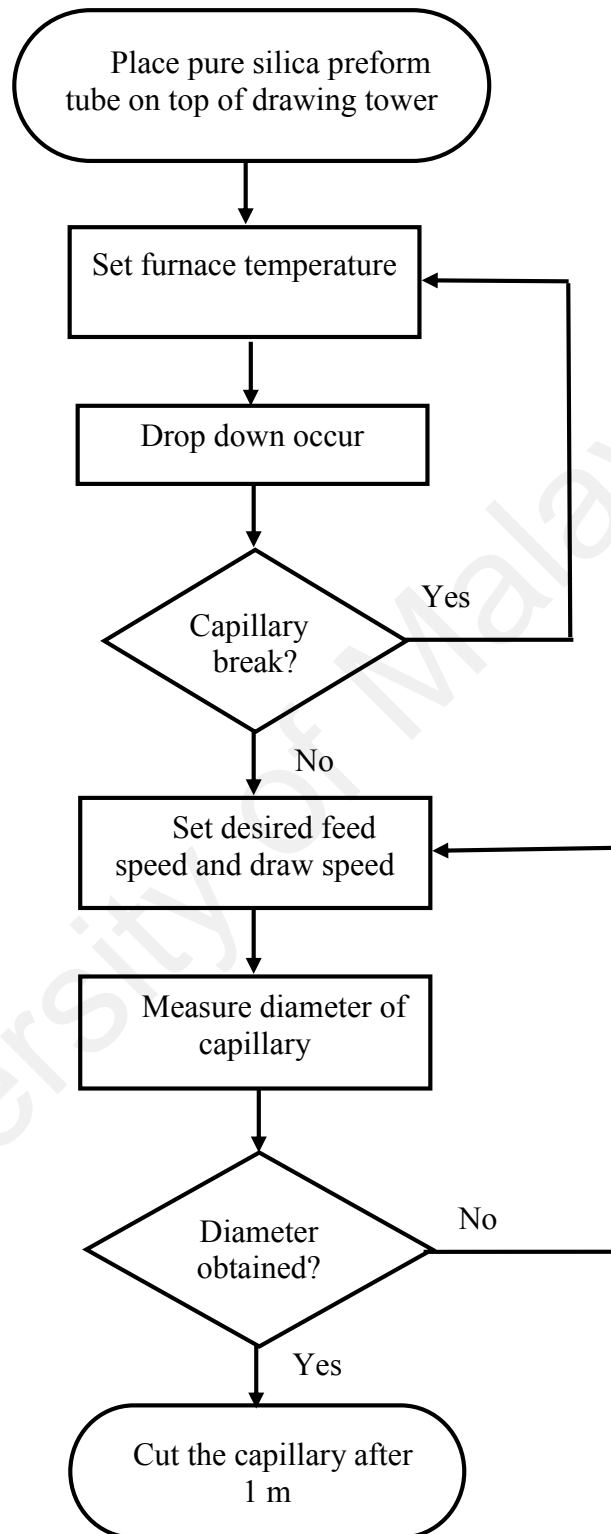


Figure 3.1: General flowchart for the fabrication of pure silica capillary.

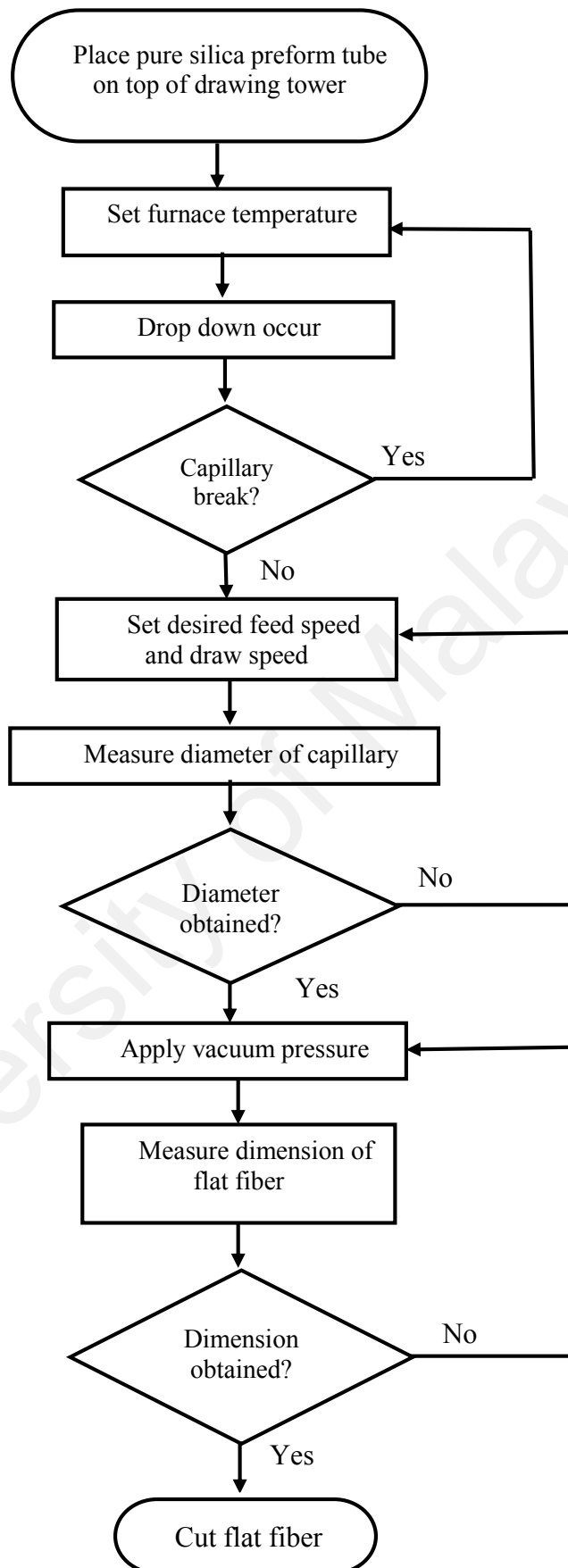


Figure 3.2: General flowchart for the fabrication of pure silica flat fiber.

The drawing of the solid preform fulfills the mass conservation law, where the volume reduction ratio, η is defined as Equation 3.8 (Paek & Runk, 1978).

$$\eta \equiv \frac{OD_{fiber}^2}{OD_{preform}^2} = \frac{U_f}{U_d} \quad (3.8)$$

where OD_{fiber} is the outer diameter of the drawn fiber, $OD_{preform}$ is the outer diameter of the preform, U_f is the preform feed rate and U_d is the draw speed. In all the drawing fabrication experiments in this thesis (unless otherwise stated), Equation 3.8 is used to determine the draw speed and feed speed of the drawing process based on the desired diameter of the drawn fiber and the known preform outer diameter.

The objective of the experiments in this chapter is to characterize the fabrication parameters that affect flat fiber drawing process and to identify feasible drawing conditions. The effects of the fabrication parameters are observed by measuring the outer and inner diameters of the fabricated capillary and the dimension and shape of the flat fiber. A summary of the experimental work done in this chapter to study the fabrication parameters and its measurements are shown in Table 3.4. Measurements are done to observe the changes in the capillary's physical properties such as diameter, flat fiber dimension and shape in different drawing conditions.

Table 3.4: Summary of experimental work done in Chapter 3.

Drawing parameter	Controlled variable	Manipulated variable	Measurements	
			Capillary	Flat fiber
Furnace temperature	Feed speed and draw speed	Furnace temperature	Outer and inner diameter	Width, thickness and shape
Preform wall thickness	Draw speed and feed speed	Furnace temperature	Outer and inner diameter	Thickness and shape
Draw speed and feed speed	Furnace temperature and feed speed	Draw speed and feed speed	Outer and inner diameter	Shape

Table 3.4: Summary of experimental work done in Chapter 3 (continued).

Drawing parameter	Controlled variable	Manipulated variable	Measurements	
			Capillary	Flat fiber
Vacuum pressure	Feed speed, draw speed and furnace temperature	Vacuum pressure	-	Width, thickness and shape

3.4 Results and Discussion

3.4.1 Furnace temperature

The experimental work to observe the effect of furnace temperature on the outer diameter of a thick preform started by drawing a capillary from a Suprasil F300 (fused silica) thick preform tube (25/19 mm). The detailed experimental procedure has been described in Chapter 2, Sections 2.2 and shown in a flow diagram in Figure 3.1.

The furnace temperature was varied from 1990 °C to 2200 °C and the change in the capillary outer diameter were measured using the drawing tower diameter gauge. The temperature range from 1990 °C to 2200 °C was chosen as its viscosity range was suitable for a fused silica preform as seen in Figure 2.5 in Chapter 2. The objective of this experiment was to vary the furnace temperature to see which temperature gives an outer diameter of 1 mm at a fixed draw speed and feed speed.

The draw speed was fixed at 1 m/min to get the initial capillary with an outer diameter of 1 mm and the feed speed was maintained at 2 mm/min. The average measurements (with error bars) were shown in Figure 3.3.

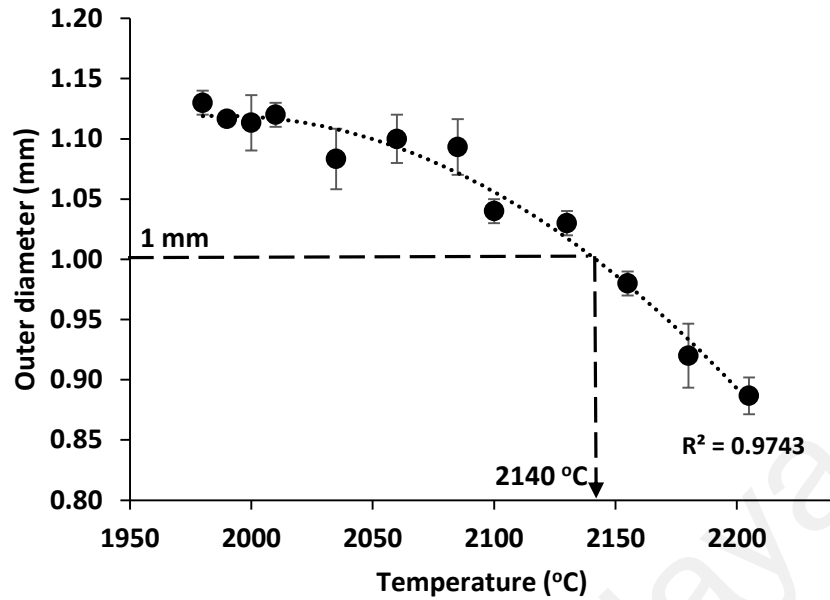


Figure 3.3: Effect of furnace temperature on capillary outer diameter.

The draw speed and feed speed were set as per Equation 3.8 to give a capillary outer diameter of 1 mm for the given preform outer diameter. The trend obtained was as predicted (refer Section 3.2 for further details) where a higher temperature results in a smaller outer diameter (Fitt *et al.*, 2001 and Mawardi & Pitchumani, 2010). Fitting the graph with a polynomial trend line (order 2) gave an R^2 value of 0.9743.

Based on the trend line, the outer diameter was approximately 1 mm at 2140 °C as highlighted in Figure 3.3. To get 1 mm with a 5% error, the range of furnace temperature was approximately between 2110 °C to 2170 °C. Initially, there was only a small variation in the outer diameter when the furnace temperature was increased at steps of 10 °C. This could be due to stabilization of the outer diameter at the lower temperature due to the rapid increase of viscosity (Fitt *et al.*, 2001). After 2010 °C, the temperature was increased at steps of 25 °C and there was a larger variation in the decrease of the outer diameter.

The reduced outer diameter was due to the softening of the preform and the draw tension acting on the fiber during the neck down region (Xue *et al.*, 2006). Further details on the neck down region can be referred in Section 2.2.3, Chapter 2. As shown in Equation

2.1, the draw tension is directly proportional to the temperature dependent viscosity. As the temperature increases, the viscosity and draw tension reduces. As viscosity reduces and combined with a low draw tension, glass reached its softening temperature in a shorter time, becoming more easily pulled from the furnace and results in a smaller outer diameter.

From this observation, the recommended furnace temperature during capillary drawing for a pure silica preform tube with a thickness of 3 mm and to obtain capillary with outer diameter of 1 mm is approximately between 2110 °C to 2170 °C, which is for a viscosity range of $10^{3.77}$ Pa.s to $10^{4.05}$ Pa.s. Thus, changing the furnace temperature could further reduce the outer diameter of the fiber despite having the draw speed and feed speed fixed to get an outer diameter of 1 mm.

This conclude that furnace temperature plays an important role in controlling the outer diameter of a capillary and the final flat fiber dimension. In the next section, the effect of furnace temperature on the preform wall thickness will be investigated.

3.4.2 Preform wall thickness

For flat fiber fabrication, a preform tube is used instead of a solid preform. The volume reduction ratio shown in Equation 3.8 is still used as a guideline to determine the draw speed and feed speed for a specific fiber diameter, but there is now additional force inside the tube acting on the preform wall thickness during the drawing process. Thus, the preform wall thickness play a role in determining the final size of the flat fiber as the effects of surface tension may differ depending on the wall thickness. The effects of surface tension may be more significant on thinner wall thickness due to its lower volume. There is also a different surface temperature on the outer diameter and inner diameter, which may cause different time for glass softening. In a thinner preform, the temperature

difference between the outer and inner diameter is smaller due to smaller thickness, causing the preform to be deformed more rapidly.

In this section, two silica preform tubes (F300) with different wall thickness were used to observe the effect of preform wall thickness. The preform inner/outer diameters were 18/20 mm and 19/25 mm respectively, which gives a preform tube wall thickness of 1 mm (thin preform) and 3 mm (thick preform). In order to study the effect of preform wall thickness, the temperature was varied from 1980 °C to 2205 °C and the change in the capillary outer and inner diameter were measured. The draw speed was fixed at 1 m/min for both preform types to get the initial capillary with an outer diameter of 1 mm.

Using SEM imaging, the cross section of the fabricated capillary using thick and thin preforms was shown in Figure 3.4 (a) and (b). The diameter measurements were taken using optical microscope and SEM imaging.

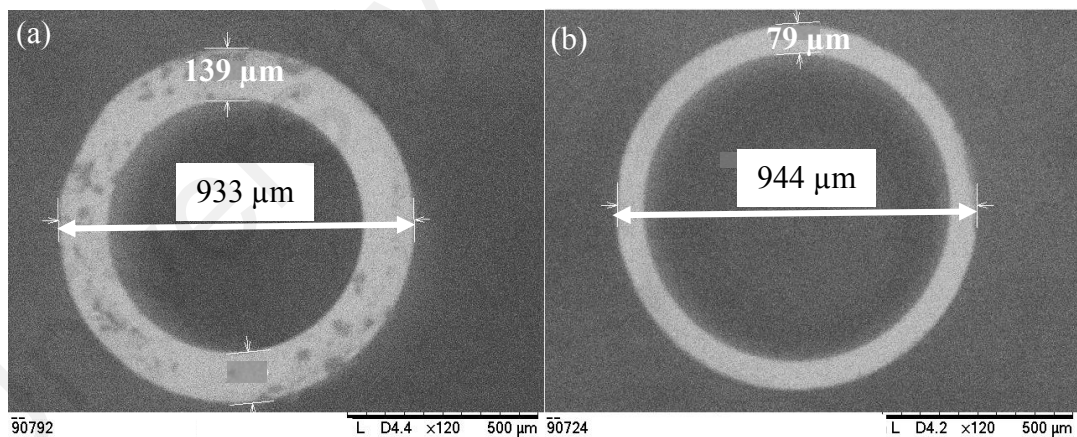


Figure 3.4: SEM image of the fabricated capillary cross section for (a) thick preform and (b) thin preform.

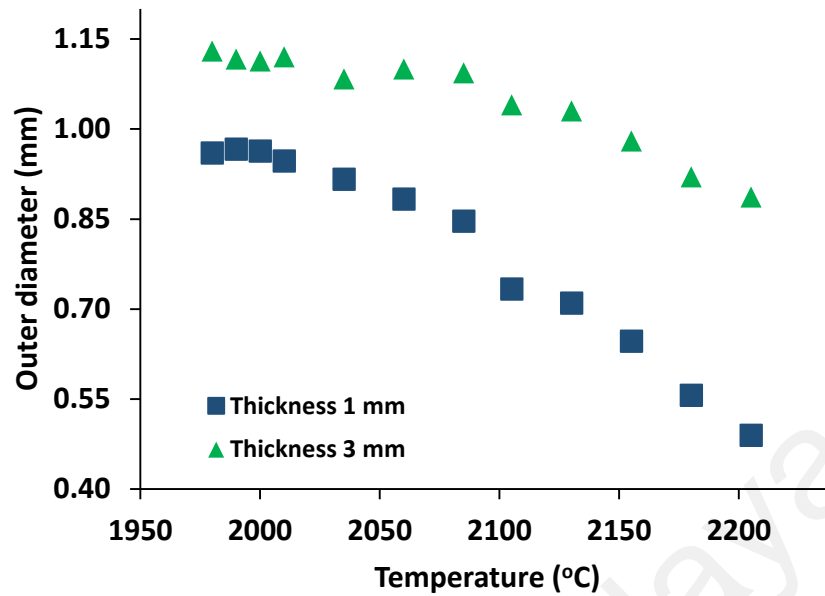


Figure 3.5: Effect of temperature on preform with different wall thickness.

Figure 3.5 shows the effect of temperature on the outer diameter of silica capillaries fabricated from thin and thick preform. Since the same material (F300) was used, there was a similar trend on the outer diameter obtained for increasing temperature. As the temperature increased, the thin preform became more sensitive to deviations in the furnace temperature as the outer diameter decreased more rapidly for the thin preform compared to the thick preform. From the minimum temperature of 1980 °C to the maximum temperature of 2205 °C, the range in the outer diameter of the thick preform was 0.24 mm. For the thin preform, the range was almost double the change for thick preform at 0.47 mm. An increase of 2 mm in the preform thickness resulted in an outer diameter that was twice as sensitive to the effect of furnace temperature. For a thin preform, after the temperature of 2010 °C, a change of 10 °C can reduce the outer diameter of the capillary by 0.05 mm.

In the thin preform, the temperature difference between the surface temperature (for the outer diameter) and the inner temperature (for the inner diameter) was smaller, so the surface temperature of the inner part of the preform had a higher temperature compared

to the thick preform. This caused a longer neck down region but at the risk of having a deformed flat fiber due to excessive surface tension on the fiber. As the inner diameter temperature increased, the viscosity and draw tension reduced, causing the inner diameter to become smaller rapidly. The viscosity for the thin preform increased more rapidly. A high viscosity may cause crystallization and viscoelastic effects (Shelby, 2005). However, viscoelastic effects can be negligible as it is less important than surface tension effects (Xue *et al.*, 2006).

The results show that preform wall thickness or volume of the preform play a role in the determination of the fiber outer diameter. It was easier to control the outer diameter for a thick preform since it was less sensitive to deviations in the furnace temperature. The thin preform has a larger airhole, which may be heated at a faster rate compared to thick preform due to the reduced amount of material present (Xue *et al.*, 2007). For better control of the capillary dimension, a thick preform was recommended. Thus, it can be concluded that in addition to furnace temperature, preform wall thickness also influenced the thickness of the capillary and the final flat fiber dimension.

Figure 3.6 shows the effect of temperature on the inner diameter of a thin preform capillary. For the thin preform, the range of the inner diameter was 0.67 mm which was larger than the outer diameter at 0.47 mm, indicating the inner diameter was more affected by the effect of temperature (Voyce *et al.*, 2004). The graph can be fitted with a polynomial trend line (order 2) with a R^2 value of 0.9957. The inner diameter was said to completely collapse at 0 mm and based on the trend line, this was expected to occur at 2230 °C, which was no longer a suitable temperature for a fused silica preform.

At 2230 °C, the outer diameter for the thin preform was predicted to be approximately 0.4 mm. The inner diameter of a capillary was affected by the draw tension and surface tension (Xue *et al.*, 2006). In this case, there was no pressurization of the hole, so the

inner diameter did not completely collapse even as the temperature was increased to 2200 °C. According to Fitt *et al.*, 2002, experimental results show that with internal hole pressurization of 0.1 psi (0.69 kPa), the capillary hole collapsed at a temperature of 2225 °C, which was almost similar to this finding.

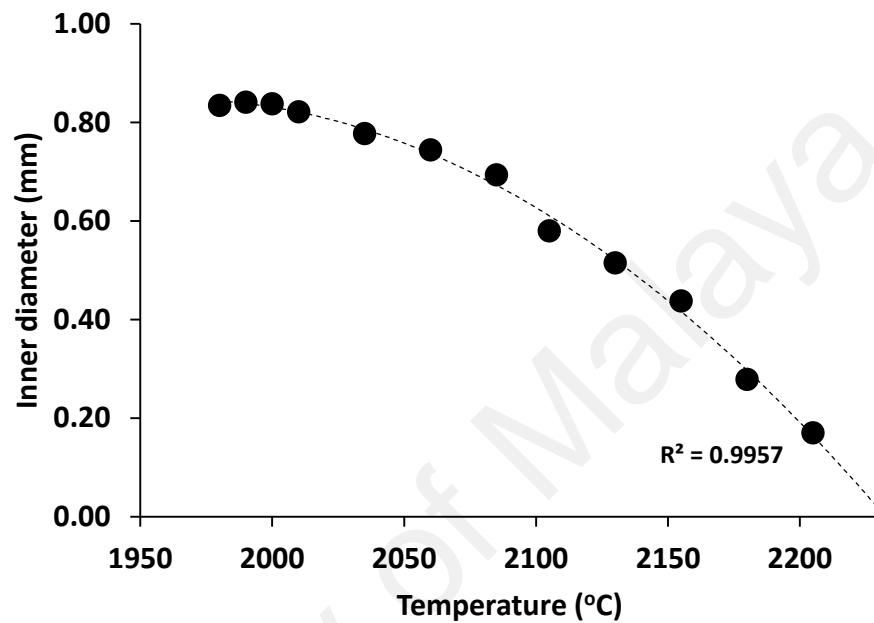


Figure 3.6: Effect of temperature on the inner diameter of a capillary (thin preform).

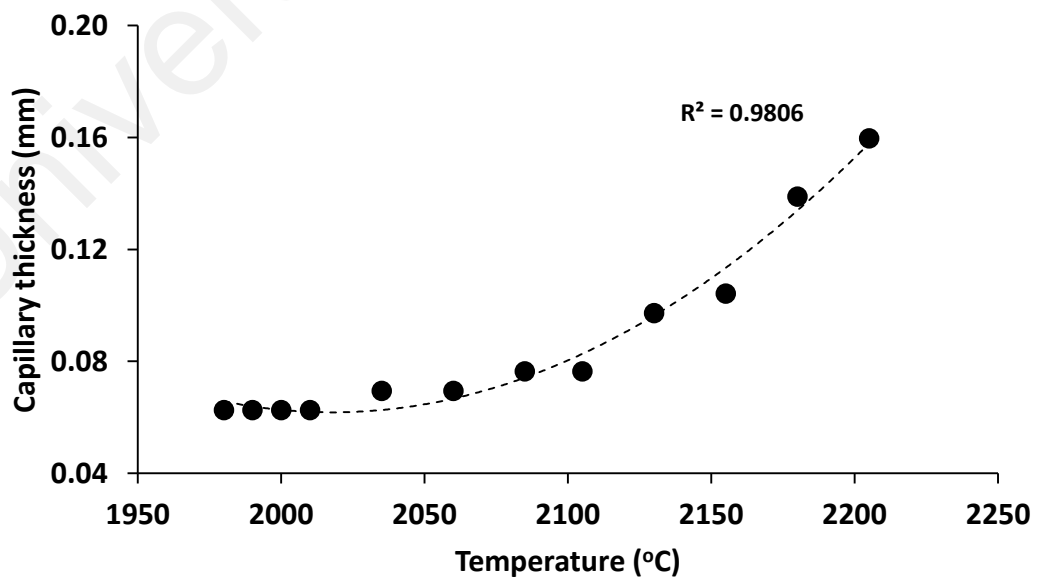


Figure 3.7: Effect of temperature on the capillary thickness (thin preform).

The variation of the thin preform capillary thickness (measured from the SEM images) as the temperature was increased was shown in Figure 3.7. As the temperature increased to above 2000 °C, the capillary thickness started to increase exponentially. This observation can be attributed to mass conservation law where the fiber draw was essentially a material redistribution process (Xue *et al.*, 2005). According to Xue *et al.*, 2005, as the preform starts extending, the net cross sectional area has to decrease inversely with the increasing velocity. This caused the external fiber radius to shrink to form the neck down region and the inner hole to enlarge.

Figure 3.8 shows the ratio OD/ID for the thin preform which can be fitted with a polynomial trend line (order 4) with a R^2 value of 0.9911. The preform OD/ID was calculated as 1.11. The ratio OD/ID increases exponentially as the temperature increases above 2010 °C and it is higher than the preform OD/ID which indicates that more hole collapse occurred at higher temperature (Xue *et al.*, 2006). If the OD/ID ratio was smaller than the preform OD/ID, hole enlargement may occur (Xue *et al.*, 2006).

Using Equation 2.3, the empirical constant, k for the drawing of the capillary using a thin preform was obtained as shown in Figure 3.9. The values for the viscosity, μ were calculated from Equation 2.2, the drawing tension, γ is assumed to be 0.3 N/m, the heating zone length, L is 3.4 cm, the preform area A is $\pi[(\frac{OD}{2})^2 - (\frac{ID}{2})^2]$ and draw speed, U_d is 0.0167 in m/s. The empirical constant, k can be used to predict the preform area, outer diameter and/or inner diameter of a fabricated capillary given the furnace temperature and draw speed. The results obtained in this section were consistent with the mass conservation theory stated in Equation 3.8. In the next section, the effect of draw speed and feed speed are investigated.

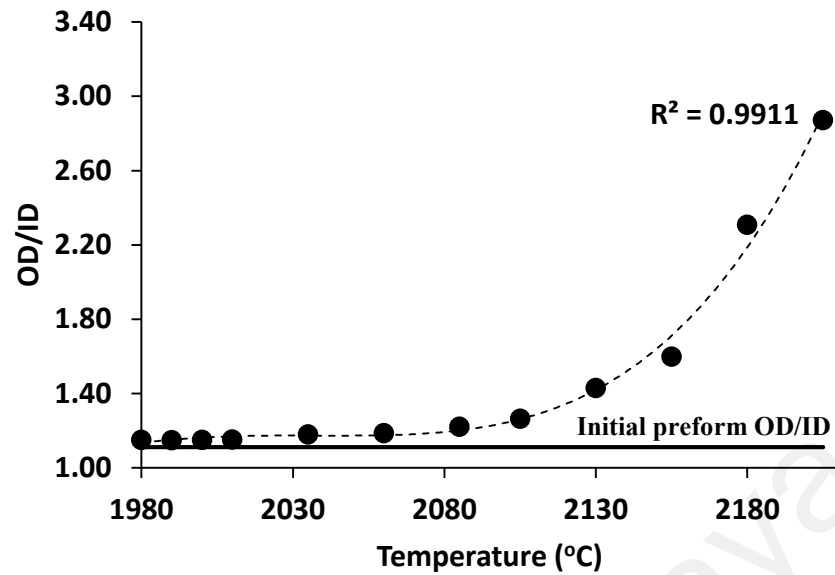


Figure 3.8: Ratio OD/ID for thin capillary. The preform OD/ID was represented by the straight line.

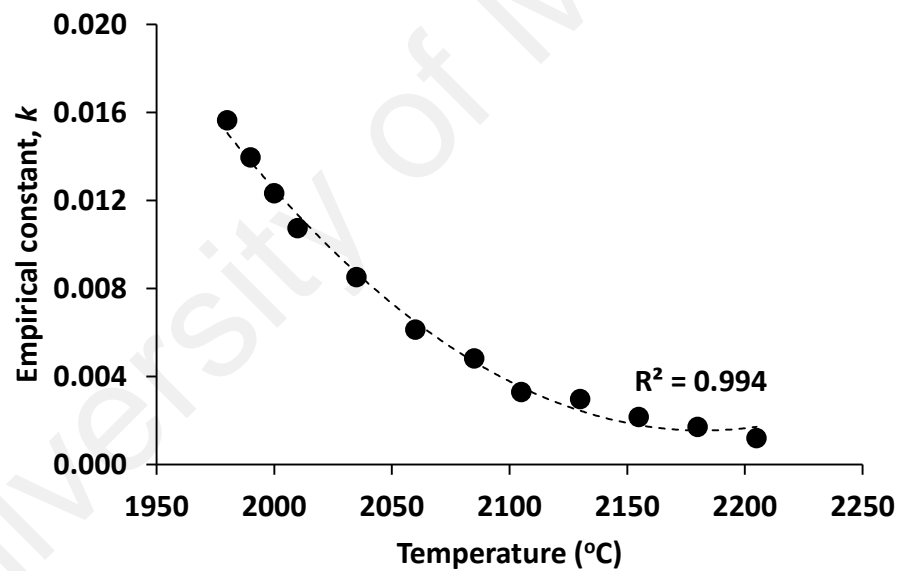


Figure 3.9: Empirical constant, k .

3.4.3 Draw speed and feed speed

Most commercially available optical fibers are fabricated using high speed drawing for mass production. However, increasing draw speed causes a delay in the necking process because the preform takes a larger distance to get heated to the softening temperature (Yin & Jaluria, 2000). Draw speed is linearly proportional to draw tension (Paek, 1999). The draw tension and the force due to gravity represents the pulling force

exerted at the fiber specifically at the neck-down region when the diameter deformation occurs due to lower glass viscosity (Choudhury & Jaluria, 1998a). Different draw speed also gives different temperature distributions, causing different neck down shape (Paek & Runk, 1978). A low draw speed (which cause low draw tension due to low value of viscosity) in combination with a high temperature may result in fiber break because of the mobile state of glass and capillary instability (Cheng & Jaluria, 2004).

For the experimental work to observe the effect of draw speed, the furnace temperature was fixed at 2100 °C and the draw speed was increased from 1 m/min to 2 m/min (at steps of 0.2 m/min) for a fixed feed speed at 2 mm/min to get an initial outer diameter of 1 mm. According to Yin & Jaluria, 2000, when furnace temperature increases, the allowed fiber draw speed also increases so in this analysis, the furnace temperature was fixed. The change in the fabricated capillary outer diameter was then measured.

Figure 3.10 shows the effect of draw speed on the outer diameter of the fabricated capillaries (thin and thick preform). As the draw speed increased, the outer diameter decreased, which was as expected based on literature (Choudhury & Jaluria, 1998a, Fitt *et al.*, 2001 and Mawardi & Pitchumani, 2010). When the draw speed increased, the surface temperature of the preform decreased and goes below the softening point, which caused the viscosity to increase (Choudhury & Jaluria, 1998a). This in turn increased the surface tension and neckdown rate (Mawardi & Pitchumani, 2010) and decreased the outer diameter. In addition, when the draw speed was increased, the melted preform will spend less time inside the furnace (Boll & Nummela, 2010) and thus have lower surface temperature. At draw speeds of 1 m/min and 1.2 m/min, there was a difference between the outer diameter for both preform thickness and this could be due to the stabilization region of the preform at thickness of 3 mm. Further details on the stabilization region will be discussed in the next chapter. The outer diameter was nearly the same after 1.2 m/min

for both preform types, which indicate the effects of the draw speed on the outer diameter was the same despite different preform wall thickness.

Next, the experiment was performed for a higher feed speed of 6.48 mm/min on a thick preform (25/19 mm). In Figure 3.11, the average outer diameter (mm) was obtained for a draw speed varied from 1.2 m/min to 2.6 m/min at a feed speed of 6.48 mm/min. The furnace temperature was 2100 °C. The average diameter was obtained since the diameter gauge of the drawing tower measured both the x and y dimension of the fiber. The theoretical prediction (Fitt *et al.*, 2001) from Equation 3.3 was represented by the solid line in Figure 3.11. A few assumptions were made for the theoretical prediction which were $\beta = \log\left(\frac{U_d}{U_f}\right)$ and $e^{-\frac{\beta}{2}} = \sqrt{\frac{U_f}{U_d}}$. The value for the fitting parameter $\frac{\gamma}{\mu}$ was 1.4×10^{-6} m/s at 2100 °C. The surface tension of the fiber was 0.52 N/m.

In conclusion, as expected from the literature review, an increase in the draw speed will reduce the outer diameter of the capillary. In addition, at the same draw speed with two different feed speeds, the higher feed speed resulted in a larger outer diameter. The outer diameter was more sensitive to the effect of draw speed at a higher feed speed. A higher feed speed was also proportional to a high draw speed. The draw speed and feed speed using different preform wall thickness had nearly similar effect on the outer diameter capillary and the final flat fiber dimension.

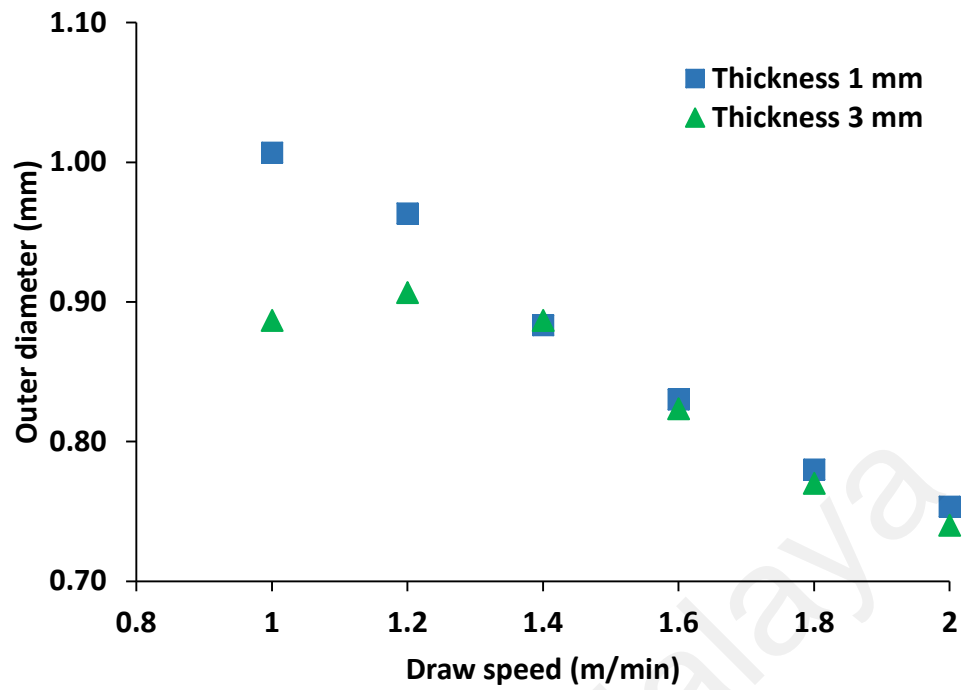


Figure 3.10: Effect of draw speed on the outer diameter of a capillary (thin and thick preform) at a feed rate of 2 mm/min.

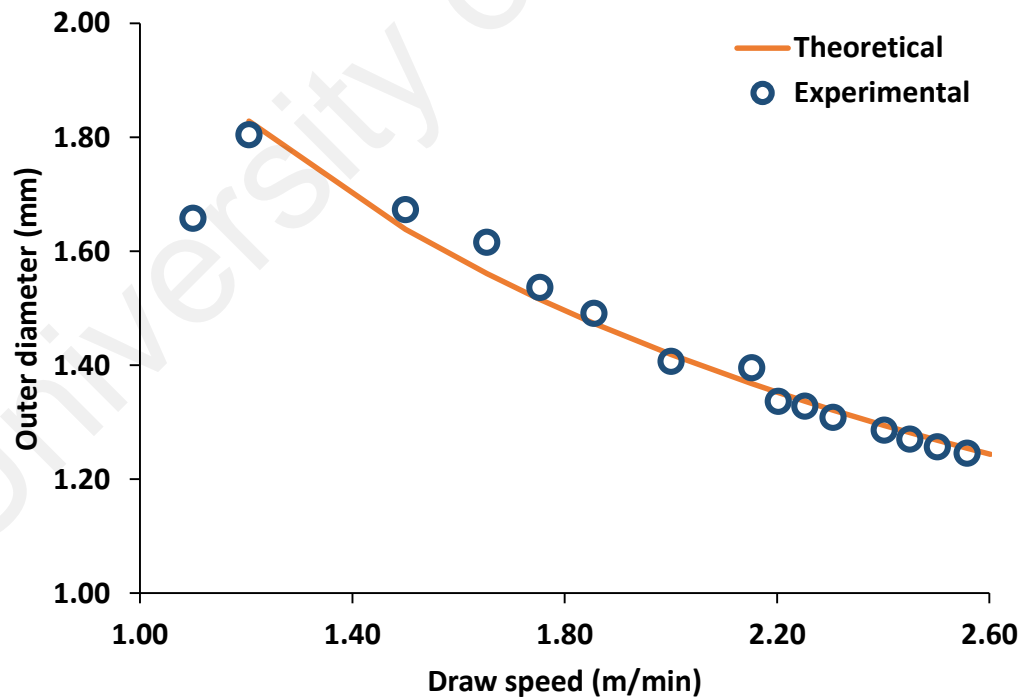


Figure 3.11: Outer diameter (mm) versus draw speed (m/min) at a feed rate of 6.48 (mm/min).

3.4.4 Vacuum pressure

Once the capillary is drawn, pumping out the air inside the capillary using a vacuum pump creates a reduced pressure inside the inner capillary, thus allowing it to be collapsed and flattened into a flat fiber. The internal hole pressurization, where there is pressure difference between the air inside and outside the capillary, allow us to control the degree of capillary hole closure and preventing capillary collapse (Fitt *et al.*, 2002). Other findings from Fitt *et al.*, 2002 related to capillary control during fabrication are:

1. When capillaries are drawn, surface tension can cause geometry changes and even hole collapse. Surface tension destabilizes a solid fiber but it is not clear if the same conclusion can be said for a capillary.
2. The degree of collapse can be predicted using the ratio of the surface tension to the viscosity.
3. Hole collapse is more sensitive to feed speed than draw speed.
4. Hole closure is sensitive to temperature. At a temperature of 2225 °C, the hole of a control capillary (no pressure applied) is completely closed due to surface tension but at 1975 °C, the hole has not closed although it does experienced collapse. For the capillary with pressure applied, it was observed that at 0.25 psi (~1.72 kPa) for 1975 °C, the hole did not collapse. However, at 2225 °C, the hole is deformed significantly due to surface tension. At a large pressure of 0.5 psi (3.45 kPa) at 1975 °C, the capillary became inflated and at 2225 °C with a pressure of 0.8 psi (5.5 kPa), the capillary has ‘exploded’.
5. For hole closure, the effects of hole pressurization and surface tension are included. A key parameter, S (Equation 3.9) for determining the practicability of pressurized fiber drawing was developed, where if $S \gg 1$, hole pressurization is not worth considering.

$$S = \frac{L\gamma}{\mu h_{10} U_f \log\left(\frac{U_d}{U_f}\right)} \quad (3.9)$$

According to Voyce *et al.*, 2009, the feedback mechanism to prevent hole closure can be described below:

1. As the preform is lowered into the furnace, the temperature for the air inside the preform increases, creating overpressure and increased fiber radius. However, the temperature soon decreases after reaching its maximum value (based on its temperature profile), reducing both the pressure and fiber radius.
2. By sealing the top of the preform, the volume of air inside the furnace remain constant and the volume of glass reduces due to reduction in length of the preform. At the end of the furnace, overpressure increases until it overcame the effects of surface tension. Hole will reopen.
3. If the surface tension were to completely close the hole, only glass would come out from the furnace and no airhole.

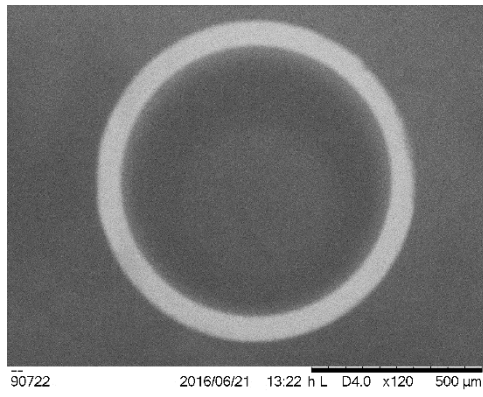
For capillary fabrication, when vacuum pressure is applied at the top of the capillary, air is completely removed. Thus, the hole will close due to surface tension effects (Fitt *et al.*, 2002 & Voyce *et al.*, 2009). Hole collapse for silica can be reduced by increasing the draw down ratio which leads to a steeper neck down region and increased capillary number (Xue *et al.*, 2006). Decreasing the aspect ratio also has the same effect as increasing the draw down ratio (Xue *et al.*, 2006).

The experimental work to observe the effect of vacuum pressure started with the fabrication of capillaries using thin (18/20 mm) and thick (19/25 mm) preforms. Once the capillary drawing process had stabilized, vacuum pressure was applied to the top of the preform. The vacuum pressure was varied from 0 kPa to 20 kPa (~2.9 psi) for the thin preform. For the thick preform, the vacuum pressure was varied from 1 kPa (~0.14 psi)

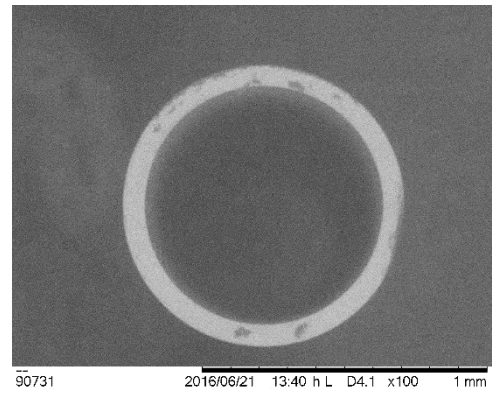
to 59 kPa (~ 8.56 psi). The furnace temperature was 2100 °C. The draw speed was fixed at 1 m/min to get the initial capillary with an outer diameter of 1 mm and the feed speed was maintained at 2 mm/min. The draw down ratio (ratio of draw speed to feed speed) was calculated as 500. The aspect ratio was 0.29 (thin preform) and 0.37 (thick preform). The capillary number, C_a was calculated as 2474 at 2100 °C and a surface tension of 0.3 N/m.

Figures 3.12 and 3.13 show the change in the capillaries fabricated from the thin and thick preform as the vacuum pressure was gradually increased at 2100 °C. The thickness of the preform wall thickness determines the rate at which the flat fiber was formed when vacuum pressure was applied. The first flat fiber thickness (starts to become flat fiber from capillary) was twice the capillary thickness for both thin and thick preform obeying the mass conservation law and as predicted from Equation 2.14. Once the flat shape was obtained, increasing the vacuum will cause excessive capillary collapse and this happened more rapidly in the thin preform. For the thin preform in Figure 3.12, a deformed ‘H’ shape was obtained at the vacuum of 2 kPa. As the vacuum increased, it can be seen that a force pulls towards the center of the fiber until a deformed ‘X’ shape was observed at 2.5 kPa to 40 kPa.

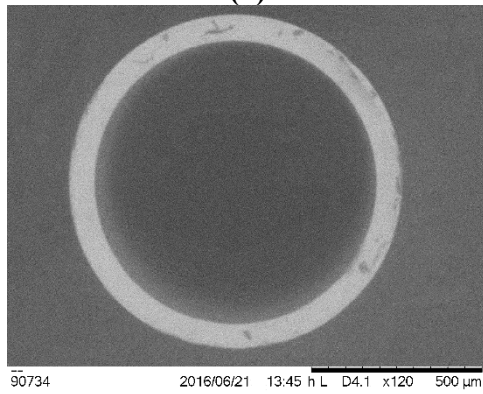
The deformations occurred in the neck down region due to surface tension effects (Fitt *et al.*, 2002, Xue *et al.*, 2006 & Voyce *et al.*, 2009). Without applied vacuum pressure, surface tension effects can be ignored when the capillary number exceeds 200 (Xue *et al.*, 2006). However, with applied vacuum pressure, the feedback mechanism described in Voyce *et al.*, 2009 in the earlier part of this section, does not occur. This because there was no longer any air inside the preform in the furnace region and there was no increased temperature inside preform, which indicate no overpressure occurring (Voyce *et al.*, 2009).



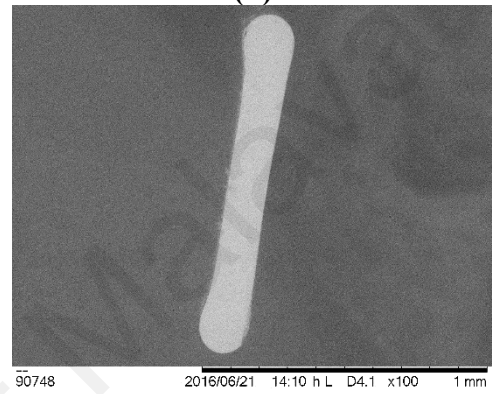
(a)



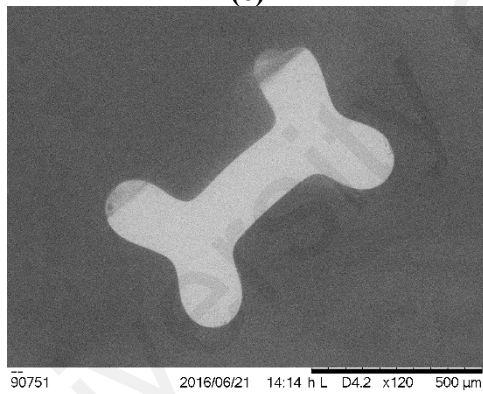
(b)



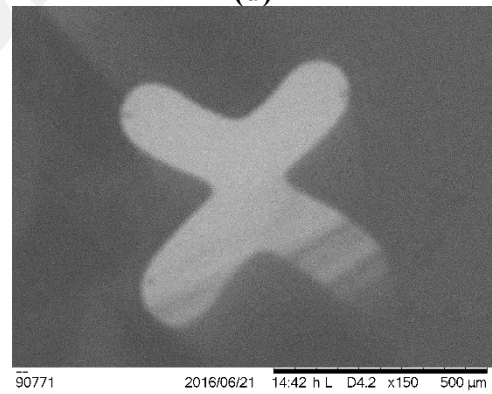
(c)



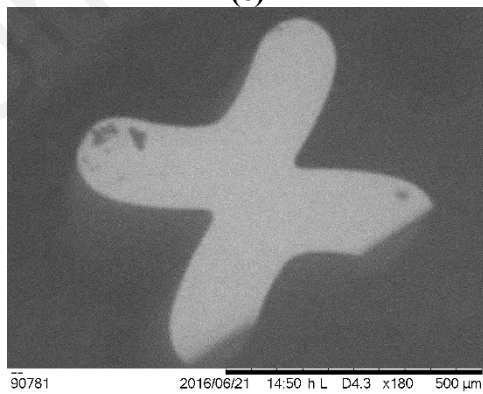
(d)



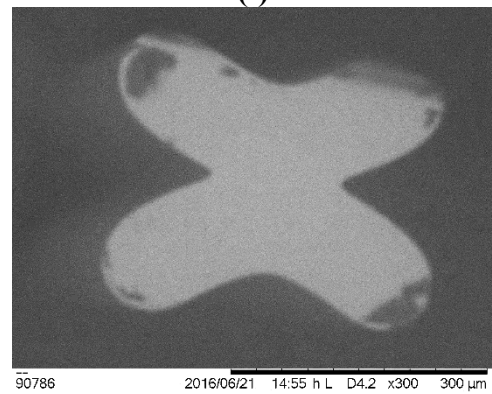
(e)



(f)

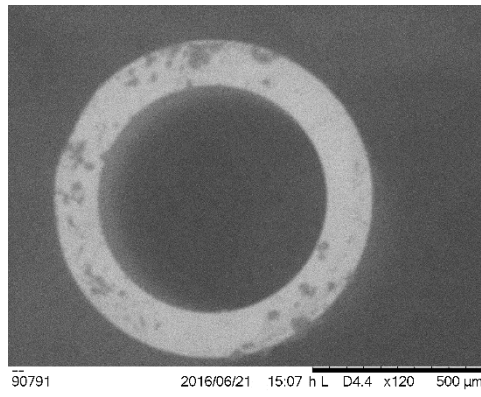


(g)

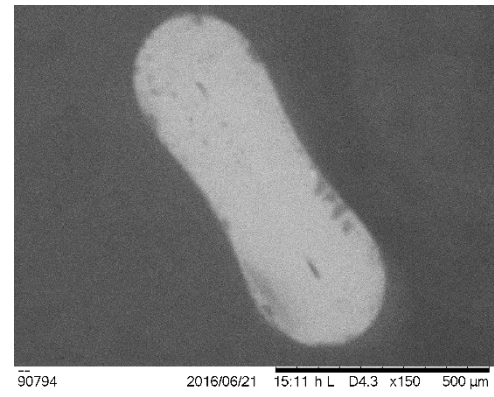


(h)

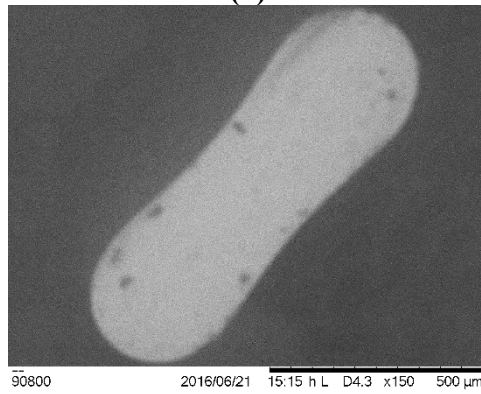
Figure 3.12: Effect of vacuum pressure on a thin preform at (a) 0.0 kPa, (b) 0.5 kPa, (c) 1.0 kPa, (d) 1.5 kPa, (e) 2.0 kPa, (f) 2.5, 5.0 and 10.0 kPa, (g) 20.0 kPa and (h) 40.0 kPa.



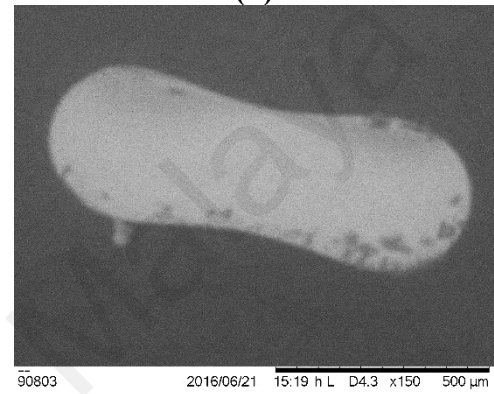
(a)



(b)



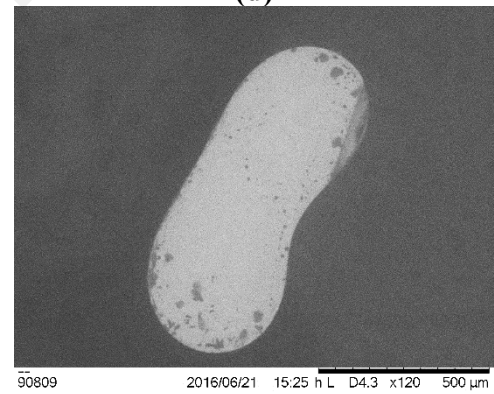
(c)



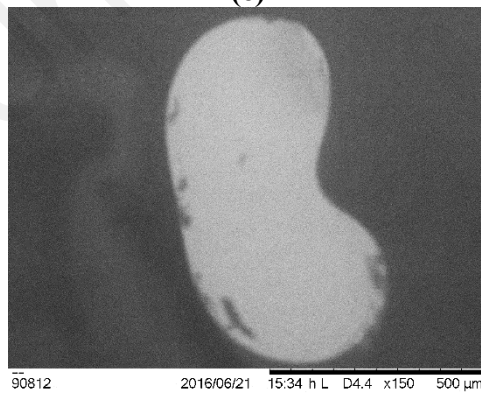
(d)



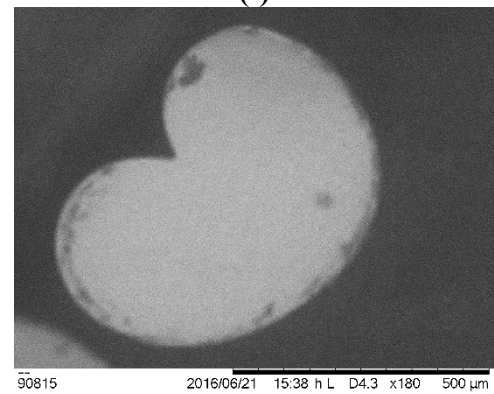
(e)



(f)



(g)



(h)

Figure 3.13: Effect of vacuum pressure on a thick preform at (a) 1.0 kPa, (b) 2.0 kPa, (c) 4.0 kPa, (d) 6.0 kPa, (e) 10.0 kPa, (f) 20.0 kPa, (g) 40.0 kPa and (h) 59.0 kPa.

For the thick preform in Figure 3.13, there was still a flat shape even at 20 kPa, indicating that the vacuum pressure had less effect on the capillary collapsing process when it had a thick wall thickness. For thick preform, there was a larger volume of glass exiting from the furnace and the thicker flat fiber was less affected by the effect of surface tension. At higher vacuum pressure, it can also be seen that a force pulled towards the center of the fiber until the fiber resembled a deformed ‘heart’ shape in the center. This force was due to the vacuum pulling upwards, which caused the fiber to flatten.

In this section, both thin and thick preforms were investigated and it was found that despite similar drawing parameters, there was a change in the fiber shape fabricated. The difference in their volume had an effect on the final fabricated fiber shape. For both the thin and thick preform, the surface tension applied on it is the same but it becomes higher as the volume of the preform decreased. In addition, vacuum pressure applied may also increase the surface tension.

Thus, vacuum pressure affects flat fiber with a different preform wall thickness differently due to the different volume of the preform. In a thin preform, the hole where vacuum was applied was larger and the glass volume was smaller, so the influence of surface tension was more significant compared to a thick preform which has a smaller hole and larger glass volume. A thick preform with more volume was less sensitive to deviations in the vacuum pressure due to lower surface tension effects and thus it would be easier to control the size of its fabricated flat fiber.

To gain an understanding of the effect of vacuum pressure on the flat fiber geometry, the ‘flatness’ of the flat fiber can be quantified using eccentricity. Mathematically, the flat fiber eccentricity is defined as $\sqrt{1 - \left(\frac{t}{w}\right)^2}$ where t and w are the thickness and width of the flat fiber. For a flat fiber, a condition of $t \neq w$ applied because when $t = w$ or

eccentricity = 0, a circular shape is obtained. A higher eccentricity indicates a more flattened fiber.

Next, the experimental work to observe the effect of vacuum pressure continued with the thick preform. This was because it was observed in Figure 3.12 that the flat fiber fabricated from the thin preform was already deformed even at low vacuum. Since the thin preform has a smaller volume, even a small reduced pressure, can deform the fiber. The temperature was fixed to 1980 °C and 2105 °C. The vacuum was varied from 0 kPa to 6 kPa. Higher vacuum will cause the flat fiber to become more deformed so the results may not be reliable. The draw speed was fixed at 1 m/min to get the initial capillary with an outer diameter of 1 mm and the feed speed was maintained at 2 mm/min. The change in the width and thickness of the flat fiber were observed as the vacuum increased. Figure 3.14 shows eccentricity versus vacuum (kPa) for a thick preform at 1980 °C and 2105 °C.

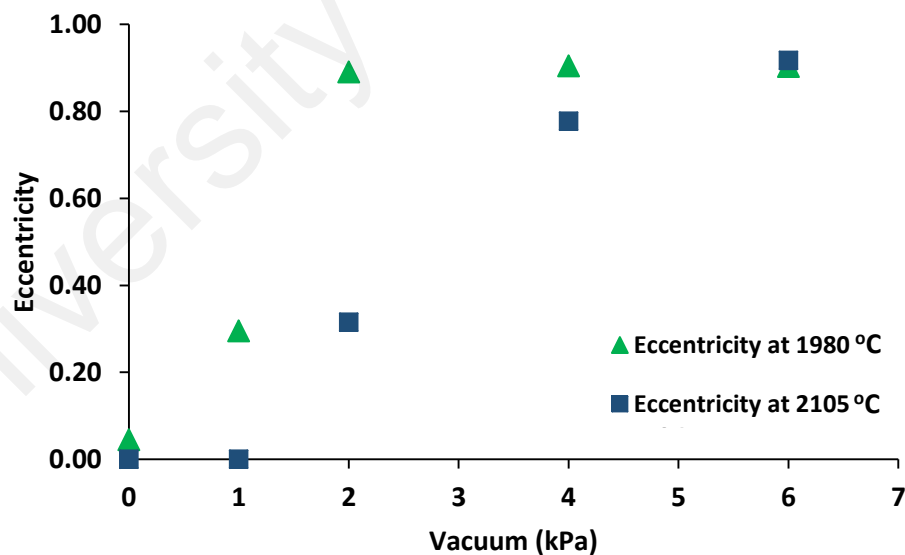


Figure 3.14: Eccentricity versus vacuum (kPa) for thick preform.

It can be seen in Figure 3.14 that the eccentricity initially increases rapidly at low vacuum pressure at 1980 °C and reaches its stagnant value faster at 2 kPa. At a higher temperature of 2105 °C, there was a gradual increase in the eccentricity of the flat fiber

and a stagnant value was reached after approximately 5 kPa. Eccentricity reached a stagnant value because the neck down part of the fiber had already collapsed and was no longer being affected by the vacuum pressure. Fiber geometry was shown to be sensitive to the temperature profile of the glass (Voyce *et al.*, 2009). Flat fiber eccentricity was more sensitive to lower temperature because the fiber drawing stabilized more quickly at lower temperatures due to the rapid increase of viscosity with reduced temperature (Fitt *et al.*, 2001). Due to that, the effect of surface tension becomes significant faster at lower temperature.

From Figure 3.14, it can be seen that a vacuum pressure of 2 – 4 kPa was sufficient to get a flat shape at a temperature of 2105 °C for a thick preform. To have better control of the fabrication process, furnace temperature should be higher than 1980 °C.

3.5 Fabrication Repeatability

In this section, the repeatability of the flat fiber fabrication process was briefly investigated to ensure that the fabrication process is repeatable. A series of flat fiber samples was measured using microscope specifically to observe the fabrication repeatability process. Firstly, capillaries with diameter of 300 μm were fabricated using a standard 25/19 mm fused silica tube. The feed speed and draw speed were adjusted accordingly based on the mass conservation law. It should be noted that the diameter of the capillaries was consistently measured using the diameter gauge and it consistently shows 300 μm . Next, vacuum pressure of 15 kPa was applied to the samples and the flat fibers were fabricated. Three different groups of samples were taken, where each group has a length of about 7 m. The width and thickness of the flat fiber samples were measured at the end of every 1 m using microscope to observe the repeatability of the samples. The results were shown in Table 3.5 for the width measurement and Table 3.6 for the thickness measurement.

Table 3.5: Flat fiber width measurements.

Sample	Set 1 (μm)	Set 2 (μm)	Set 3 (μm)	Standard deviation
1	385.71	385.71	382.14	2.06
2	385.71	392.86	385.71	4.13
3	389.29	392.86	382.14	5.46
4	385.71	385.71	382.14	2.06
5	385.71	385.71	382.14	2.06
6	385.71	385.71	382.14	2.06
7	382.14	371.43	382.14	6.18

Table 3.6: Flat fiber thickness measurements.

Sample	Set 1 (μm)	Set 2 (μm)	Set 3 (μm)	Standard deviation
1	103.57	107.14	103.57	2.06
2	107.14	107.14	107.14	0.00
3	96.43	107.14	107.14	6.18
4	103.57	107.14	103.57	2.06
5	100.00	107.14	103.57	3.57
6	107.14	107.14	103.57	2.06
7	107.14	114.29	107.14	4.13

This crude method to observe the flat fiber repeatability was sufficient enough to conclude that during the fabrication process, if the drawing parameters remain constant, the width and height of the flat fibers fabricated had an average standard deviation of 3.43 for the width and 2.87 for the thickness of the flat fiber.

3.6 Summary

This chapter presented the effects of drawing parameters on the flat fiber dimensions in flat fiber drawing using a pure silica preform tube (F300 Suprasil glass tubes). The drawing parameters studied were preform wall thickness, furnace temperature, draw speed, feed speed and vacuum pressure. Table 3.7 briefly summarizes the general trend of each drawing parameter studied in this chapter based on the experimental results and Table 3.8 concludes the experimental results. However, this was also subject to other

factors involved during the fabrication process such as whether the range of the furnace temperature used was suitable for the preform material. Some of the effects were also not observed on the flat fiber, as the effect was more significant on the fabrication of the capillary.

In this chapter, the focus was more on the effects of drawing parameters on the fabrication of flat fibers. It was found that to ensure greater control of the flat fiber dimension, a fused silica preform with a wall thickness of more than 3 mm could be used with a furnace temperature of 2100 °C and vacuum of 2 - 4 kPa to flatten the flat fiber. In the next chapter, the control of flat fiber dimensions will be investigated.

Table 3.7: General trend of drawing parameter studied in Chapter 3.

Drawing parameter	Effect on outer diameter (OD) of capillary	Effect on flat fiber dimension
Preform wall thickness	<u>Thick wall thickness:</u> OD decrease slower with increasing temperature. <u>Thin wall thickness:</u> OD decrease rapidly with increasing temperature.	<u>Thick wall thickness:</u> Higher vacuum pressure is required to flatten the capillary. <u>Thin wall thickness:</u> Only low vacuum pressure is required to flatten the capillary.
Furnace temperature	<u>High temperature:</u> Smaller OD and lower drawing tension. <u>Low temperature:</u> Higher OD and higher drawing tension.	<u>High temperature:</u> Eccentricity of flat fiber is maintained for a longer time before reaching a stagnant value. <u>Low temperature:</u> Eccentricity of flat fiber is maintained for a shorter time before reaching a stagnant value.
Draw speed	<u>High draw speed:</u> Smaller OD. <u>Low draw speed:</u> Higher OD.	Not observed.

Table 3.7: General trend of drawing parameter studied in Chapter 3 (continued).

Drawing parameter	Effect on outer diameter (OD) of capillary	Effect on flat fiber dimension
Feed speed	<u>High feed speed:</u> OD decrease rapidly with increasing draw speed <u>Low feed speed:</u> OD decrease slower with increasing draw speed	Not observed.
Vacuum pressure	Not observed	<u>High vacuum pressure:</u> Deformed flat fiber, once fiber become flattened <u>Low vacuum pressure:</u> Flatten capillary to flat fiber

Table 3.8: Summary from effect of drawing parameters.

Drawing parameter	Conclusion
Furnace temperature	<ul style="list-style-type: none"> Furnace temperature play an important role in controlling the outer diameter of a capillary and the final flat fiber dimension. Outer diameter of capillaries fabricated from a thin preform decreases more rapidly with increasing temperature.
Preform wall thickness	<ul style="list-style-type: none"> Preform wall thickness influenced the thickness of the fabricated capillary and the final flat fiber dimension. For better control of the capillary dimension, a thick preform was recommended.
Draw speed and feed speed	<ul style="list-style-type: none"> At the same draw speed with two different feed speeds, the higher feed speed resulted in a larger outer diameter. A higher feed speed was proportional to a high draw speed. The draw speed and feed speed using different preform wall thickness had nearly similar effect on the outer diameter capillary and the final flat fiber dimension.
Vacuum pressure	<ul style="list-style-type: none"> The vacuum pressure affected the thin preform more significantly compared to the thick preform. Vacuum pressure affects flat fiber with a different preform wall thickness differently due to the different volume of the preform which gives different surface tension effects.

CHAPTER 4: CONTROL OF FLAT FIBER DIMENSIONS

4.1 Introduction

In terms of drawing parameters, the drawing process for conventional optical fibers is a function of furnace temperature, draw speed and feed speed. However, for flat fiber fabrication, the drawing process is not only a function of furnace temperature, draw speed and feed speed, but is also a function of vacuum pressure and preform wall thickness.

In Chapter 3, the drawing parameters for capillary and flat fiber were studied and investigated using a pure silica preform tube (F300 Suprasil glass tubes) in order to see its effects on the dimension of a flat fiber. The summary and conclusion of the effects can be seen in Table 3.7 and Table 3.8, Chapter 3. These drawing parameters affected the formation of the neck down profile during the fabrication process, which in turn, affected the final flat fiber dimension and shape. The physical and the core dimension of the flat fiber affects the type of fiber that can be coupled or spliced to the flat fiber. For example, a flat fiber with a thickness and core size that is similar to the diameter (cladding and core) of a single mode fiber can be coupled together with lower coupling loss. Controlling these characteristics require optimization of the fabrication parameters involved.

The results obtained in Chapter 3 are useful as it provides basic understanding, guidance and intuitiveness on the fiber drawing process because it focuses on capillary fabrication and dimensional characterization. It is relevant to control the capillary fabrication as the thickness of the capillary directly influences the dimension of the flat fiber. It should be noted that only geometrical characterization was done for the capillaries and flat fibers fabricated in Chapter 3. Optical characterization was not done due to the pure silica preform tube used, which lack the core layer required for light guidance and propagation. In this chapter, the focus will be on the control of the flat fiber dimensions.

Literature have shown that the drawing conditions using doped preforms with specific refractive index profiles may affect the core size of a fiber (Lyytikainen *et. al*, 2004, Yan & Pitchumani, 2006 and Chen & Jaluria, 2009). Thus, further in this chapter, another characteristic which can be controlled through the fiber fabrication process which is the core size will be studied and investigated. The fiber core size affects the wavevector of the transverse waves, which determine the mode of light propagation in the flat fiber. The core size is primarily controlled by the amount of dopant in the preform tube and the thickness of the preform tube. However, the fabrication of preforms is beyond the scope of this thesis so investigation in this chapter will be done using available doped preforms. Fabrication of flat fibers from doped preform tubes will be investigated in terms of its drawing conditions to see its effect on the flat fiber physical and core dimension.

Compared to fabrication of capillaries and flat fibers using pure silica preform (which only has one viscosity parameter involved), controlling the drawing conditions for doped preforms is less straightforward as each dopant material will have its own viscosity, which may cause thermal expansion mismatch with the viscosity of the cladding material (Chen & Jaluria, 2009). Issues that may arise during the drawing process include dopant diffusion (Lyytikainen *et. al*, 2004, Yan & Pitchumani, 2006 and Chen & Jaluria, 2009). The composition of the core and cladding materials also affects the draw tension, which influence the fiber strength (Paek, 1999).

In this chapter, potential problems related to the fabrication process of a doped silica preform tube will also be identified and a method to solve the problems will be proposed. A general understanding to design a flat fiber for specific applications can be deduced from the results obtained. At the same time, the experimental setup will be designed in such a way that the effect of the fabrication process on the dimension and core size of the flat fiber can be observed. Due to limited samples, many experimental and fabrication

parameters are varied at the same time, and the effect of these parameters will be interrelated.

4.2 Literature Review

This chapter begins with a literature review on the effect of drawing conditions on dopant diffusion during fiber drawing. Dopants are materials commonly put into the core layer of optical fibers during the preform fabrication process to either increase or decrease the refractive index of the optical fiber (Chen & Jaluria, 2009). Examples of commonly used dopant materials to increase the refractive index are germanium oxide (GeO_2), phosphorus pentoxide (P_2O_5), titanium dioxide (TiO_2) and aluminium oxide (Al_2O_3). Dopant materials used to decrease the refractive index are fluorine and boron trioxide (B_2O_3). However, dopants also change other properties of the material such as its absorption coefficient and viscosity (Chen & Jaluria, 2009).

As discussed previously in Chapter 2, the drawing process is a function of viscosity (affected by the furnace temperature) which will affect the neck down profile of the final fabricated fiber. The dopant concentration and its distribution profile in the preform is set during the preform fabrication process to meet specific optical applications. However, due to high furnace's temperature during the fiber drawing process, diffusion of the dopant may occur. When the dopant material diffuses, the refractive index profile and optical properties such as the dispersion properties of the final optical fiber will be affected (Lyytikainen *et. al*, 2004). Controlling the dopant diffusion during fiber drawing is complicated since it is interrelated with many fabrication parameters such as temperature, dopant materials, profile of the dopants, draw tension and defect of the starting preform (Huang *et al.*, 2008 and Chen & Jaluria, 2009). Table 4.1 summarizes the effect of fabrication parameters or process on dopant diffusion in fiber fabrication.

Table 4.1: Effect of drawing conditions on dopant diffusion.

Observation on dopant diffusion	Conclusion	Fabrication parameter / process	Reference
1. Change in GeO ₂ distribution from preform and drawn fiber.	1. Ge diffusion occur during drawing process when preform is heated and collapsed to neck down region.	Furnace temperature	Hersener & Huber, 1984
1. High temperature for a period of time can change dopant distribution in core and inner cladding of fiber due to dopant diffusion. 2. Study of surface topology measured by atomic force microscope was done between fiber fabricated at 2100 °C and 1800 °C. The fiber drawn at 2100 °C has lower Ge concentration. 3. Fibers drawn in furnace with a longer heating zone experienced more diffusion.	1. Fiber should be drawn at lower furnace temperature to minimize diffusion. 2. Fiber should be drawn at higher speed to minimize diffusion.	Furnace temperature and draw speed	Lyytikainen <i>et. al</i> , 2004
1. Diffusion coefficient is very small at low temperatures. 2. When furnace wall temperature is low, the rate of dopant diffusion becomes very small and the final refractive index of the fiber is the same profile as the preform.	1. Fiber should be drawn at lower furnace temperature to minimize diffusion.	Furnace temperature	Yan & Pitchumani, 2006
1. Viscosity and diffusion coefficient vary rapidly with temperature.	1. Control of dopant diffusion from core into cladding region can be done by controlling the feed speed.	Feed speed	Huang <i>et al.</i> , 2008

Table 4.1: Effect of drawing conditions on dopant diffusion (continued).

Observation on dopant diffusion	Conclusion	Fabrication parameter / process	Reference
<ol style="list-style-type: none">1. Effect of GeO₂ concentration is more significant at higher temperature at higher draw speed.2. The concentration of E' defects increase with increasing GeO₂ concentration because of higher preform temperature.3. Viscosity of the GeO₂ doped silica core decreases with increasing GeO₂ concentrations and higher preform temperature.4. Higher draw speed reduces the concentration of E' defects due to lower preform temperature.5. The draw tension decreases with increasing GeO₂ concentration.	<ol style="list-style-type: none">1. Dopant concentration depend on the furnace temperature and draw speed of fiber drawing process.	Furnace temperature, draw speed and draw tension	Chen & Jaluria, 2009

According to Fick's Law, the diffusion process during optical fiber drawing is independent of the dopant concentration in the preform and solely depend on the process temperature as stated by Arrhenius equation (Lyytikainen *et al.*, 2004). For GeO₂ doped glass optical fiber, the widely used diffusion coefficient equation is defined as (Yan & Pitchumani, 2006):

$$D = D_0 e^{-E/k_B T} \quad (4.1)$$

where D_0 is the inert diffusion constant which is $1.875 \times 10^4 \text{ m}^2/\text{s}$, E is the activation energy which is $7.69 \times 10^4 \text{ J}$, k_B is the Boltzmann constant and T is the temperature in Kelvin.

The refractive index of the fiber can be expressed as a function of the dopant concentration using the Lorentz-Lorentz equation as defined in Yan & Pitchumani, 2006. For small amount of dopants added to a pure silica glass, the surface tension, specific heat and thermal conductivity does not change much so the values can be assumed to be similar to pure silica (Chen & Jaluria, 2009).

The refractive index and absorption coefficient are strongly dependent on the type and concentration of the dopants (Chen & Jaluria, 2009). The linear relationship between the change in refractive index and dopant concentration for GeO_2 and B_2O_3 is defined as:

$$\Delta = c\chi \quad (4.2)$$

where c is a constant, χ is the mole fraction in % and Δ is the difference in refractive index n between doped and pure silica and is defined as:

$$\Delta = \frac{n_{\text{core}} - n_{\text{cladding}}}{n_{\text{core}}} \quad (4.3)$$

According to Kirchhof *et al.*, 2000, diffusion coefficients also increased with growing concentrations and co-doping of different dopants.

4.3 Fabrication of Doped Flat Fiber

In this section, the effect the drawing conditions on flat fibers fabricated from germanium oxide (GeO_2) doped preforms will be investigated. GeO_2 is one of the most commonly used dopants in optical fibers due to its refractive index and optical dispersion properties. It also has a similar atomic structure compared to silica (Izawa & Sudo, 1987).

Adding GeO₂ to a pure silica cladding increases its absorption coefficient (in the UV region) and lowers its viscosity (Chen & Jaluria, 2009). Germanium doping also makes silica photosensitive, allowing possibility of inducing nonlinear effects such as second harmonic generation (Alessi *et al.*, 2011). The viscosity of a silica glass uniformly doped with GeO₂ depends on the dopant concentration and is shown in the following equation (Tajima *et al.*, 1994):

$$\mu_{Ge} = \mu_{Si} \exp(-A\Delta) \quad (4.4)$$

where μ_{Si} is the viscosity of a pure silica glass, Δ is the relative index difference in percentage between GeO₂ -doped silica glass and pure silica glass and A is a positive constant defined as 0.5 (Chen & Jaluria, 2009). Equation 4.4 is also valid for preforms with larger amount of dopants (Tajima *et al.*, 1994).

4.3.1 GeO₂ doped flat fibers using single stage drawing method

In this section, the fabrication of a doped flat fiber was done using a preform doped with 36.7 mol% germanium oxide (GeO₂). The method of drawing process was single stage drawing. In a single stage drawing process, the flat fiber is directly drawn from the preform to its desired size. This investigation was done to study the effect of single stage drawing and highly doped preform on the fabricated flat fiber. The original preform tube before being doped with germanium oxide was 25 mm (outer diameter)/19 mm (inner diameter). The preform was manufactured using MCVD technique at Multimedia University, Cyberjaya, Malaysia. The proposed fabricated flat fiber dimension was 300 μm x 125 μm . The thickness of the proposed flat fiber was chosen at 125 μm to reduce coupling loss when coupling with commercially available single mode fibers which usually have 125 μm cladding diameter. The furnace temperature was initially set slightly lower at 2100 °C because earlier characterization work shows that for a similar thickness

preform using a pure silica preform tube, the estimated suitable temperature was at 2140 °C and also because the preform was highly doped with GeO₂.

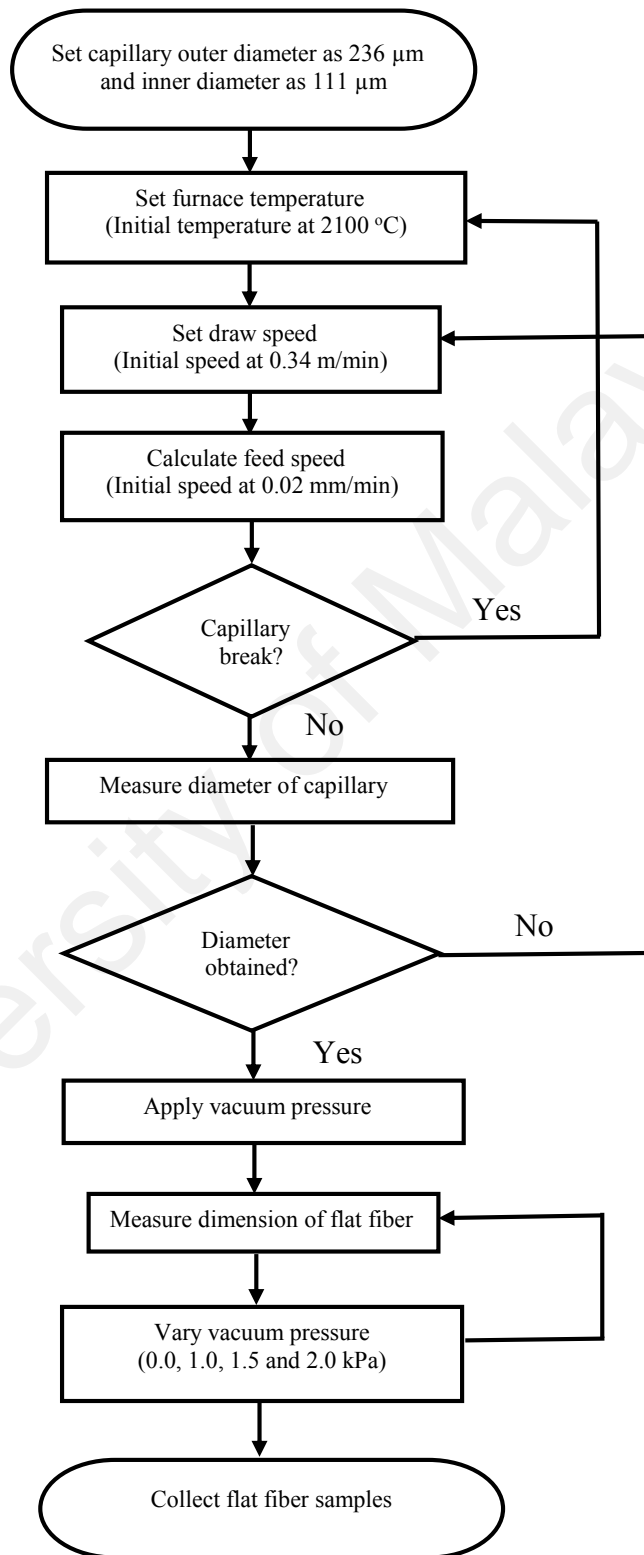


Figure 4.1: Flowchart for the fabrication of GeO₂ doped flat fibers using single stage drawing method.

The outer and inner diameter of the capillary (before being flattened) can be estimated using Equation 2.14 – 2.16 in Chapter 2 to get the proposed flat fiber width and thickness of $300\text{ }\mu\text{m} \times 125\text{ }\mu\text{m}$ (with core width of $175\text{ }\mu\text{m}$). To achieve a flat fiber thickness of $125\text{ }\mu\text{m}$, the thickness of the capillary was estimated at $62.5\text{ }\mu\text{m}$. The outer diameter of the initial capillary was estimated $236\text{ }\mu\text{m}$ and the inner diameter of the capillary was approximately $111\text{ }\mu\text{m}$. The flat fiber was then fabricated using the initial drawing conditions as seen in the flow diagram in Figure 4.1. The flat fiber's width and thickness during the fabrication process was observed using fiber diameter measurement unit, model ODAC 15XY-J from Zumbach. The initial fiber drop occurred at the furnace temperature of $2000\text{ }^{\circ}\text{C}$.

Drawing conditions were then changed accordingly depending on the proposed width and thickness of the flat fiber. As previously discussed, for a pure silica preform, the eccentricity of the flat fiber depends largely with the vacuum pressure applied to the preform. Therefore, during this fabrication process, the vacuum pressure was varied while the temperature was kept constant at $2100\text{ }^{\circ}\text{C}$.

Figure 4.2 shows the change in the measurement of the diameter x and y (in mm) as the drawing time increased (in minutes). For all analysis based on drawing time, it should be noted that the first few minutes of the drawing time (after the initial fiber drop) are the stabilization region. In the stabilization region, the fiber's diameter was not yet affected by the drawing parameters as it was drawn from the lower part of the preform in the furnace, which was the part after the heating zone length. Any changes due to heating zone length should take effect after the preform at the lower end of the heating zone length is being pulled. The time taken for the stabilization region depends on the preform volume, fiber volume and draw speed. Figure 4.2 shows the change in the dimension of the flat fiber as drawing time increases. The drawing time has been divided into 4 regions,

where each region has different drawing parameters. The drawing time does not directly affect the dimension of the flat fiber as it is only used to represent different drawing parameters. Only the drawing parameters such as furnace temperature, draw speed, feed speed and vacuum pressure will influence the dimension of the flat fiber.

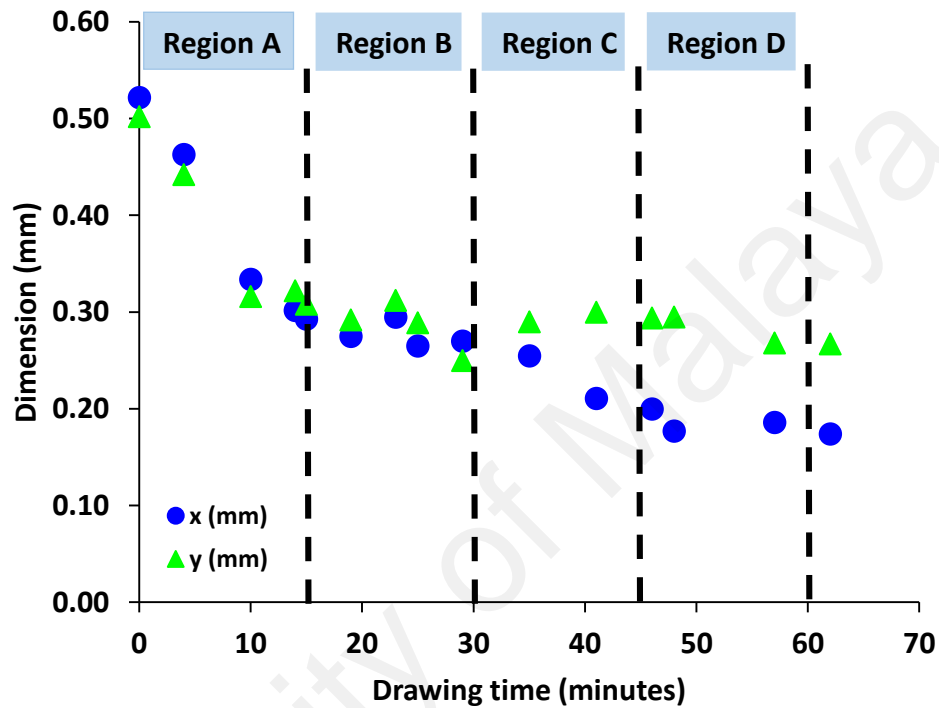


Figure 4.2: Diameter x and y (in mm) during the drawing process (the x -axis represents the drawing time). Regions A-D show the changes in drawing conditions.

Table 4.2: Changes in drawing conditions during the fabrication process. Regions A-D indicate the region where drawing conditions were changed.

Region	Vacuum pressure (kPa)	Average draw speed (m/min)	Average feed speed (mm/min)
A	0.0	0.45	0.02
B	1.0	0.34	0.07
C	1.5	0.26	0.10
D	2.0	0.28	0.13

The draw speed and feed speed were continuously controlled accordingly to get the required dimensions as seen in Table 4.2. The fiber was cut and collected after every 1 m.

The vacuum pressure was increased after 5 samples of 1 m length each had been collected.

The total fiber length collected was 20 m.

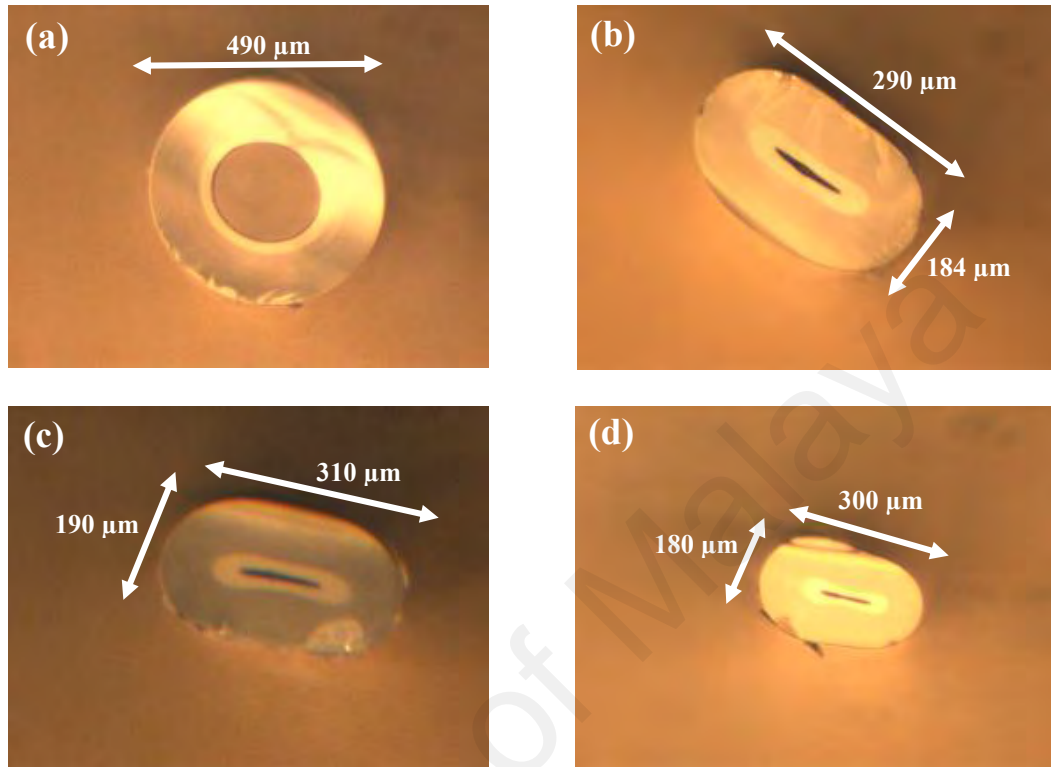


Figure 4.3: Microscope image of the cross section of fabricated flat fiber for vacuum settings of 0, 1.0, 1.5 and 2.0 shown in Figures 4.3 (a), (b), (c) and (d) respectively (Reproduced from Dambul *et al.*, 2011 with permission).

Figures 4.3 (a) – (d) show the image of the flat fiber during a particular vacuum pressure captured using microscope with a total magnification of 100 x. It can be seen that the capillary tube slowly changed its shape from circular to elliptical, while the center hole started to fuse and form a solid flat rod at a vacuum pressure of 2.0 kPa. For a circular optical fiber (at 0 kPa), the optical fiber diameter was almost constant at approximately 480 μm. As the applied vacuum pressure was increased from 1 to 2 kPa, the thickness of the flat fiber decreased to 180 μm. Compared with the pure silica flat fiber drawn from a thick preform, the main significant difference was that the flat fiber was not able to fully flatten as there was an airhole in the middle of the core (seen in Figure 4.3 (b), (c) and (d)). This could be due to the high GeO₂ content in the preform affecting the viscosity and surface tension of the flat fiber. As seen previously in Figure 2.4, Chapter 2, the viscosity

of pure silica is higher than the viscosity of GeO₂ doped silica fiber. The high GeO₂ content added to silica caused the flat fiber to have a lower viscosity, thus being drawn before it can fully flatten.

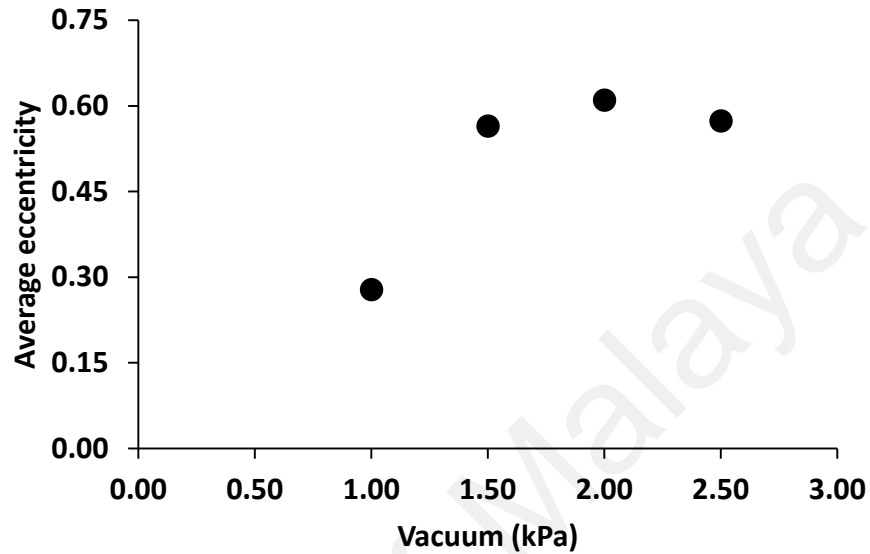


Figure 4.4: Average eccentricity versus vacuum pressure (kPa) at 2100 °C.

Figure 4.4 shows the average eccentricity versus applied vacuum pressure (kPa) at the drawing temperature of 2100 °C. The maximum eccentricity of 0.61 was obtained at vacuum pressure of 2 kPa. This indicated that the vacuum pressure could still be increased. But an increased vacuum pressure of 2.5 kPa had reduced the dimension of the flat fiber as shown in Table 4.3.

In a pure silica capillary, airholes exist due to the effect of surface tension and can be fused with sufficient pressurization (Xue *et al.*, 2006). The applied vacuum pressure was increased in order to fuse the airhole but instead of fusing the airhole, the flat fiber dimension itself became smaller and more circular. When a vacuum pressure of 5 kPa with a temperature of 2075 °C was used, the fiber that was obtained was no longer flat but shaped like a capillary with an average width and thickness of 155 μm x 153 μm. Thus, even at higher vacuum pressure there was an airhole in the middle of the flat fiber

which was previously not observed in the pure silica flat fiber (using thick preform) analyzed in Chapter 3. It was found that at higher vacuum pressure, the force acting towards the center of the preform will increase, which subsequently increased the surface tension of the fiber as the forces are acting parallel to one another. Thus, the 5 kPa vacuum was still unable to seal the airhole due to the increased surface tension. There was also a high concentration of germanium oxide in the core and dopant diffusion could occur, causing the dopant to diffuse into the cladding. This could also prevent the airhole from sealing. The airhole was also not sealed due to a lack of pressurization (Xue *et al.*, 2006).

Table 4.3: Flat fiber and its core dimensions.

Vacuum (kPa)	Samples physical dimension				
	Flat fiber width (w) (in μm)	Flat fiber thickness (t) (in μm)	Core width (w_c) (in μm)	Core thickness (t_c) (in μm)	Core aspect ratio
0	490	470	75	68	-
1.0	290	184	132	27	4.89: 1
1.5	310	190	130	25	5.20: 1
2.0	300	180	140	12	11.67: 1
2.5	210	130	90	4	22.50: 1

The width and thickness of the flat fiber and its core were measured using optical microscope and shown in Table 4.3. The core aspect ratio shown in the table is defined as the ratio between the width and thickness of the flat fiber core. The ability to fabricate flat fibers with different core aspect ratio using only one preform is useful as the different core aspect ratio can be expanded for different applications. Starting from vacuum pressure of 1.5 kPa, the capillary tube changed from circular into elliptical shape. The core aspect ratios have increased from 4.89 to a maximum of 22.50 producing a flat fiber with a core thickness of $90\text{ }\mu\text{m} \times 4\text{ }\mu\text{m}$ at vacuum pressure of 2.5 kPa. The final flat fiber dimensions have reduced to $210\text{ }\mu\text{m} \times 130\text{ }\mu\text{m}$.

The flat fiber with a core aspect ratio of 4.89: 1 and 5.20: 1 can be used in arrayed waveguide grating filters. In some arrayed waveguide grating filters, waveguide core dimension ratio of 3.75:1 was used to reduce phase errors caused by the variation of the core width (Lockwood & Pavesi, 2011). As reported by Rockwell *et al.*, 2011, a rectangular shape fiber with core aspect ratio of 28:1 and core aspect ratio of 18.75:1 had been fabricated for fiber laser applications.

The draw tension for the flat fiber was measured during the flat fiber fabrication process. At a temperature of 2075 °C, with a feed rate of 0.15 mm/min and a draw speed of 0.15 m/min, the average draw tension of the fabricated fiber was 42.33 g. According to Oh *et.al.*, 1983, for optical fiber fabrication, a lower drawing tension (> 5 g) was useful for fabrication of uniform high strength fibers while a higher drawing tension (> 50 g) was found applicable for low loss fibers with a large silica core.

During the fiber drawing process, it was observed that no fiber break occurs. This could be due to several reasons which are:

1. The thick preform used had higher material volume which was capable to supply sufficient material at the predetermined flat fiber's thickness. Thus, fiber was less prone to fiber breaking.
2. Optimized drawing temperature of 2100 °C and low draw speed (average of 0.33 m/min during the whole drawing time). If a low draw speed was used with a high temperature, this may cause fiber to break (Cheng & Jaluria, 2004).

In conclusion, single stage drawing method is simple but it can be difficult to control the flat fiber dimensions. Fabrication of flat fibers using high concentration of GeO₂ and thick preform vary dependently with applied vacuum pressure where increasing the vacuum pressure was producing flat fibers with smaller dimensions, which in turn

affected the core dimension and core aspect ratio. A single airhole also existed in the middle of the core, which could not be fused even at increased vacuum pressure. Due to the thick preform used, no fiber break was observed during the fabrication process.

4.3.2 Single stage drawing method for specific diameter

In the previous section, it can be seen that using a single stage drawing method produced doped flat fibers, though with an airhole defect in the middle of the core. The ability to fabricate flat fibers with different core sizes, dimensions and dopant concentration is desirable. From Equation 3.8, with a given preform diameter and at specific values of the draw speed and feed speed, a flat fiber with a specific outer dimension could be fabricated. However, the draw speed and feed speed should be set within the limits of the drawing tower capability. In this section, a series of experimental trials were performed using pure silica preform tubes to investigate the effects of single stage drawing on specific fiber capillary dimensions. The trial experiments used Suprasil F300 glass tubes with an average outer diameter of 25 mm and average inner diameter of 19 mm. Two capillary sizes were investigated, which were 125 μm and 1.25 mm.

The first fiber capillary proposed was 125 μm , which will be drawn directly from the preform with a diameter of 25 mm. Using Equations 2.14 – 2.16 from Chapter 2, the flat fiber fabricated will have a thickness of 30 μm and width of 180 μm (after vacuum applied).

Drawing conditions such as draw speed, feed speed and furnace temperature were varied to see their effects on the capillary dimensions. The draw speed and feed speed required can be calculated from Equation 3.8. The second fiber capillary proposed was a larger diameter capillary of 1.25 mm. Based on Equation 3.8, with similar draw speeds used to fabricate the 125 μm capillaries, the feed speed need to be increased accordingly. Table 4.4 shows a summary of the experimental work done in this section. The objective

of the experimental work was to determine which specific diameter was easier to control in terms of drawing parameters.

Table 4.4: Summary of experimental work done in Section 4.3.2

Desired Capillary Diameter	Controlled Variable	Manipulated Variable	Measurement (capillary)
125 μm	Furnace temperature	Draw speed Feed speed	Outer diameter
	Draw speed Feed speed	Furnace temperature	
	Furnace temperature Feed speed	Draw speed	
1.25 mm	Furnace temperature Feed speed	Draw speed	Outer diameter
	Draw speed Feed speed	None	

4.3.2.1 Fabrication of 125 μm capillary from 25 mm preform

In this section, attempts were made to fabricate a fiber capillary with a diameter of 125 μm from a preform with diameter of 25 mm using single stage drawing. The results were shown in Figure 4.5. The furnace temperature was fixed at 2050 $^{\circ}\text{C}$ in Region A. From Equation 3.8, it was calculated that to achieve a diameter of 125 μm from a preform with an outer diameter of 25 mm, a feed speed of 0.05 mm/min and a draw speed of 2 m/min was required. The first few minutes of the drawing process was the stabilization region. In Region A, the changes in the diameter x and y were seen when the feed speed and draw speed were changed. The feed speed was gradually increased to 0.05 mm/min and the draw speed was gradually increased to 2.2 m/min. As the required diameter was not yet achieved, the draw speed was increased but before the appropriate feed speed was applied, fiber break had occurred (in Figure 4.5, this was indicated when the diameter was 0 mm). Fiber break occurred after the draw speed was increased to 2.5 m/min while maintaining the feed rate of 0.05 mm/min. As the draw speed was increased, the surface temperature

of the fiber decreased, causing a high viscosity. At a high viscosity, there was a lack of material flow and the fiber break occurred due to viscous rupture (Choudhury & Jaluria, 1998a).

In Region B of Figure 4.5, the drawing process was repeated and the feed speed was gradually increased to 0.03 mm/min with a draw speed of 1.2 m/min at a higher temperature of 2100 °C. From Equation 3.8, theoretically, at this draw speed and feed speed, the required diameter of 125 μm should be achieved. As the required diameter was still not achieved, the furnace temperature was reduced to 2080 °C.

In another attempt to obtain the desired diameter in Region B, the fiber draw speed was increased to 2 m/min with feed speed of 0.05 mm/min but fiber break occurred. From Figure 4.5, some of the general trend line obtained from Chapter 3 for the fabrication of capillaries using pure silica preform tubes was observed, which are lower fiber diameter as the draw speed and furnace temperature increased.

In Figure 4.6, the feed speed was fixed at 0.05 mm/min and the draw speed was fixed at 2 m/min. The effect of furnace temperature in obtaining the desired fiber diameter was investigated. The temperature was initially set at 2130 °C. As the required diameter of 125 μm was not achieved, the temperature was gradually reduced to 2115 °C and again reduced to 2100 °C. Fiber break occurred when the average diameter was 270 μm . However, in this case, the fiber break probably occurred due to a sudden change in the temperature. A change in the temperature to a lower temperature caused an increase in the viscosity, and the fiber may break due to viscous rupture which happens due to lack of material flow (Choudhury & Jaluria, 1998a).

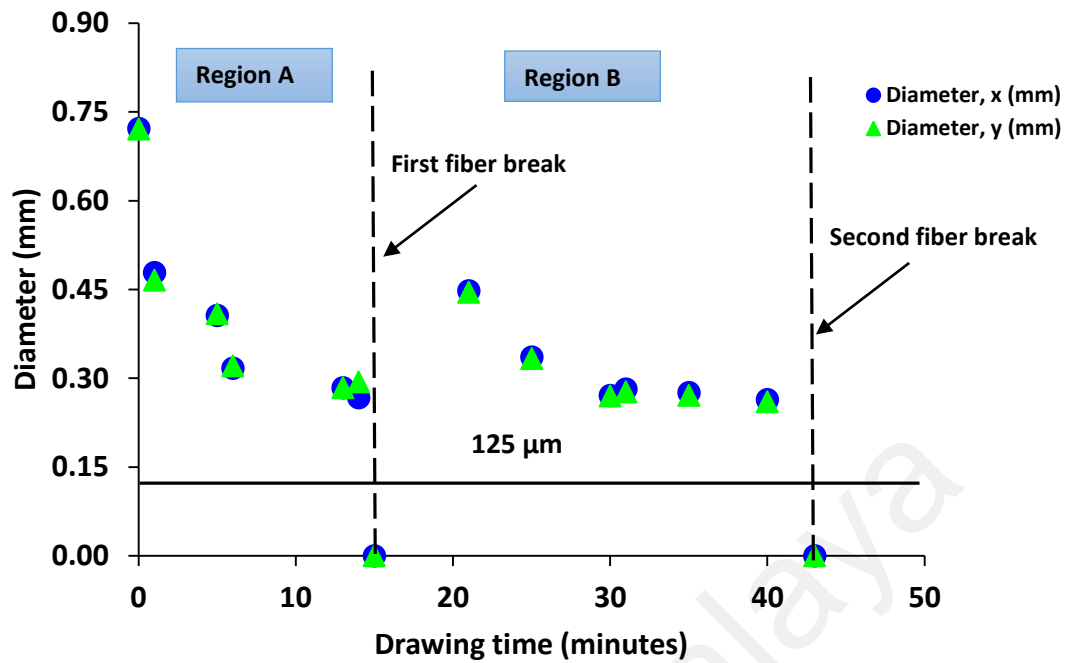


Figure 4.5: Diameter x and y (in mm) versus drawing time with two regions of drawing conditions. Desired diameter was 125 μm as shown in the straight line.

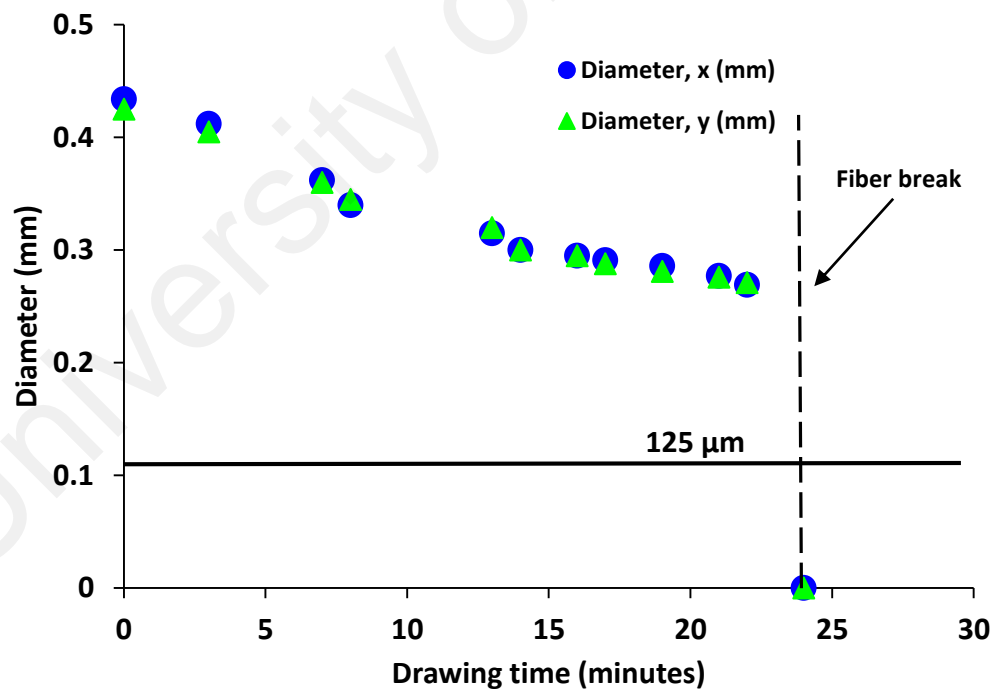


Figure 4.6: Diameter x and y (in mm) versus drawing time at a constant feed speed and draw speed.

In Figure 4.7, the feed speed was fixed at 0.05 mm/min and the draw speed was increased gradually from 2 m/min to a maximum of 4 m/min before fiber break occurred. The draw speed was increased as the desired diameter was not achieved. The furnace temperature was maintained in the region of 2105 °C - 2115 °C. The average diameter was 153 μm when fiber break occurred. This diameter was closer to the desired diameter of 125 μm . However, the fiber break was probably due to higher defect concentrations at higher speed and higher furnace temperature (Choudhury & Jaluria, 1998a).

The results from Figures 4.5 – 4.7 show that from a preform tube with an outer diameter of 25 mm and inner diameter of 19 mm, it was difficult to obtain a capillary with 125 μm despite following the draw speed and feed speed as per the volume reduction ratio. Fiber breaks also occurred during the fabrication process and the reasons for these breaks had been discussed.

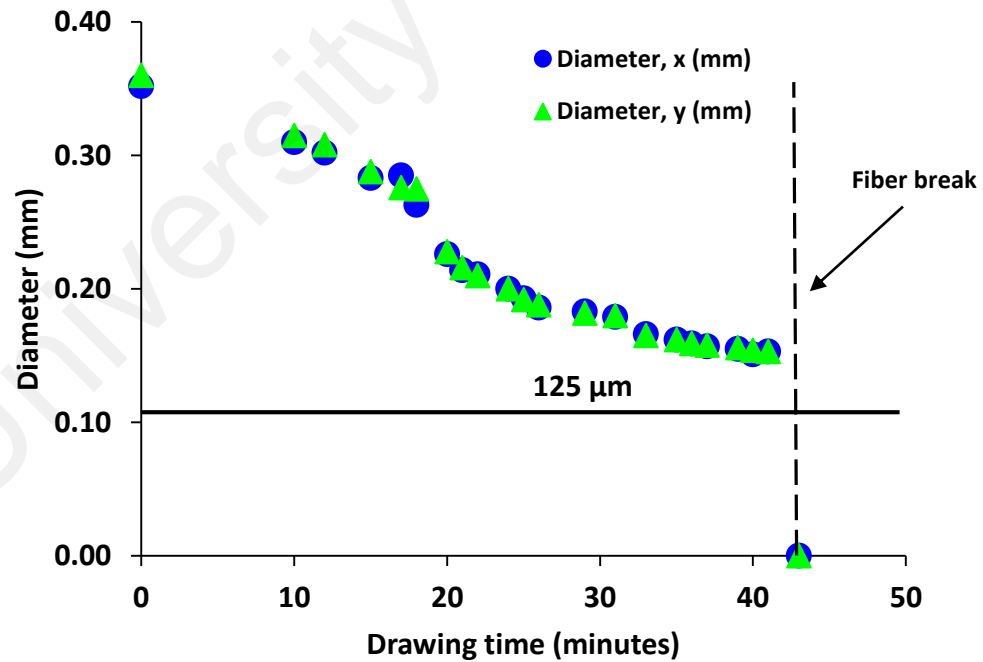


Figure 4.7: Diameter x and y (in mm) versus drawing time at a constant feed speed.

4.3.2.2 Fabrication of 1.25 mm capillary from 25 mm preform

Results from the previous section had shown that despite varying drawing parameters, it was difficult to obtain the capillary dimension of 125 μm from a pure silica preform with an outer diameter of 25 mm. Thus, in this section, the drawing conditions in the fabrication of a 1.25 mm capillary was investigated. From Equation 3.8, with a feed speed of 6.5 mm/min, the required draw speed was 2.6 m/min in order to achieve a 1.25 mm capillary from a pure silica preform with outer diameter of 25 mm. In this experiment trial, the feed speed was kept constant at 6.5 mm/min and the draw speed was slowly increased to 2.6 m/min as shown in Figure 4.8. The furnace temperature was maintained at 2100 °C.

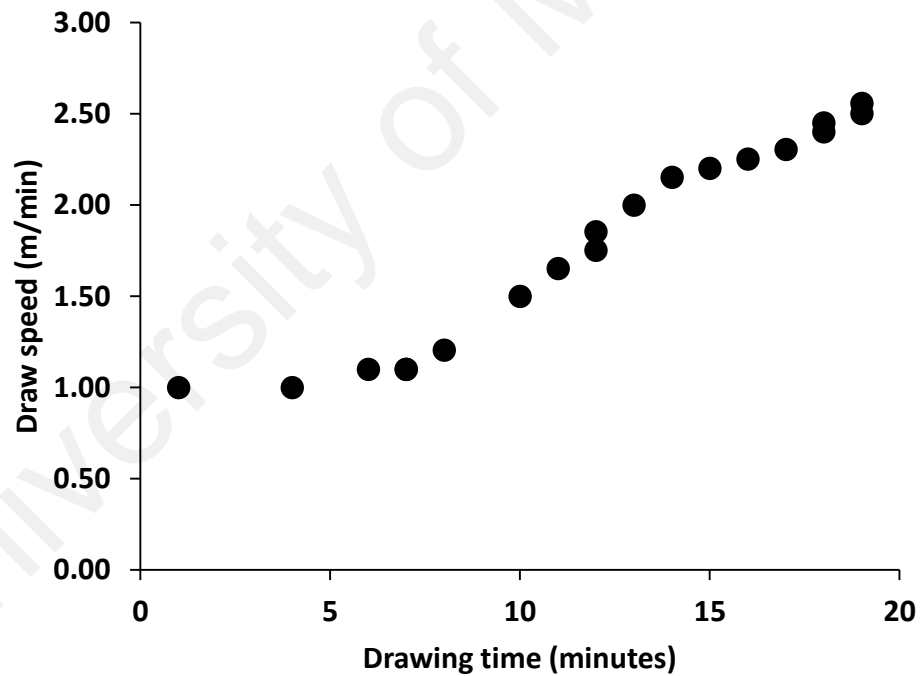


Figure 4.8: Draw speed (m/min) versus drawing time at a constant feed speed of 6.5 mm/min.

The results in Figure 4.9 show that the capillary with a diameter of 1.25 mm was achieved at the feed speed of 6.5 mm/min and draw speed of 2.6 m/min. In Figure 4.9, the first 8 minutes of fiber drawing was the stabilization region. The stabilization region had been explained in Section 4.3. Results from Figure 4.9 show that the volume

reduction ratio could be used to predict the draw speed and feed speed with an acceptable accuracy for a 1.25 mm capillary. To determine the repeatability of this, a different feed speed and draw speed was also performed in order to achieve an outer diameter of 1.25 mm from a preform of 25 mm. The results were shown in Figures 4.10 and 4.11. The results in Figure 4.10 show that the required diameter of 1.25 mm was achieved at the feed speed of 2.6 mm/min and draw speed of 1 m/min, which was similar to the ratio required by the volume reduction ratio. Similar to Figure 4.9, the first 8 minutes of fiber drawing in Figure 4.10 was the stabilization region. No fiber breaks were observed during the experiment.

Figure 4.11 shows the results when the feed speed was 5 mm/min and the draw speed was 2 m/min. The results confirmed that the fabrication process was repeatable and the volume reduction ratio could be used to fabricate specific capillary sizes with an acceptable accuracy. Comparing between Figure 4.10 and Figure 4.11 which had the same preform diameter and desired fiber diameter, it was observed that at a higher draw speed of 2 m/min, less time was required in the stabilization region. This was consistent with the results in the previous chapter which show that when the draw speed increases, the preform spends less time inside the furnace hence was drawn faster (Boll & Nummela, 2010). Table 4.5 shows a summary of the experimental results performed in this section.

Table 4.5: Summary of experimental results.

Feed Speed (mm/min)	Draw Speed (m/min)	Desired Capillary Size	Obtained Capillary Size	Fiber break
0.05 (Region A) 0.03 (Region B)	2.0, 2.2 and 2.5 (Region A) 1.2 (Region B)	125 μ m	No	Yes
0.05	2.0	125 μ m	No	Yes
0.05	2.0 – 4.0	125 μ m	No	Yes
6.5	2.6	1.25 mm	Yes	No
2.6	1.0	1.25 mm	Yes	No
5.0	2.0	1.25 mm	Yes	No

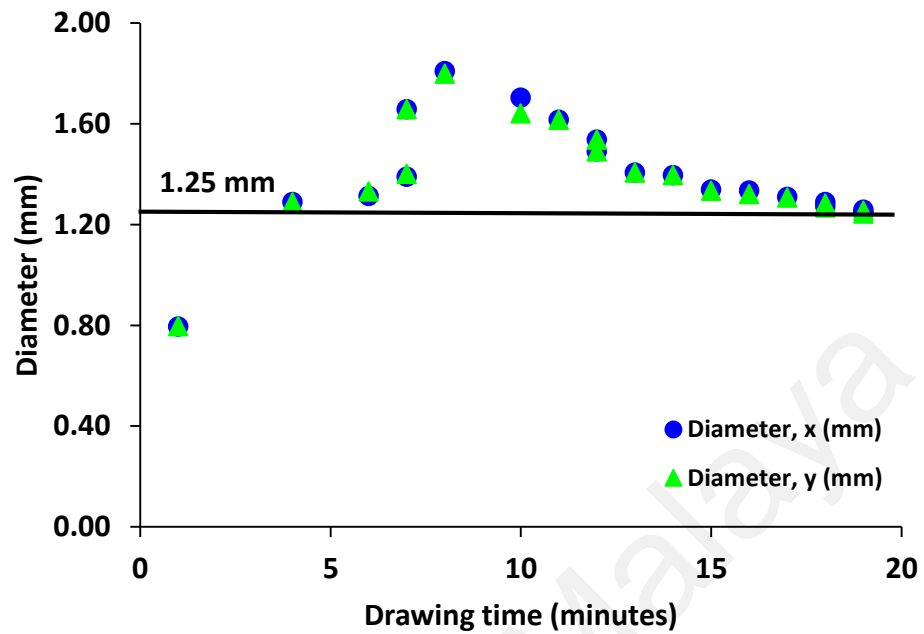


Figure 4.9: Diameter x and y (in mm) versus drawing time at a constant feed speed of 6.5 mm/min.

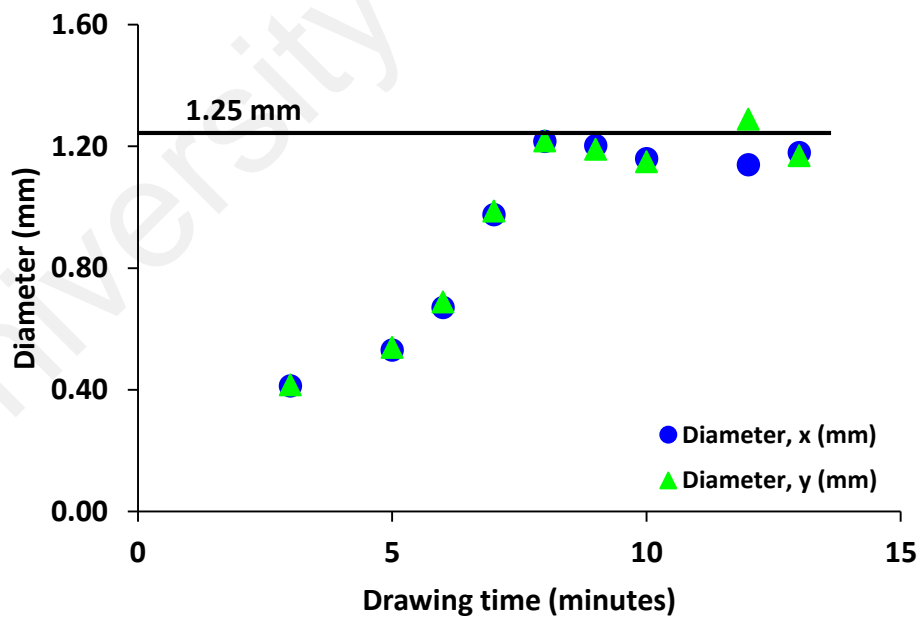


Figure 4.10: Diameter x and y (in mm) versus drawing time (minutes) with feed speed of 2.6 mm/min and draw speed of 1 m/min.

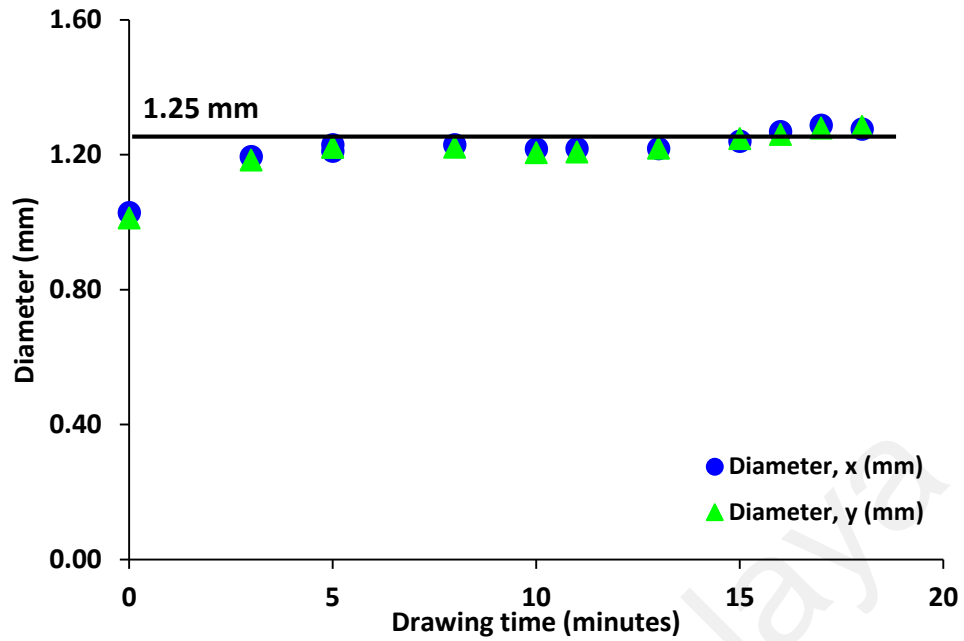


Figure 4.11: Diameter x and y (in mm) versus drawing time (minutes) with feed speed of approximately 5 mm/min and draw speed of 2 m/min.

4.4 Dual Stage Drawing Method

A dual stage drawing method was proposed in this section to achieve better control of the flat fiber drawing process, leading to a more uniform and reliable drawing process. In a dual stage drawing, the preform is first drawn into a capillary about 2 to 3 mm in diameter before being drawn for the second time to the desired flat fiber dimension. During the first drawing stage, internal pressurization can be applied to the tube to ensure it does not collapse. Alternatively, the preform can also be drawn into a flat fiber rod with a width of 1 to 2 mm, before being drawn the second time into micron-size. Figure 4.12 shows the flowchart for the dual stage drawing method.

Once a desired capillary diameter was achieved, vacuum pressure was applied to flatten the capillary into a flat fiber rod. Figure 4.13 shows a microscope image of a pure silica flat fiber rod. Figure 4.14 shows the dimensions of a flat fiber rod that was fabricated using a feed speed of 6 mm/min and draw speed of 2 m/min. Some of the flat fibers obtained have holes at the sides and were more elliptical in shape than flat fiber shaped.

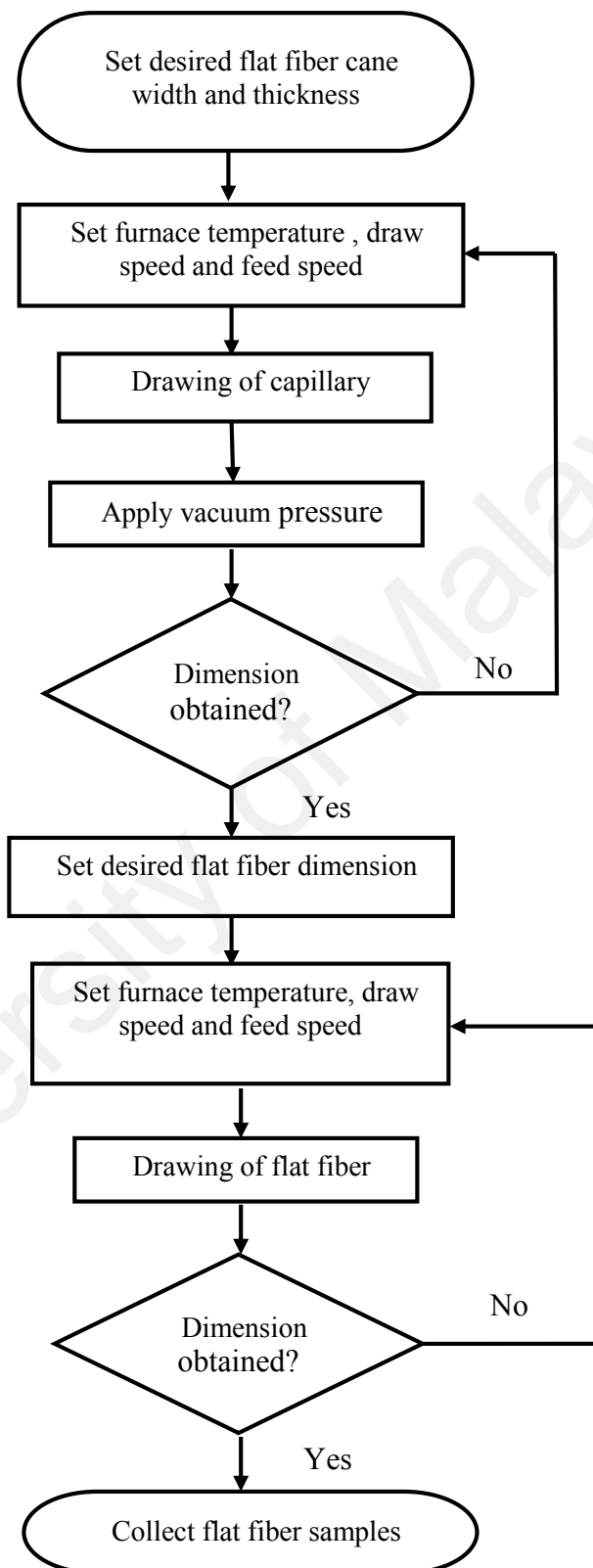


Figure 4.12: Flowchart for the fabrication of flat fibers using two stage drawing method.

The reasons for elliptical shaped flat fibers had been discussed in Chapter 3. From the flat fiber rod, a second drawing was performed to obtain the flat fibers in the desired dimensions. To show repeatability of the flat fiber rod fabrication, Figure 4.15 shows the dimensions of a flat fiber rod that was fabricated using a feed speed of 8.5 mm/min and a draw speed of 2.5 m/min. The diameter obtained was quite uniform, however, some issues faced during the experimental trial to obtain the samples shown in Figure 4.15 was twisting of the flat fiber due to the preform not being tightly attached to the preform chuck. Due to fiber twisting, the fiber fabricated from this rod will also be twisted. Thus, samples from this drawing was not optimized for fabrication of long lengths of fiber.

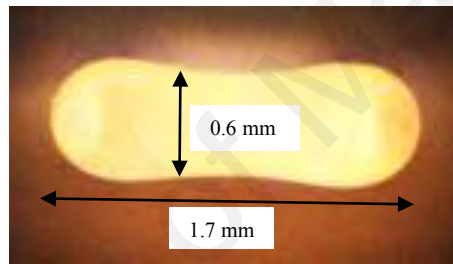


Figure 4.13: Cross section image of undoped flat fiber rod.

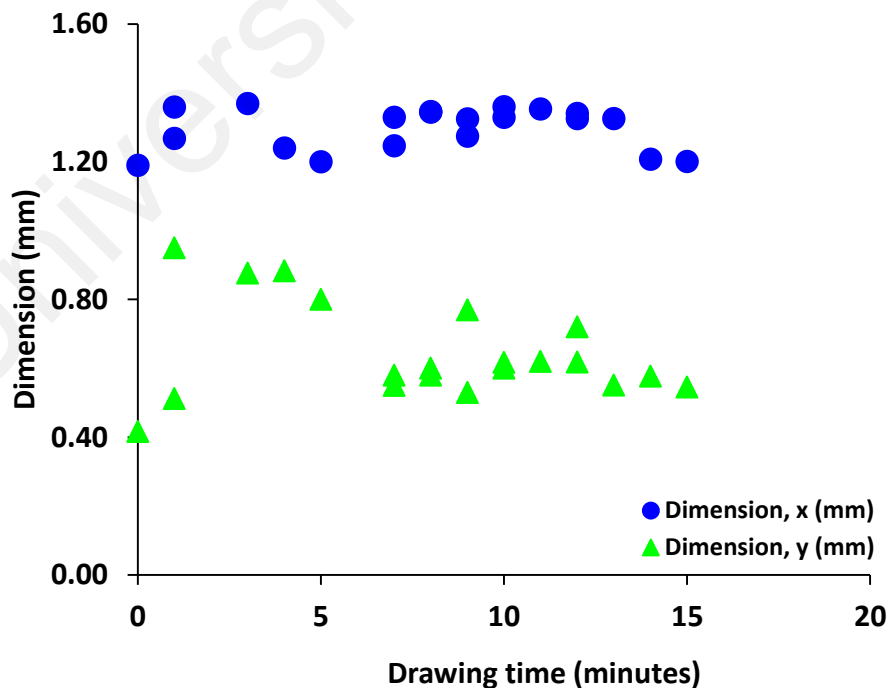


Figure 4.14: Dimension x and y (in mm) versus drawing time (minutes) with feed speed of approximately 6 mm/min and draw speed of 2 m/min.

Table 4.6 shows the drawing conditions and the measured flat fibers drawn from the flat fiber rods during a dual stage drawing.

Table 4.6: Flat fibers obtained using dual stage drawing.

Temperature (°C)	Feed speed (mm/min)	Draw speed (m/min)	Tension (g)	Dimension (μm)
2050	12.08	2	51	250 x 80
2050	12.11	2	54	230 x 80
2060	12.10	2	52	230 x 80
2065	17.00	3	54	260 x 65

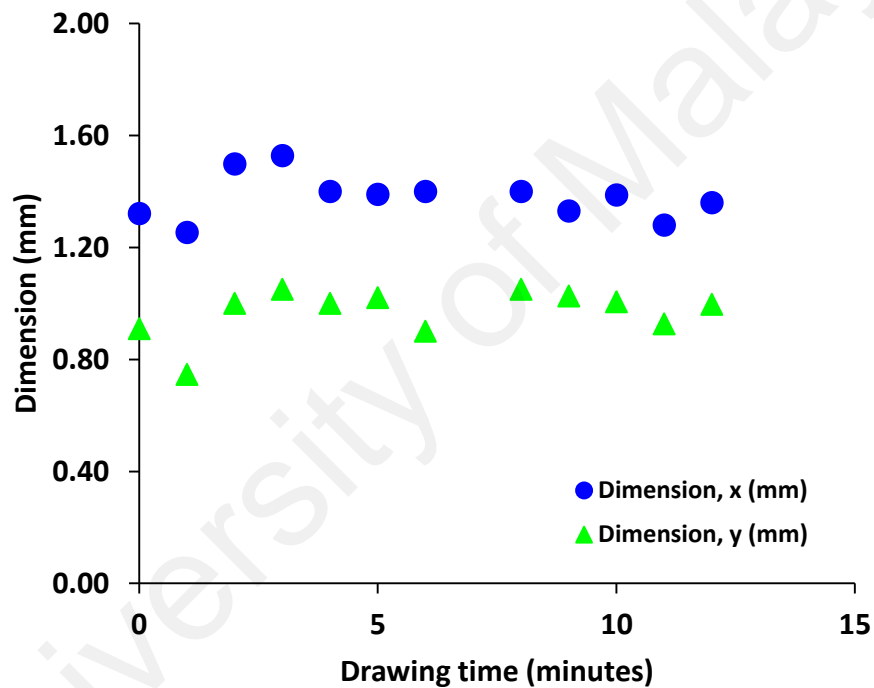


Figure 4.15: Dimension x and y (in mm) versus drawing time (minutes) with feed speed of approximately 8.5 mm/min and draw speed of 2.5 m/min.

In this section, dual stage drawing was performed by fabrication of flat fiber rods with a width of 1 – 2 mm, before drawing the rods for the second time into flat fibers with a width of 250 μm. Figures 4.14 and 4.15 show that the flat fiber rod dimension remain consistent during the drawing process. In conclusion, dual stage drawing method was proposed in flat fiber drawing to achieve better control of the flat fiber dimensions.

4.5 Characterization of Doped Flat Fiber

In this section, basic characterization work will be performed on a flat fiber fabricated using dual stage drawing, from a 25 mm diameter preform doped with a lower GeO_2 concentration of 6 mol%. The first stage of drawing produced capillaries with a diameter of 3 mm before vacuum was applied. After the second stage of drawing, the flat fiber physical properties were characterized using SEM imaging techniques and the cross-section dimension of the samples was measured as $340\text{ }\mu\text{m} \times 168\text{ }\mu\text{m}$ and the average core dimensions were $189\text{ }\mu\text{m} \times 3.96\text{ }\mu\text{m}$ as seen in Figure 4.16. The core thickness varies along the width of the core, where it is $13.9\text{ }\mu\text{m}$ at both edges of the core and upon further magnification of the SEM imaging, the core thickness at the middle of the core was measured as $3.67\text{ }\mu\text{m}$.

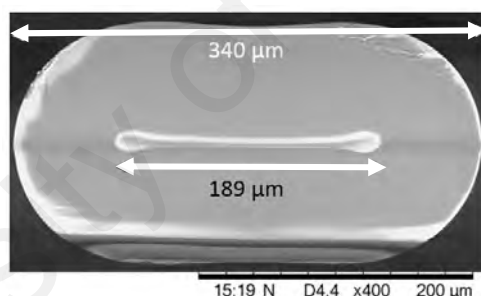


Figure 4.16: Cross section of the flat fiber sample with 6 mol% of GeO_2 .

The fabricated flat fiber sample shows good mechanical strength as it can tolerate a bending diameter of 3.35 cm. The fiber bending tolerance can be further improved by applying polymer coating after the flat fiber was drawn from the furnace. Using an Instron tensile measurement unit, the flat fiber sample can tolerate a load of 9.58 N with a tensile stress of 167.75 MPa. The Young's Modulus for the sample was 32.45 GPa. For comparison purposes, in silica fibers, the Young's Modulus is 73 GPa (Shackelford & Doremus, 2008).

Two experimental setups used to characterize the flat fiber samples were shown in Figure 4.17. Setup (a) was used to measure the insertion loss of the flat fiber samples using cut-back measurement (Derickson, 1998) and setup (b) was used to measure the near field patterns of the flat fiber samples under different signal wavelengths (Hui & Sullivan, 2009). Next, the experimental procedures used to obtain the results were described. In setup (a), the light source was a multichannel laser coupled fiber for wavelengths at 635 nm, 1310 nm and 1550 nm. The laser source (chosen at 1550 nm) was connected to an SMF-28 fiber pigtail and coupled via free space coupling to the flat fiber sample. Both sides of the flat fibers were mounted on positional XYZ-axis stages and clamped using magnetic holders. The end of the fiber sample was then butt coupled to the power meter. For the launching condition, the single-mode optical fiber SMF-28 pigtail was aligned to the middle of the flat fiber sample.

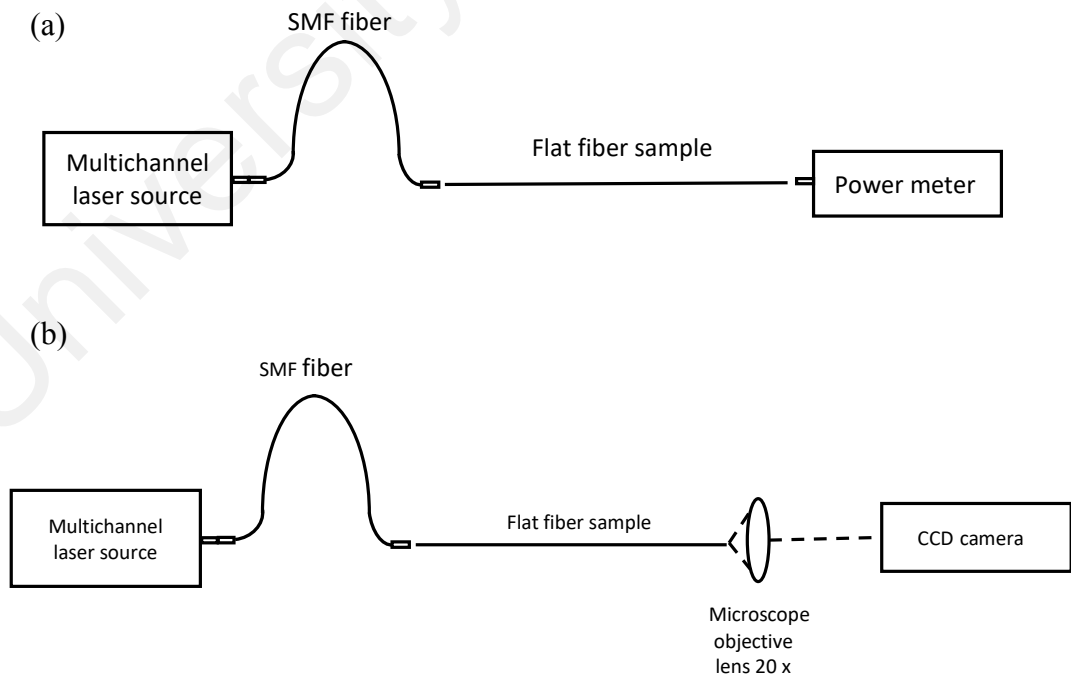


Figure 4.17: Experimental setups for (a) insertion loss measurements and (b) near field measurement.

In setup (b), the length of samples used was 60 cm. The SMF-28 pigtail from the laser source was butt coupled to the flat fiber sample under 3 different launching conditions defined as right, middle and left positions. A ‘Supereyes’ digital magnifier was mounted on top of the connection between the SMF fiber pigtail from the laser source to the flat fiber sample in order to adjust the launching condition and to monitor the fiber position for alignment purposes. In setup (b), the power meter was replaced with a microscope objective lens with magnification of 20X and a CCD camera. The light radiating from the end of the flat fiber sample was coupled to the microscope objective lens to magnify the near field patterns before the intensity profiles was captured by the CCD camera. All optical modes were excited with equal power at the input ends of the flat fiber. The measurement was done for wavelengths of 635 nm, 1310 nm and 1550 nm. The cladding modes were removed by applying index gel near to the output ends of the flat fiber sample. The CCD images of the samples under different launching conditions were then analysed.

4.5.1 Attenuation loss

The attenuation loss of the flat fiber sample was defined as the total light loss inclusive of the coupling loss and was measured using the cut-back method (Shenoy *et al.*, 2009), which compares the received power for different lengths of the sample. The loss, α was defined as:

$$\alpha \left(\frac{dB}{cm} \right) = \frac{10 \log \left(\frac{P_0}{P_1} \right)}{L_f} \quad (4.5)$$

where P_0 was the received power in mW at the initial length and P_1 was the received power in mW at the final length (after length of L_f in cm). Figure 4.18 shows the insertion loss cut back measurements for the flat fiber sample at a wavelength of 1550 nm. The insertion loss, IL (in dB) is defined as $IL \text{ (dB)} = P_0 \text{ (dBm)} - P_1 \text{ (dBm)}$.

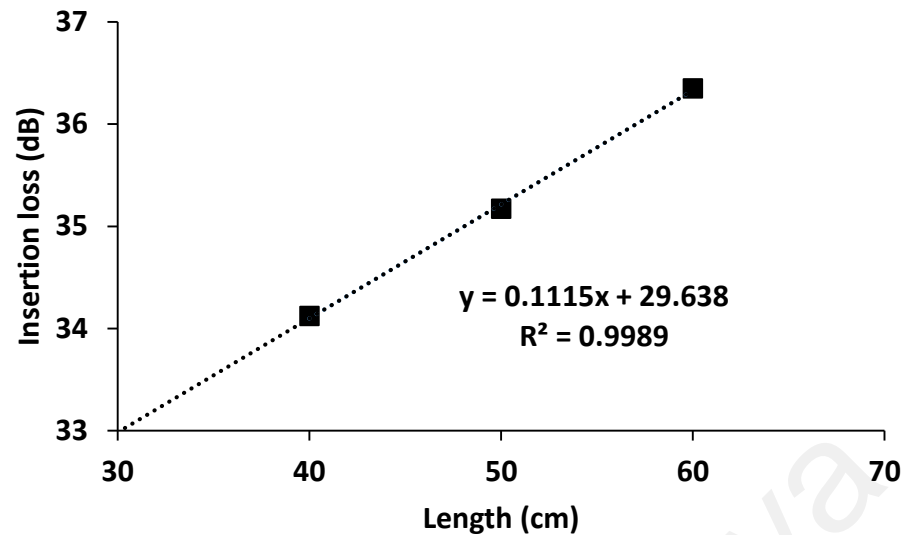
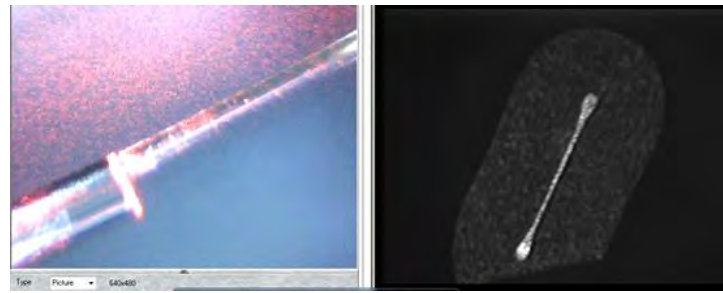


Figure 4.18: Insertion loss measurements at 1550 nm.

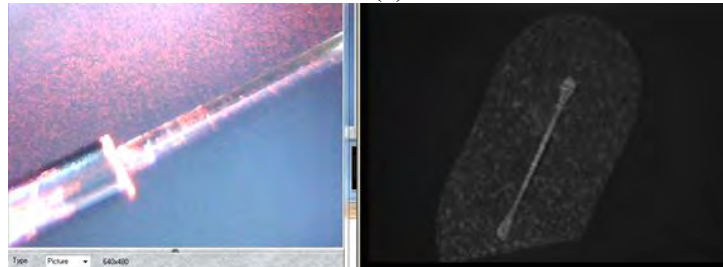
The linear model of the measurement in Figure 4.18 was done to obtain the attenuation loss and coupling loss. From Figure 4.18, the average attenuation loss in the flat fiber sample was measured as 0.11 dB/cm at 1550 nm and the coupling loss was estimated as 29.64 dB. The coupling loss was due to the alignment losses, Fresnel losses and NA mismatch of single mode fiber from laser source pigtail to flat fiber sample (launched in the middle).

4.5.2 Near field intensity distribution patterns

The modal properties of the flat fiber were determined from the near field patterns measurement. Figure 4.19 shows the near field patterns at 635 nm. The mode patterns can be slightly seen, although the number of modes cannot be determined accurately. Figure 4.20 shows the near field patterns at 1310 nm where the brightest spot on the fiber core moved from one end to the other end when the SMF fiber launching conditions changed. When the SMF fiber was launched at the right side of the flat fiber, the brightest spot on the mode pattern was also at the right side of the flat fiber and vice versa. If the SMF fiber was launched at the middle of the flat fiber, the mode patterns were equally bright.

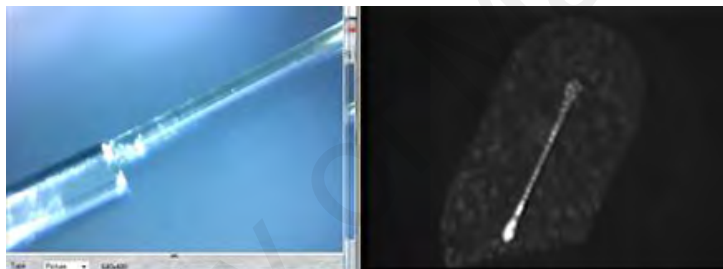


(a)

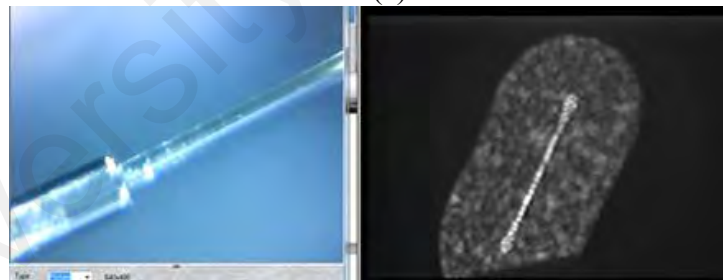


(b)

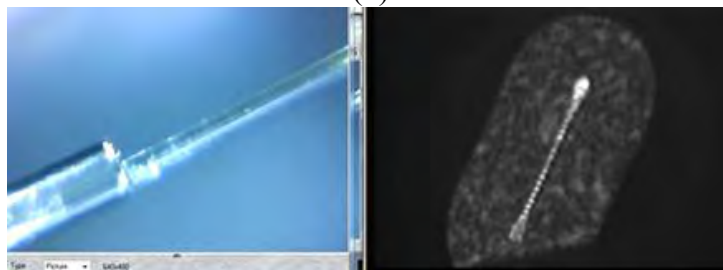
Figure 4.19: 60 cm flat fiber at 635 nm under 2 launching conditions (left (a) and middle (b)).



(a)



(b)



(c)

Figure 4.20: 60 cm flat fiber at 1310 nm under 3 launching conditions (left (a), middle (b) and right (c)).

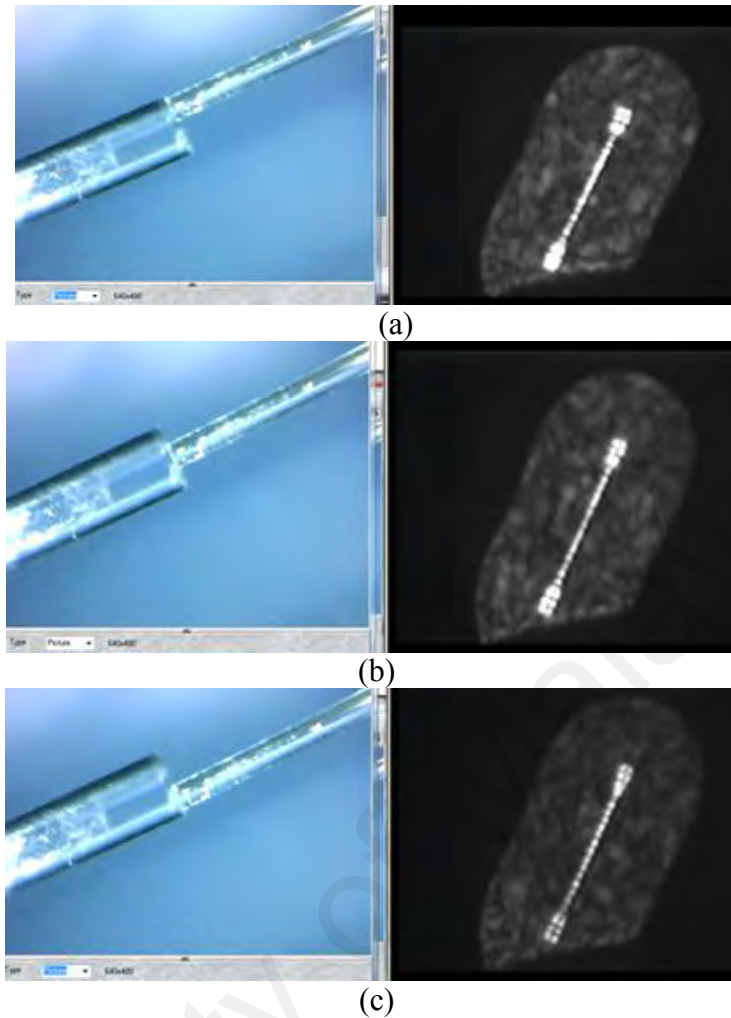


Figure 4.21: 60 cm flat fiber at 1550 nm under 3 launching condition (right (a), middle (b) and left (c)).

Figure 4.21 shows the near field patterns at 1550 nm. Similar to the wavelength at 1310 nm, despite different launching conditions, light was guided throughout the core and the sides of the core but with different intensity depending on the launching condition. In addition, only multimode propagation was observed in the flat fiber core and at the sides of the core.

4.5.3 Theoretical framework

A review of the modal analysis of flat fibers can be found in Appendix B. Simulation was performed using the RF module (mode analysis) in the commercial COMSOL Multiphysics software to observe the intensity distribution and mode profile patterns on

the core of the flat fiber for different wavelengths. The captured SEM image (Figure 4.16) was vectorised and imported into COMSOL.

The flat fiber sample had a cladding layer that was fused silica and a core doped with GeO₂ concentration of 3.63 (\pm 0.35) mol% measured using EDX. The initial GeO₂ concentration for the preform was approximately 5.78 mol%. The fiber drawing process had caused the dopant concentration to be reduced by about 37%. The refractive index for the GeO₂ doped core layer can be estimated by using a generalized formula (based on Sellmeier equation) defined as:

$$n_{core}(\lambda) = n_{silica}(\lambda) + d(1.4145 \times 10^{-3}) \quad (4.6)$$

where d is the dopant concentration in mol%.

The refractive index of the fused silica cladding based on Sellmeier equation (Agrawal, 1995) was calculated to be 1.457, 1.447 and 1.444 at 635 nm, 1310 nm and 1550 nm respectively. The refractive index difference was 0.35%.

Table 4.7: Core and cladding refractive index of the flat fiber

Wavelength (nm)	Core index	Cladding index
635	1.4621	1.4570
1310	1.4519	1.4468
1550	1.4497	1.4446

Table 4.7 shows the calculated core and cladding refractive indices of the flat fiber. The modal cutoff condition in the flat fiber is determined by assuming the following equation for the normalized frequency (Dyott, 1995),

$$V = \frac{2\pi \sqrt{\frac{tw}{\pi}}}{\lambda_0} \sqrt{n_1^2 - n_2^2} \quad (4.7)$$

where t is the thickness of the flat fiber, w is the width of the flat fiber, λ_0 is the free space wavelength, n_1 is the core refractive index and n_2 is the cladding refractive index. Using the core dimensions stated in Section 4.5, Equation 4.7 and the normalized frequency for planar waveguides which is equal to 1.571, the cutoff wavelength was calculated as 7.53 μm . The modal profiles were obtained at all three wavelengths.

Figure 4.22 shows the intensity mode profiles obtained using COMSOL which shows the mode order at 635 nm, 1310 nm and 1550 nm. For the 1st order mode, the distribution and number of lobes was similar for all wavelengths. For the 5th order mode, the number of lobes was similar for all wavelengths, but as the wavelength increases, the intensity distribution of the mode profile moves towards the sides of the flat fiber core. For the higher order modes (more than 10 modes), the number of lobes (mode order) increased as the wavelength increased, from 11 (at 635 nm) and 13 (at 1310 nm) to 15 (at 1550 nm). More electric fields penetrate into the cladding at longer wavelengths. At the 1st order, 5th order and higher order modes for 635 nm, the mode patterns are more confined to the core of the flat fiber and there was less electric field leakage into the cladding. At 1550 nm for the 1st order, 5th order and 15th order modes, the modal profiles show that there was more leakage in the cladding.

4.5.4 Discussion on characterization results

Experimental procedure was performed in the previous section to observe the near field patterns of the flat fiber under different launching conditions at the wavelengths of 635 nm, 1310 nm and 1550 nm. Despite different launching conditions, light was guided throughout the core with different intensity depending on the launching condition. In addition, only multimode propagation was observed in the flat fiber core. The near field patterns show that at 1310 nm, the brightest spot moved from one end to the other end based accordingly on the positions of the launching conditions. Individual intensity

profile spot cannot be selectively excited during experiment due to mismatch in the geometry of the single mode fiber and flat fiber.

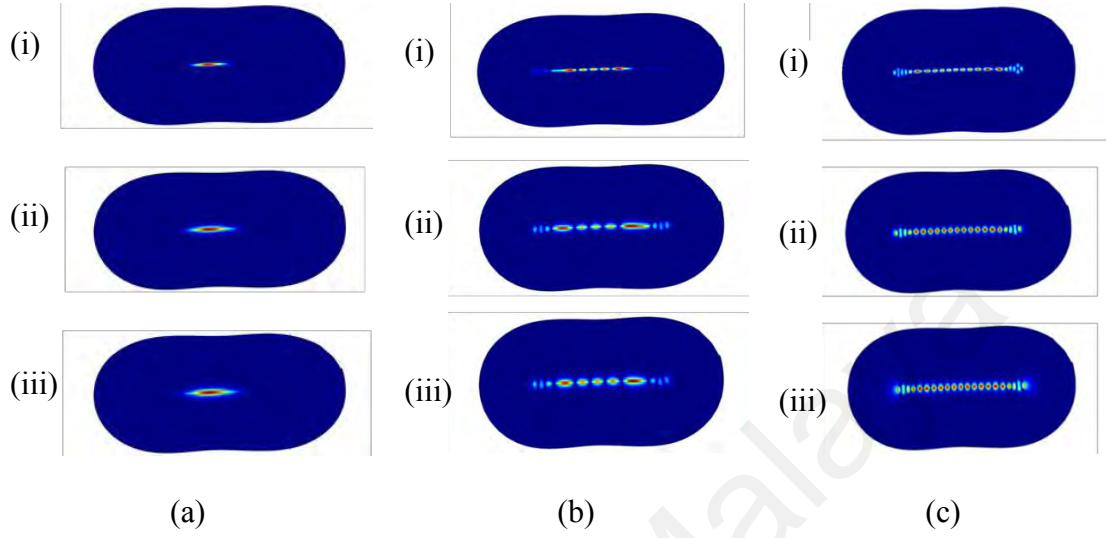


Figure 4.22: (a) Modal profile for 1st order mode at (i) 635 nm, (ii) 1310 nm (iii) 1550 nm. (b) Modal profile for 5th order mode at (i) 635 nm, (ii) 1310 nm (iii) 1550 nm. (c) Modal profile for higher order modes at (i) 635 nm, (ii) 1310 nm and (iii) 1550 nm.

The modal profile for the 1st order mode, 5th order mode and higher order modes were simulated numerically at the wavelengths of 635 nm, 1310 nm and 1550 nm. The modal profile shows that higher electric field penetrated into the cladding at 1550 nm. The simulated higher order mode profiles at 1310 nm and 1550 nm were almost similar to the near field intensity patterns observed experimentally. The experimental results confirmed that the doped flat fiber samples fabricated supported multimode propagation. Single mode propagation cannot be obtained due to the mismatch in core geometry of the SMF and flat fiber and the fixed NA of the SMF. In addition, the core thickness of the flat fiber was not optimized for single mode propagation where the cutoff wavelength was calculated as 7.53 μm using the flat fiber's core thickness. Due to the free space coupling between the SMF pigtail and the flat fiber, the high coupling loss further contributed to the loss in the fiber.

4.6 Fabrication of Multidopant Flat Fiber

In this section, multidopant flat fibers were fabricated and characterized using dual stage drawing. Two preforms were obtained commercially and were co-doped with 15 mol% GeO_2 and 10 mol% B_2O_3 . The thickness of the first preform tube was 1.85 mm (considered a thin preform) with an outer diameter of 26.50 mm and an inner diameter of 22.80 mm. The thickness of the second preform tube was 1.825 mm (considered a thin preform) with an outer diameter of 26.75 mm and an inner diameter of 23.10 mm.

Dual stage drawing was chosen for better control of the flat fiber dimension as it was anticipated that it will be a challenging fabrication process to fabricate a thin preform with two dopants based on fabrication results obtained previously. The preform was first drawn to a target capillary size without applying any vacuum pressure to the preform. Once the capillary size was obtained, the vacuum pressure was immediately applied to flatten it to a flat fiber rod size. Results from Chapter 3 show that at a furnace temperature of 2100 °C and a vacuum pressure of 1.5 kPa, a pure silica preform (with thin preform) can be flattened to a thickness of 1 mm. Considering that this preform has a thickness of 1.85 mm and was doped with both GeO_2 and B_2O_3 , the furnace temperature was initially set as 2100 °C for the initial condition. In Chapter 3, it can be seen that the thin preform was more sensitive to change in the furnace temperature. The plan was to first draw the preform into a flat fiber rod with a width of 3 mm (first stage drawing), so the initial vacuum pressure was set as 2 kPa. Table 4.8 shows the initial drawing conditions.

Table 4.8: Initial drawing conditions.

Proposed rod for first stage drawing (mm)	3.0
Furnace temperature (°C)	2100
Feed speed (mm/min)	9.0
Draw speed (m/min)	0.7
Vacuum pressure (kPa)	2.0

A vacuum of 2 kPa was applied immediately after the fiber drop with the initial temperature set at 2100 °C. Due to non-optimized drawing conditions, measurements of the x and y dimensions were not accurate and were not taken. At the temperature of 2090 °C for vacuum pressure of 1 up to 3 kPa, the thin preform was observed to fully collapsed (except for some small interstitial holes) and formed a deformed shape as shown in Figure 4.23 (a). When the temperature was slowly lowered to 1950 °C, capillary was obtained when the vacuum pressure applied was 3 and 4 kPa.

As expected from the investigation done in Chapter 3, a preform with a thin wall thickness (1.85 mm) can easily be collapsed to a solid fiber. This was due to the small temperature difference between the preform outer layer and inner layer of the hollow preform. Therefore, adding extra upwards force from the suction of the vacuum pump could easily deform the flat fiber. In addition, the deformed shape obtained could also be due to the surface tension effects as previously discussed in Chapter 3 (Fitt *et al.*, 2002, Xue *et al.*, 2006 & Voyce *et al.*, 2009). Figure 4.23 (b) shows two large air holes at both sides of the flat fiber. This shape was observed at low vacuum pressure and low temperature.

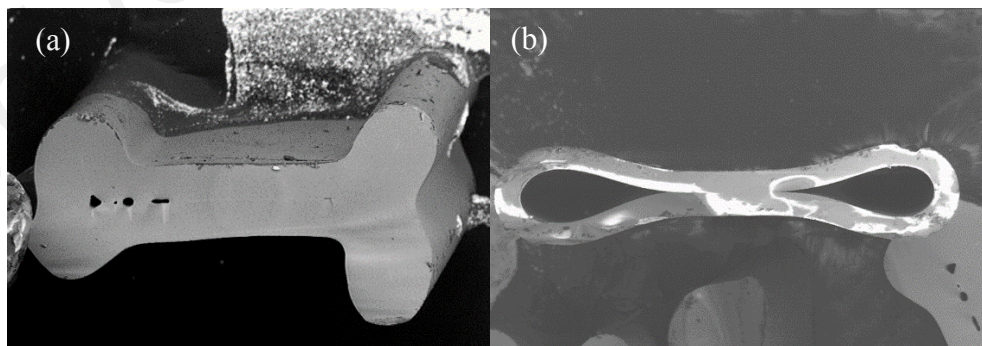


Figure 4.23: (a) Deformed flat fiber rod obtained at a furnace temperature of 2100 °C and 2 kPa vacuum pressure (b) Large airholes at the sides of the flat fiber rod.

Due to difficulties in controlling the flat fiber shape, capillaries at a diameter of 1 mm, 2.4 mm and 2.55 mm were collected at a temperature of 2100 °C. Vacuum pressure was

applied during the second stage drawing method to flatten the capillaries. In addition to capillaries, flat fiber rods are also collected. A sample of the collected flat fiber rod measured using FESEM had an approximate dimension of 2.86 mm x 0.445 mm and a core dimension of 2.43 mm x 2.81 μm . For the dual stage drawing of the flat fiber rod, the initial feeding rate was 8 mm/min and the draw speed were 1 m/min using flat fiber rod. The temperature was set at 2020 $^{\circ}\text{C}$ and later the draw conditions were changed to a draw speed of 0.7 m/min and a feed rate of 13.13 mm/min. The draw tension was observed to be 34 - 39 g.

Figure 4.24 shows a sample of the flat fiber rod measured using FESEM which has a dimension of 332 μm x 36 μm (core dimension 254 μm x 0.55 μm). From the image, small air holes measuring about 15 μm were found at the sides of the core layer which formed during the collapse process.

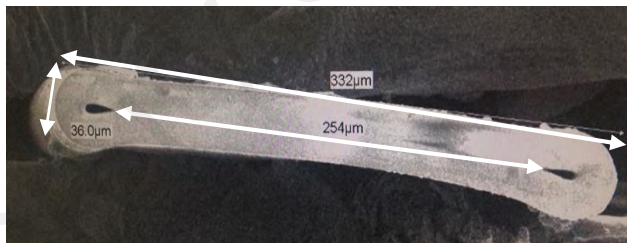


Figure 4.24: Flat fiber sample.

Due to the thin core thickness obtained (core thickness of less than 3 μm for both the flat fiber rod and flat fiber), it was a concern whether the GeO_2 and B_2O_3 content in the core had diffused. If the GeO_2 and B_2O_3 content had diffused, this would affect the refractive index of the fiber and in the worst case, there would be no core in the flat fiber. Thus, FESEM EDX analysis was performed on the samples with the initial objective of measuring the Germanium (Ge) and Boron (B) concentration.

FESEM EDX was done on a few samples of the capillary, flat fiber rod and flat fiber to measure the Ge and B concentration in the samples. From this measurement, the

refractive index for both the core and cladding can be determined. This value can be used to estimate the numerical aperture of the fiber. The FESEM EDX measurement was repeated for a few samples and done using two different types of EDX equipment (Institute of Postgraduate Studies, University of Malaya and Faculty of Physics, University of Malaya). The EDX measurements setting include only five relevant elements which were Ge, B, Silicon, Oxygen and Chlorine. These were the elements that were expected in the flat fiber core.

The capillary samples measured had Germanium concentration of 5.9% and 8.5% (in Wt%). The EDX results show that there was a very low concentration of Germanium on the flat fiber rod (0.51% in Wt%) and flat fiber samples (0.12% in Wt%). Boron was not detected at all. This could be due to the fact that GeO_2 and B_2O_3 had diffused during the fiber drawing process. Dopant diffusion may occur during the fiber drawing process due to high furnace temperature and low draw speed (Lyytikainen, 2004). Dopant diffusion also caused the original dopant distribution in the preform to change (Lyytikainen, 2004). Besides that, the concentration of these elements was low and very close to the EDX detector detection limit. The FESEM EDX measurement was repeated on a few different samples and the same results was obtained. Due to this, the refractive index of the thin core flat fiber could not be estimated and the analysis on the light propagation in the thin core flat fiber could not be performed.

4.7 Summary

In this chapter, the control of flat fiber dimensions was investigated by studying the drawing process of doped flat fibers. It was found that a high concentration of GeO_2 preform tube produced flat fibers with a thick core and unwanted airhole in the center of the core. Applying more vacuum had no effect on further collapsing the airhole due to the diffused cladding. Adding dopant into the pure silica preform decreased its viscosity and

a higher temperature was required for its melting temperature. Thus, for the drawing of doped flat fibers, optimum furnace temperature was required to ensure the desired flat fiber dimension was achieved. Drawing parameters such as furnace temperature and vacuum pressure, are also a function of the preform material itself. Thus, knowledge of the preform material also influence the final flat fiber dimension.

Although dual stage drawing method has been used in the fabrication of photonic crystal fibers, this method has never been reported in flat fiber fabrication. Experimental results show that using single stage drawing, it was easier to control the dimension of a 1.25 mm capillary compared to a 125 μm capillary. Hence, dual stage drawing for flat fibers were proposed to overcome the difficulties in drawing to a smaller desired diameter. Using dual stage drawing, the fabrication of flat fibers from flat fiber rods were also discussed. Basic characterization was performed on the doped flat fiber samples. The near field intensity profiles were obtained at wavelengths of 635 nm, 1310 nm and 1550 nm and the profiles showed multimode propagation in flat fibers. Thus, to achieve single mode propagation, suitable preform core was required.

For flat fibers with a thin preform tube and doped with both GeO_2 and B_2O_3 , the fabrication process was a challenge and flat fibers produced were deformed. Moreover, dopant diffusion occurred in the core as the thin core had very low concentration of germanium and boron. In summary, it was difficult to control the flat fiber dimensions using a thin-walled preform with multi-dopants.

In the next chapter, novel multistructured flat fibers will be proposed and fabricated.

CHAPTER 5: NOVEL MULTISTRUCTURED FLAT FIBERS

5.1 Introduction

Based on the fabrication knowledge obtained in Chapters 3 and 4, novel design of multistructured flat fiber will be proposed and fabricated in this chapter. These multistructured flat fibers can be used as functional optical devices, without the need for additional technology related to planar waveguide technology. The fabrication process of these multistructured flat fibers will be discussed and its drawing conditions will be characterized. A novel and improved fabrication technique to fabricate multistructured flat fibers will also be discussed in this chapter.

5.2 Fabrication of Multicapillary Flat Fiber

There is a growing interest to incorporate non-solid materials such as liquids, gases and plasma gases into functional parts in photonic devices and systems (Schmidt & Hawkins, 2011). This is the backbone for optical sensing (Schartner *et al.*, 2015), where optical devices can be used to detect many types of non-solid materials for diverse applications in healthcare, industrial, communication and others. Specialty optical fibers such as photonic crystal fibers and microstructured optical fibers consist of air voids that can be filled with different kinds of microfluidics (Monat *et al.*, 2007). Fluid-light interaction can modify the optical properties of the device, creating an optical device such as tunable optical filter, which have been demonstrated using microstructured fiber with a core index grating surrounded by six holes surrounded by fluids (Mach *et al.*, 2002). In this device, optical filtering is done via selectively coupling the light mode between core and the cladding layer utilizing a fluid with high refractive index. Fluids can also form adaptive Bragg gratings for tunable optical filtering (Kerbage & Eggleton, 2003). Side hole fibers (fibers with two side holes) can also potentially be used in nonlinear fibers and fiber sensing devices where the holes can be filled with materials such as metals, alloys, gases and liquids (S. H. Lee *et al.*, 2015).

In this section, a multicapillary flat fiber was proposed. The multicapillary flat fiber has a row of air holes across the lateral dimension of the flat fiber. One of the main motivations for these air holes is to store non-solid materials such as liquids and gases. This could potentially be used later to develop microfluidic channels, biosensors (Erickson *et al.*, 2008) and lab-on-a-chip sensors and devices.

There were a few initial experimental trials done by members of the Integrated Lightwave Research Group, Faculty of Engineering, University of Malaya to fabricate the multicapillary flat fiber. In the first experimental trial, 8 capillaries (1 mm in diameter) were inserted into a preform with an outer diameter of 24.15 mm. The capillaries hang freely and loosely in the preform, which meant they were not fixed together and not fixed to the preform. The length of the preform and capillaries were nearly similar. The feed rate was fixed at 0.06 mm/min and the draw speed was 0.38 m/min. The furnace temperature was set at 2025 °C. As the drawing process stabilized, the vacuum pressure was increased from 0 kPa to 1 kPa and 1.1 kPa. The microscope images in Figure 5.1 show that when the vacuum pressure was increased, the inner capillaries were randomly distributed on the fiber and not aligned in a straight line as expected. A few capillaries were also collapsed and combined with one another. As the draw speed was increased to 1.12 m/min and the feed rate was increased to 0.16 mm/min (with vacuum pressure of 1.1 kPa and the furnace temperature remaining the same), the fiber became fragile and break easily. It can be seen from this trial that there was a need to fix the inner capillaries together as the vacuum pressure may cause the inner capillaries to sway freely during the drawing process. Besides that, the vacuum pressure also needs to be increased in order to flatten the fiber.

In the next experimental trial, 6 capillaries (1 mm in diameter) were inserted into a preform with an outer diameter of 24.3 mm. The capillaries were fixed together at the top

and bottom using a custom made holder. The feed rate was fixed at 0.06 mm/min and the draw speed was 0.3 m/min. The furnace temperature was set at 2025 °C. As the drawing process stabilized, the vacuum pressure was increased from 0 kPa to 2.5 kPa. The microscope images in Figure 5.2 shows the capillary fabricated with the inner capillaries as the vacuum pressure increased from 1.5 to 2.5 kPa. As shown, the inner capillaries were also collapsed, which was not seen previously which was suspected from the leaking of seal at the vacuum mount.

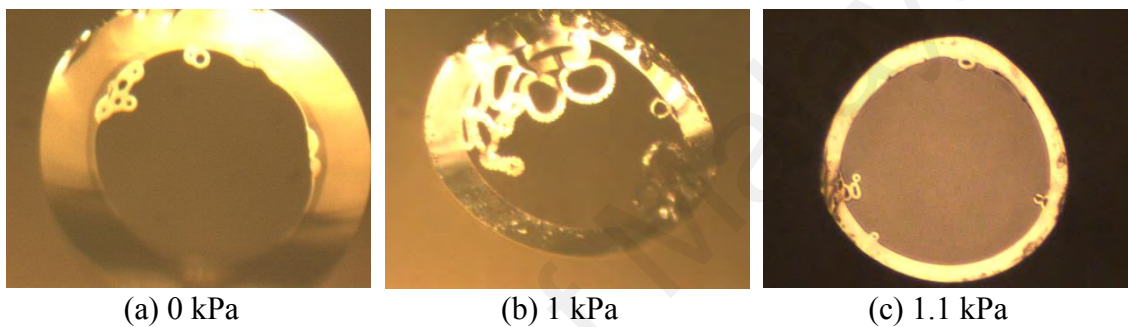


Figure 5.1: Microscope images of the capillary fabricated.

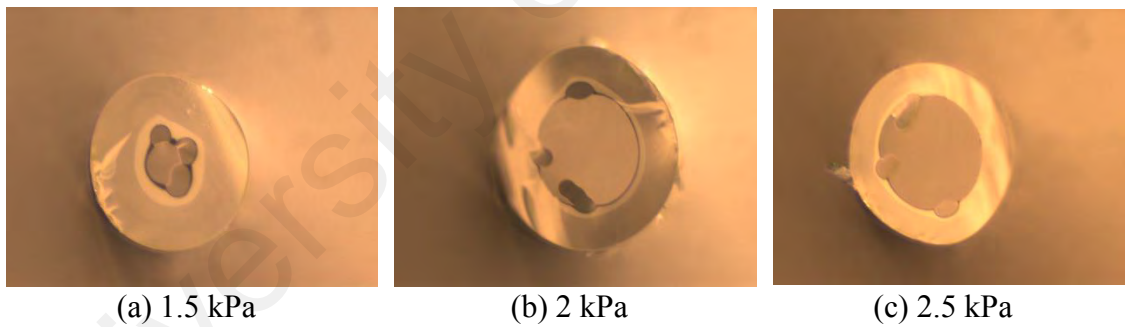


Figure 5.2: Microscope images of the capillary fabricated.

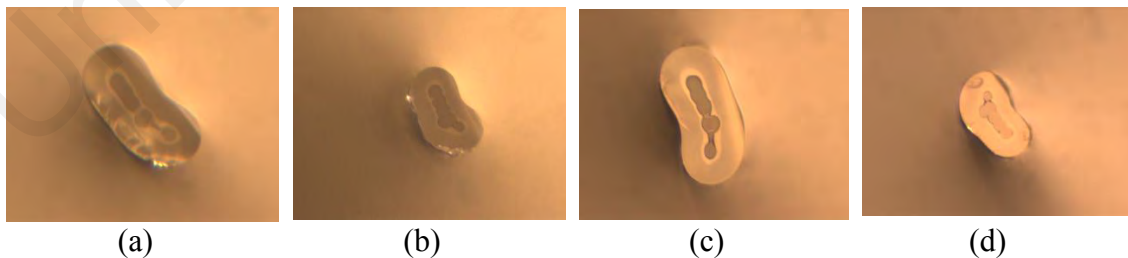


Figure 5.3: Microscope images of the capillary fabricated at vacuum of 25 kPa at various feed rate and draw speed setting.

Figure 5.3 shows the flat fiber fabricated as the vacuum pressure was increased to 25 kPa. The flat fiber shape was partially obtained but the capillaries were collapsed. During

the fabrication process, the draw speed and feed speed were varied to see the effect on the inner capillaries. The values were shown in Table 5.1.

Table 5.1: Effect of drawing conditions on the multicapillary flat fiber.

Figure	Feed speed (mm/min)	Draw speed (m/min)	Observation
5.3 (a)	0.08	0.40	<ul style="list-style-type: none"> • All inner capillaries collapsed. • Middle capillary was not aligned in straight line and indicated that slight movement in the inner capillary's positions had occurred. • Slight deformed shape at the center of the flat fiber.
5.3 (b)	0.08	0.21	
5.3 (c)	0.32	0.21	
5.3 (d)	0.40	0.03	

Two methods had been proposed to overcome the problems faced in the initial fabrication process of the multicapillary flat fiber. The first was the dual stage fabrication process as described in Chapter 4 and the second was a custom designed mount. Both these methods have been filed and patented in Malaysia by the Integrated Lightwave Research Group, Faculty of Engineering, University of Malaya (Grant No: MY-163092-A and MY-163093-A).

Using the two methods proposed, preliminary geometrical characterization was performed to verify the experiment procedure (as a proof of process) was successful to produce a multicapillary flat fiber. In this trial, pure silica Suprasil F300 preform tubes were used. For the fabrication of the multicapillary flat fiber, firstly a short length capillary about 25 cm in length were carefully tied together (by melting) forming a row of capillary. Each capillary had an outer diameter of 1 mm. The row of capillaries was then inserted inside the preform tube before the first stage of the fiber drawing. The row of capillaries was hold together using a custom made holder and the top ends of each

capillary was sealed using flame. The capillaries were sealed to ensure that the vacuum pressure used to collapse the flat fiber's preform does not affect the capillaries. The draw speed, feed speed and drawing temperature were controlled to ensure that the specified final dimension of the multicapillary flat fiber was achieved. The first stage of the fabrication produced a flat fiber rod, with a width of about 3 mm. In the second stage of fabrication, the dimension of the multicapillary flat fiber was $300\text{ }\mu\text{m} \times 120\text{ }\mu\text{m}$ and the diameter of the airholes were approximately $20\text{ }\mu\text{m}$.

The main difficulty in developing the multicapillary flat fiber was the ability to control the hole deformations. During multiple experimental runs done in the Flat Fiber Lab, University of Malaya, Malaysia, the deformations of inner capillary can occur during the drawing process which caused a total collapse of the capillary, changes in the dimension and the shape of the capillary and movement of the capillary. The deformations occur due to a number of reasons including non-optimised capillary number with relative to the size of the preform and desired multicapillary flat fiber diameter (Xue *et al.*, 2006), non-optimised draw speed and feed speed, high pressure inside the capillaries and the capillaries break inside the preform during drawing processes.

Figure 5.4 (a) shows the cross section of a multicapillary flat fiber (with light guidance) with capillaries that are not collapsed, changed shapes and aligned in multiple rows and Figure 5.4 (b) shows the cross section of a multicapillary flat fiber (with light guidance) with capillaries that are not collapsed and aligned perfectly in a single row.

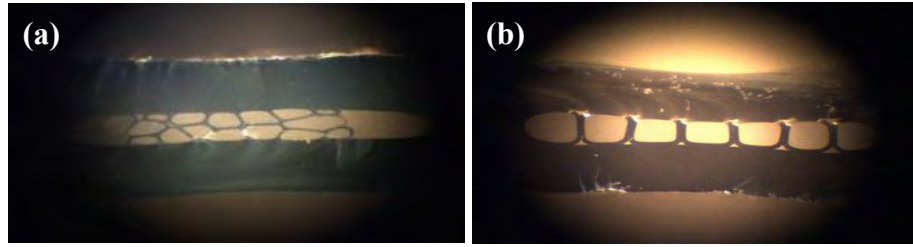


Figure 5.4: Cross section of multicapillary fiber with (a) multiple rows of holes (b) one row of holes.

The multicapillary flat fiber using only pure silica preform does not propagate the light in the holes but leaked into the cladding layer. This was because air has a smaller refractive index than silica glass and the physical dimension of the inner layer of the multicapillary flat fiber was not suitable to propagate the light with photonic bandgap effect. On its own, due to light not propagating in the air holes, further investigation was necessary to determine suitable applications for the multicapillary flat fiber. As a suggestion, for light to propagate in the holes of the multicapillary flat fiber, it needs to be filled with materials with a higher refractive index than silica glass or the preform needs to be doped. Different design of the air hole structure in the multicapillary flat fiber can also be explored to see if it can produce optical bandgap effect. Further investigation on the optical and waveguiding properties of the multicapillary flat fiber is currently ongoing to explore the potential of developing waveguide devices, grating devices and optically active devices using the multicapillary flat fiber.

5.3 Fabrication of Multicore Flat Fiber

Nowadays, most long haul and short haul telecommunication networks are implemented using optical fiber communication systems. However, the bandwidth of conventional optical fibers is not infinite and more bandwidth is needed to support the current and future services offered by the Internet. New generation optical fibers, such as multicore fibers, are needed to improve the bandwidth capacity. In recent years, the transmission capacity of multicore fibers has been rapidly increasing. In 2010, a 70 Gb/s

transmission using a single 550 m multicore fiber has been reported (Zhu *et al.*, 2010), thus demonstrating high speed transmission using a multicore fiber with 7 cores arranged in a hexagonal array. In 2012, a 12 core multicore fiber has also been demonstrated with a transmission speed of 1.01 Pb/s (Takara *et al.*, 2012). In 2018, a 6 mode, 19 core multicore fiber has been demonstrated to provide a fiber transmission capacity of 10.16 Pb/s (Soma *et al.*, 2018).

Fabrication of a single mode 7 core fiber can be done using the stack-and-draw procedure (Samir *et al.*, 2016). A rectangular fiber with multiple cores fabricated using outside vapor deposition has also been demonstrated (S. Huang *et al.*, 2017).

Multicore flat fibers have a structure that is similar to the multicapillary flat fiber discussed in Section 5.2, except that the single row of air holes is replaced with a single row of single mode fibers. Due to its structure and core arrangement, multicore flat fibers can be used for optical applications which has closely packed arrays of transmitters and receivers. Multicore flat fibers with 6 cores (Mahdiraji *et al.*, 2014) have been successfully fabricated using novel suspend-array drawing by the Integrated Lightwave Research Group, Faculty of Engineering, University of Malaya. For the preform preparation, the preform which contains 6 step index glass rods were arranged in a linear array and fused together at a few locations using a hand torch. The fusing was done using silica bridges. The glass rods hang over a 'hanging rail' which was connected to the extended part of the vacuum mount. using a hand torch. The fusing was done using silica bridges. The glass rods hang over a 'hanging rail' which was connected to the extended part of the vacuum mount. Then, the preform was drawn to a circular/elliptical rod size at a draw speed of 0.5 m/min, furnace temperature of 2100 °C and vacuum pressure of 5 kPa. The rod size was approximately 4.62 mm x 1.59 mm. The rod was then redrawn to the desired multicore flat fiber size by setting the furnace temperature at 1990 °C, preform

feed rate of 31.2 mm/min, draw speed of 2 m/min and fiber tension of 40 ± 10 gm. There were some interstitial holes between the cores in the flat fiber and a higher vacuum pressure was applied to close the holes. Polymer coating was then applied by using a circular-hole die with a hole diameter of $800 \mu\text{m}$. Figure 5.6 shows the cross section image of the 6 core multicore flat fiber (Mahdiraji *et al.*, 2014).

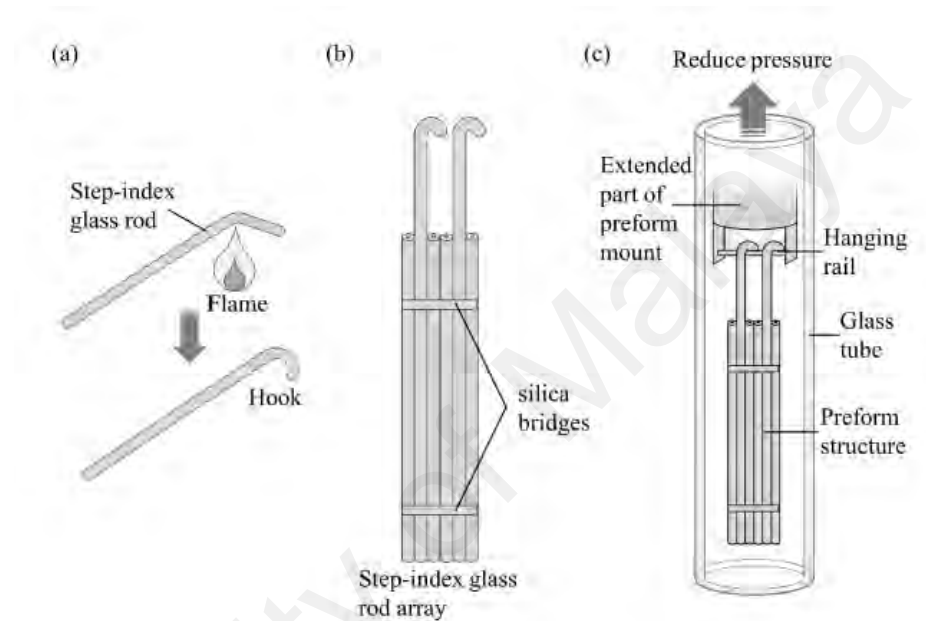


Figure 5.5: (a) Preparation of step index rods with hooks (b) Fusing of glass rods using silica bridges (c) Preform arrangement inside the mount (Reproduced from Mahdiraji *et al.*, 2014 with permission).

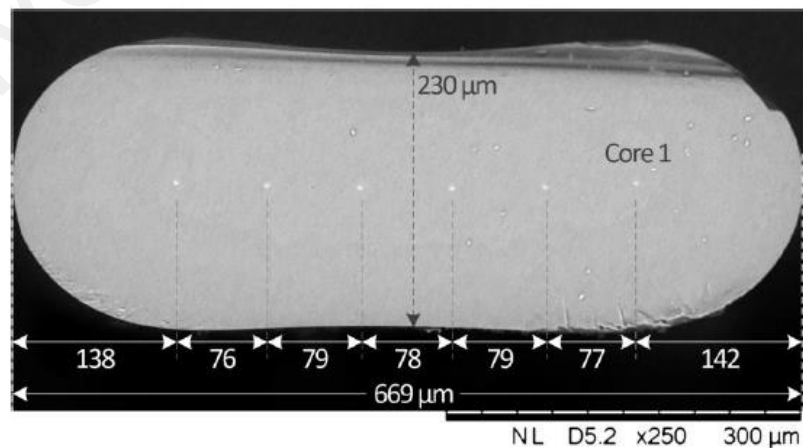


Figure 5.6: Cross section of the 6 core multicore flat fiber (Reproduced from Mahdiraji *et al.*, 2014 with permission).

For the 6 core multicore flat fiber, the signal crosstalk between adjacent cores was found to be less than -74 dB and can tolerate a bending diameter of 2 cm (with polymer coating) (Mahdiraji *et al.*, 2014). The fabricated multicore flat fibers can potentially be used for high speed transmission in long haul communication systems. In addition, the fabrication of the multicore flat fiber was flexible, simple and can be done rapidly.

5.4 Fabrication of Doped Flat Fiber with Airholes

In the previous sections, two types of multistructured flat fiber, which were multicapillary flat fiber and multicore flat fiber were discussed. Multicapillary flat fiber were fabricated using pure silica preforms, thus it cannot propagate light in the air holes and further investigation is ongoing to determine its potential applications in sensors and communications. At the same time, multicore flat fiber, fabricated using just an optical drawing tower, can potentially be used for long haul optical fiber communications.

A new multistructured flat fiber was developed in this thesis in order to solve the issue with multicapillary flat fiber which cannot propagate light in the airholes. In this initial design, an airhole was produced into a doped flat fiber. This will ensure the light to propagate in the core of the flat fiber and the airhole in the flat fiber could be used as an optical sensor for material sensing with different refractive index. Figure 5.7 shows a schematic of the doped flat fiber design with a single airhole.

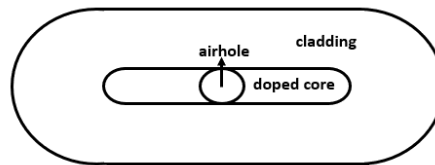


Figure 5.7: Single airhole and doped core.

Three parameters which was discussed below will be investigated using COMSOL simulation to design a doped flat fiber with airholes which allow single mode light propagation. With single mode propagation, light was confined to the core of the flat fiber

and allow less coupling loss when coupling or splicing with other single mode optical fibers.

The parameters that were investigated and optimized were:

- (i) Core geometry (thickness of the core) – For this part, the thickness and width of the core were first determined for single mode propagation based on planar waveguide's cutoff V parameter. The parameters were then varied based on the refractive index of the core and cladding of the flat fiber.
- (ii) Refractive index of the core and cladding. This was varied based on the dopant concentration used in the core of the flat fiber. For this design, the dopant's material was assumed to be GeO_2 and the cladding was pure silica glass. GeO_2 was a common dopant used to increase the refractive index of the core and literature on this dopant had been discussed in Chapter 4, Section 4.3.
- (iii) Wavelength of light propagating in the flat fiber.
- (iv) Number of airholes in the core. This will also affect the core geometry of the flat fiber.

Once an optimum design was achieved, the fabrication process will be attempted. However, the fabrication process will only be a proof of concept due to limited preforms availability.

5.4.1 Simulation results

Similar to optical fibers and planar waveguides, light propagation in flat fibers depend largely on their core geometry. The analysis began by using the design shown in Figure 5.7, which had a single airhole positioned in the middle of the flat fiber core. Using COMSOL simulation to observe the modal profile, the core geometry (core thickness) was varied for a flat fiber with a single airhole to observe its mode profiles.

The main outcome of the simulation was to decide a core thickness that allows single mode propagation in each side adjacent to the airhole. To start the design process, an initial flat fiber dimension of 300 μm x 200 μm was chosen. The wavelength was fixed at 1550 nm. The cladding refractive index was fixed at 1.4440 which was the refractive index for fused silica at 1550 nm. The core was initially assumed to be doped with GeO_2 so the values for the refractive index was dependent on the concentration of the dopant (defined as d) and calculated using Equation 4.6.

To begin the analysis on the effect of core thickness on flat fibers, the effect of core thickness on planar waveguide was studied. For a planar waveguide, the V number is defined as:

$$V = \frac{2\pi}{\lambda} t_c \sqrt{n_{core}^2 - n_{cladding}^2} \quad (5.1)$$

where t_c is the core thickness, λ is the wavelength of light, n_{core} is the core refractive index and $n_{cladding}$ is the cladding refractive index. To achieve single mode propagation in a planar waveguide, the V parameter should be less than or equal to $\frac{\pi}{2}$ or 1.5707. Thus, in the simulation, the thickness of the flat fiber was calculated using Equation 5.1 where V was taken as 1.5707 for single mode propagation. The preliminary simulation results which had single mode propagation on each side of the single airhole were shown in Table 5.2. The effective refractive index was recorded for when single mode profile was observed and the finding was tabulated in Table 5.2. The effective refractive index, n_{eff} is defined as:

$$n_{eff} = \frac{\beta}{k} \quad (5.2)$$

where β is the phase constant and k is defined as $\frac{2\pi}{\lambda}$ with λ as the wavelength in the medium. Based on the results from Table 5.2, the effect of dopant concentration on the core thickness of 13.60 μm and 19.20 μm was investigated as shown in Table 5.3. The two core thickness values were chosen as it can confine the light better. The dopant concentration in mol% was varied from 0.1 to 1.0 to observe the light confinement and single mode propagation obtained with different dopant concentration. The wavelength was still fixed at 1550 nm and the cladding refractive index was also fixed at 1.4440.

The COMSOL simulation results show that at a core thickness of 13.6 μm , single mode propagation only was obtained when the dopant concentration in mol% was 0.1 (effective refractive index 1.4440) and 0.2 (effective refractive index 1.4441). At a thickness of 19.2 μm , single mode propagation only was obtained when the dopant concentration in mol% was 0.1 (effective refractive index 1.4440). Multiple modes were seen in the modal profile as the dopant concentration in mol% was increased. As the dopant concentration in mol% was increased to 1 at a thickness of 13.6 μm , up to a maximum of 5 modes in the modal profile could be seen at each side of the airhole for varying effective refractive index. Thus, to obtain single mode propagation at 1550 nm, the dopant concentration in mol% should be small, indicating that the NA for the flat fiber design should also be very small.

Table 5.2: Different core thickness at 1550 nm

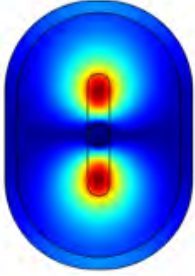
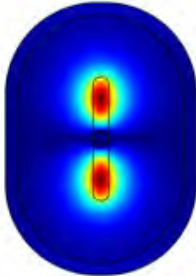
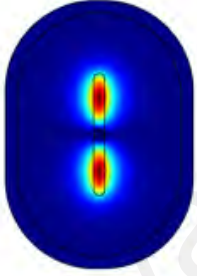
Core refractive index	Dopant concentration (mol%)	Effective refractive index	Core thickness (μm)	Airhole diameter (μm)	Modal Profile	Observation
1.4441	0.05	1.4440	27.10	27.10		Light was less confined to the core.
1.4442	0.1	1.4440	19.20	19.20		Light was less confined to the core.
1.4443	0.2	1.4441	13.60	13.60		Light was less confined to the core.

Table 5.3: Modal profile obtained at 1 mol% of GeO₂ doped core at a core of 13.6 μm

Effective refractive index	Modal profile
1.4450	<p>Figure 1: Modal profile for effective index 1.4450. The plot shows the surface electric field norm (V/m) for the $\text{dl}(2)=-2$ mode. The field is concentrated in two lobes along the horizontal axis, with a maximum value of approximately 1.2 $\times 10^4$ V/m. The axes range from -250 to 250 on the x-axis and -120 to 120 on the y-axis.</p>
1.4448	<p>Figure 2: Modal profile for effective index 1.4448. The plot shows the surface electric field norm (V/m) for the $\text{dl}(2)=-1$ mode. The field is concentrated in three lobes along the horizontal axis, with a maximum value of approximately 700 V/m. The axes range from -250 to 250 on the x-axis and -120 to 120 on the y-axis.</p>
1.4446	<p>Figure 3: Modal profile for effective index 1.4446. The plot shows the surface electric field norm (V/m) for the $\text{dl}(2)=-1$ mode. The field is concentrated in four lobes along the horizontal axis, with a maximum value of approximately 600 V/m. The axes range from -250 to 250 on the x-axis and -120 to 120 on the y-axis.</p>
1.4444	<p>Figure 4: Modal profile for effective index 1.4444. The plot shows the surface electric field norm (V/m) for the $\text{dl}(2)=-1$ mode. The field is concentrated in five lobes along the horizontal axis, with a maximum value of approximately 350 V/m. The axes range from -250 to 250 on the x-axis and -120 to 120 on the y-axis.</p>
1.4440	<p>Figure 5: Modal profile for effective index 1.4440. The plot shows the surface electric field norm (V/m) for the $\text{dl}(2)=-2$ mode. The field is concentrated in six lobes along the horizontal axis, with a maximum value of approximately 500 V/m. The axes range from -250 to 250 on the x-axis and -120 to 120 on the y-axis.</p>

Next, the wavelength was varied from 600 nm to 1700 nm for a core thickness of 13.6 μm and a GeO_2 concentration of 0.1 mol% to observe the modal profile. The core refractive index was 1.4442 and the cladding refractive index was 1.4440. The results showed that single mode profile at each side of the airhole was obtained at the wavelength range of 1200 nm to 1700 nm. At wavelength range of 800 nm to 1100 nm, two modes were seen at each side of the airhole and at 700 nm, three modes were seen at each side of the airhole. Four modes were seen at each side of the airhole at 600 nm.

The effect of varying the airhole diameter on the modal profile was also investigated at the wavelength of 1310 nm and a GeO_2 dopant concentration of 0.1 mol%. The core thickness was fixed at 13.6 μm . The airhole diameter was reduced by 25% for each subsequent airhole diameter which are 13.6 μm , 10.2 μm , 6.8 μm and 3.4 μm . The wavelength 1310 nm was chosen as it is a wavelength used for communication purposes and the previous simulation results show that at this wavelength, all light was confined in the core. It shows that the airhole diameter does not play a significant role in the modal profile simulated as the results were the same for all airhole diameters. The airhole acts as a barrier between the sides of the airhole and confine light accordingly.

Next, the number of airholes was increased to two airholes as seen in Figure 5.8 and the GeO_2 concentration was 0.1 mol%. The wavelength was varied from 600 nm to 1700 nm. The core thickness was set as 13.6 μm . Single mode propagation was obtained at the wavelength of 1200 nm – 1700 nm and there were no other modes propagating in the core of the flat fiber at these wavelengths. However, at higher wavelengths, the modal profile shows less confinement of the power intensity in the core and light field can be seen leaking into the cladding as seen in Figure 5.9 (b). Figure 5.10 shows the effective refractive index versus wavelength for the two airholes for single mode propagation. Using COMSOL, the desired number of modes searched was 100.

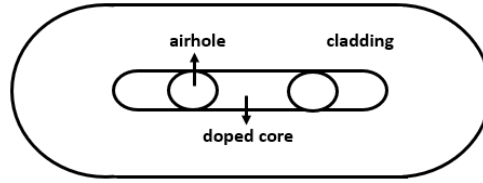


Figure 5.8: Two airholes in the core.

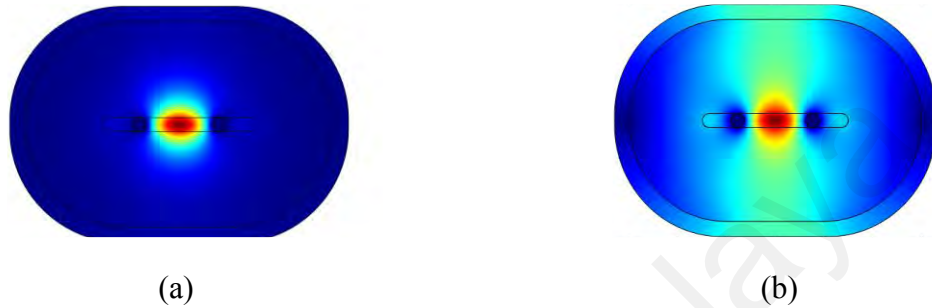


Figure 5.9: Single mode propagation in doped flat fiber with 2 airholes at wavelength of (a) 1310 nm and (b) 1700 nm.

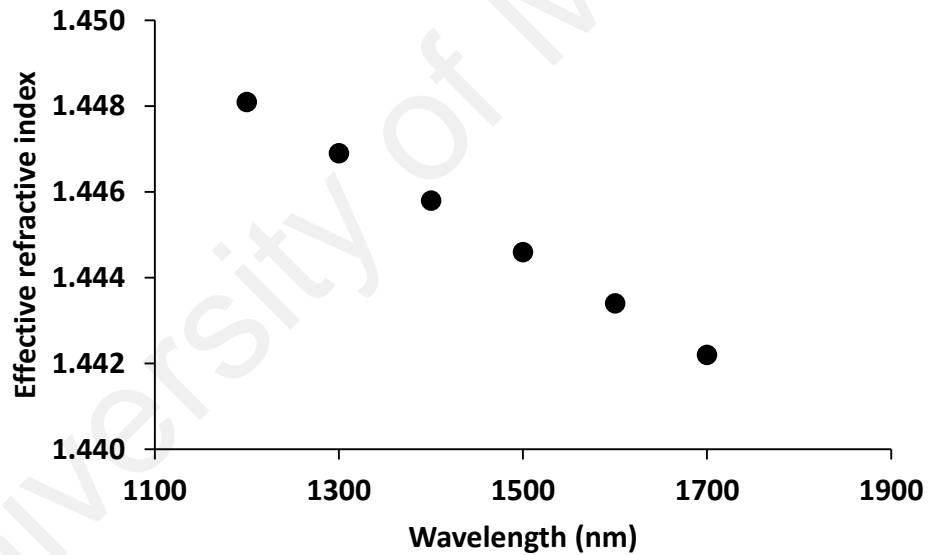


Figure 5.10: Effective refractive index versus wavelength for single mode modal profile observed.

Next, the number of airholes was increased to three airholes as seen in Figure 5.11. The wavelength was varied from 1200 nm to 1700 nm. The core thickness was 13.6 μm and the dopant concentration was 0.1 mol% of GeO_2 . The dopant concentration was varied from 0.5 to 5 mol%. Light was very confined to the core with the 3 airholes in the doped flat fiber at 5 mol% of GeO_2 . In addition, the mode was only excited at specific location in the core for different values of the effective refractive index.

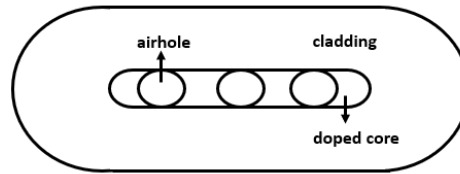
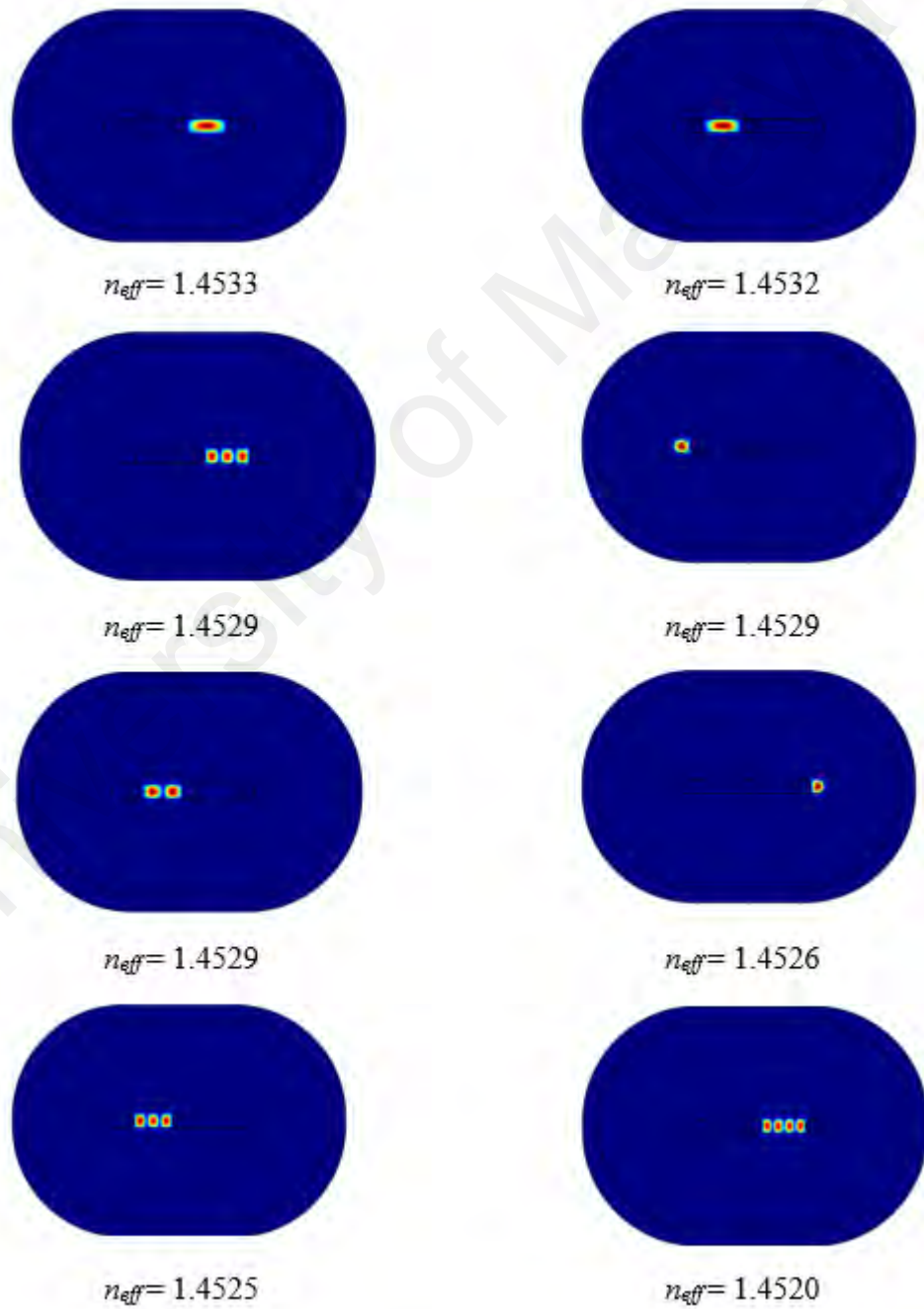


Figure 5.11: Three airholes in doped flat fiber.

Table 5.4: Modal profiles for 3 airholes at dopant concentration of 5 mol% of GeO_2 for varying effective refractive index, n_{eff}



5.4.2 Fabrication framework

The fabrication of doped flat fibers with airholes was carried out as a proof of concept. Results using the COMSOL simulation have shown that the effect of the core and cladding refractive index (as shown in d which is the mol % concentration of the GeO_2 in the core) play an important role but this is beyond the scope of this thesis as the control of the core and cladding refractive index is done at the preform fabrication stage. For this thesis, the focus will be on controlling the airhole diameter and position inside the doped area as the GeO_2 doped preform used already has definite core and cladding refractive indices. The requirements for the airhole fabrication are listed as below:

1. The airhole is not collapsed. The shape of the airhole is preferably circular shape. This can be done by sealing off the capillary after it has been fabricated or applying a minimal pressure to the capillary
2. Position for the single airhole is at the center of the core. This can be done by mounting a single capillary inside a doped preform tube using a custom-made holder.
3. Position and arrangement for the dual airhole is at both sides of the core.
4. Material of the capillary for the airhole is fused silica. It does not have to be doped preform tube. It can also be any type of silicate material.
5. The size and thickness of the airhole diameter is not stringent. It should be within the core thickness.

The simulation results obtained in Section 5.4.1 show that the size and thickness of the airhole diameter does not significantly affect the expected results. Thus, focus of the fabrication would be on maintaining an airhole in the doped flat fiber (position and shape). For this purpose, the airhole was fabricated from a capillary. Based on discussions done

in Chapter 3 and 4, it was found that capillary fabrication is affected by the following parameters:

1. Temperature of the furnace. If the temperature is too high for the preform material, the airhole will collapse and will not maintain the circular shape. For pure silica glass fiber, the recommended temperature is 2100 °C or lower. For borosilicate fibers, the recommended temperature is lower at 1000 °C. Any type of preform material can be used and drawn as long as the material's softening temperature is known.
2. Preform thickness. The preform thickness directly influence the capillary diameter. To achieve better control of the capillary diameter, dual stage drawing process will be performed.
3. Positive pressure in the capillary. This is required to maintain the airhole circular shape. However, this may not be required if the capillaries are sealed using hand torch (flame) at the opening of the capillary.
4. Vacuum pressure to the preform. This is required to flatten the capillary into flat fiber.

The methodology for the fabrication of doped flat fiber with airholes is briefly given next:

1. Fabrication of a doped preform tube with relevant core and cladding refractive index. Fabrication of the preform tube is beyond the scope of this thesis.
2. Fabrication of capillaries. Capillaries will be fabricated as the capillary will form the airhole in the doped flat fiber. Size of the capillaries will depend on the draw speed and feed speed (mass conservation law).
3. Stacking of capillary inside the preform. The capillary may be sealed at both ends in order to maintain the circular shape. A custom-made mount is used to hold the

capillary together. The capillaries can also be held together using bridges. Bridges are short pieces of the capillaries.

4. Pulling the fiber preform at a suitable temperature based on the material of the dopant and the preform and at a suitable draw speed based on the mass conservation law.
5. Basic geometrical characterization of the fabricated flat fiber with airholes to ensure that the airhole maintain its circular shape and is not collapsed.

5.4.3 Experimental results

The objective of the experimental trial was to fabricate doped flat fibers with dual airholes as a proof of concept. The thickness and the airhole diameter should be designed to allow for single mode propagation. Experimental trials were performed using available preform tubes and rods which were made of borosilicate and aluminosilicate glass. These were also chosen as they require lower furnace temperature (easier to control) and is cheaper compared to fused silica preform tubes. However, the borosilicate and aluminosilicate preform tubes may have a higher attenuation loss compared to pure silica preform tubes. The experimental trials were performed as a proof-of-concept to ensure that specific airhole diameter and position are fabricated.

5.4.3.1 Proposed design

As a proof of concept, the fabricated flat fiber will be measured using microscope or SEM should show that the two airholes are not collapsed and there is a doped core (with higher refractive index than cladding). The basic light propagation characterization results should show that single mode propagation can ideally be seen at the near field light characterization. Diameter of the airholes were planned to be around $10\text{ }\mu\text{m} - 15\text{ }\mu\text{m}$. This diameter was chosen as the flat fiber can be easily coupled with lower coupling loss into standard single mode fibers for characterization purposes.

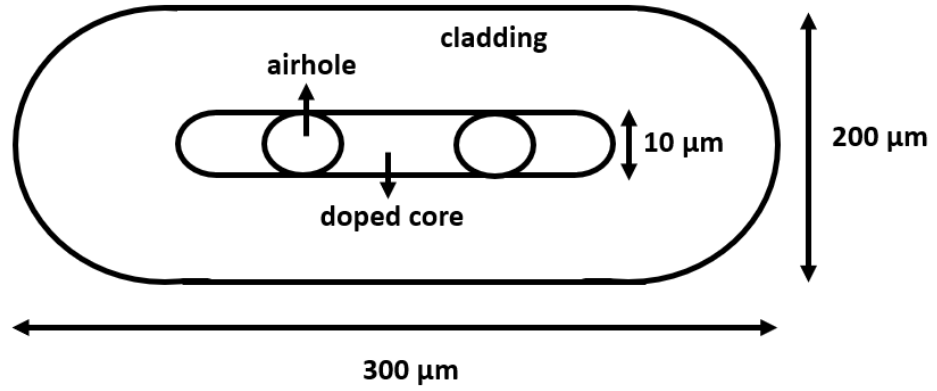


Figure 5.12: Proposed design for fabrication.

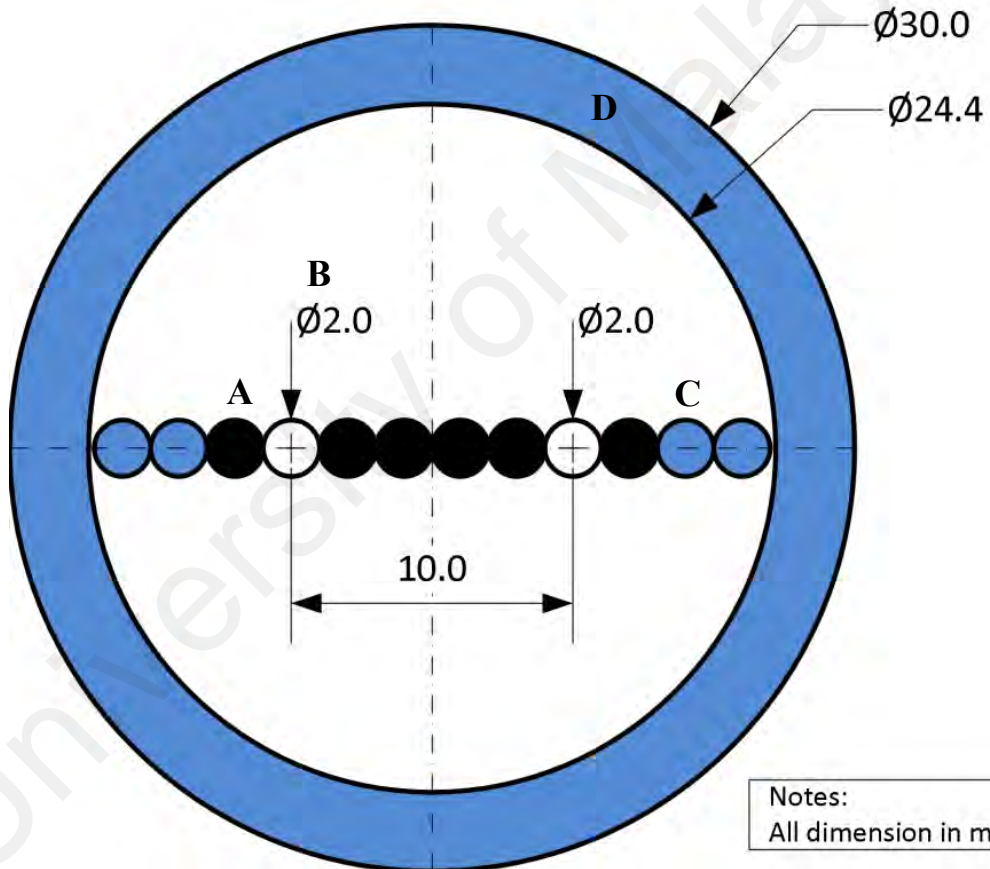


Figure 5.13: Proposed preform structure. The black circle (including the capillary) represents aluminosilicate material which has a higher refractive index of 1.538 and the blue circle (including the 30 mm preform tube) represents borosilicate material which has a lower refractive index of 1.473.

With the available materials, the preform structure as seen in Figure 5.13 was proposed. The materials that were used during the fabrication for the preform preparation were:

- A. Six aluminosilicate rods which has a refractive index of 1.538 at 587.6 nm and a diameter of 2.03 mm. The melting temperature of this rod was 1240 °C. In Figure 5.13, these were represented by the 6 circles in black.
- B. One aluminosilicate preform tube which has an outer diameter of 14.73 mm and an inner diameter of 12.69 mm. The refractive index was 1.538 at 587.6 nm and the melting temperature was 1240 °C. From this preform tube, two pieces of capillaries with the diameter size of 2 mm will be fabricated. In Figure 5.13, these were represented by the two airholes at both sides of the cores.
- C. One borosilicate preform rod with an outer diameter of 20 mm. The refractive index was 1.473 and the melting temperature was 1260 °C. From this preform tube, 4 rods with the diameter size of 2.03 mm will be fabricated. In Figure 5.13, these were represented by the 4 circles in blue colour.
- D. One borosilicate preform tube with an outer diameter of 30 mm and an inner diameter of 24.4 mm. The refractive index was 1.473 and the melting temperature was 1260 °C. In Figure 5.13, these were represented by main preform tube in blue colour which contain the array of rods and capillaries.

Table 5.5: Preform structure design.

Label	Material type	Structure	Plan
A	Aluminosilicate	Rod	Maintain
B	Aluminosilicate	Preform tube	Draw into capillary
C	Borosilicate	Rod	Draw into rod
D	Borosilicate	Preform tube	Put core array inside

5.4.3.2 Fabrication results

The flow diagram for the fabrication methodology was shown in Figure 5.14.

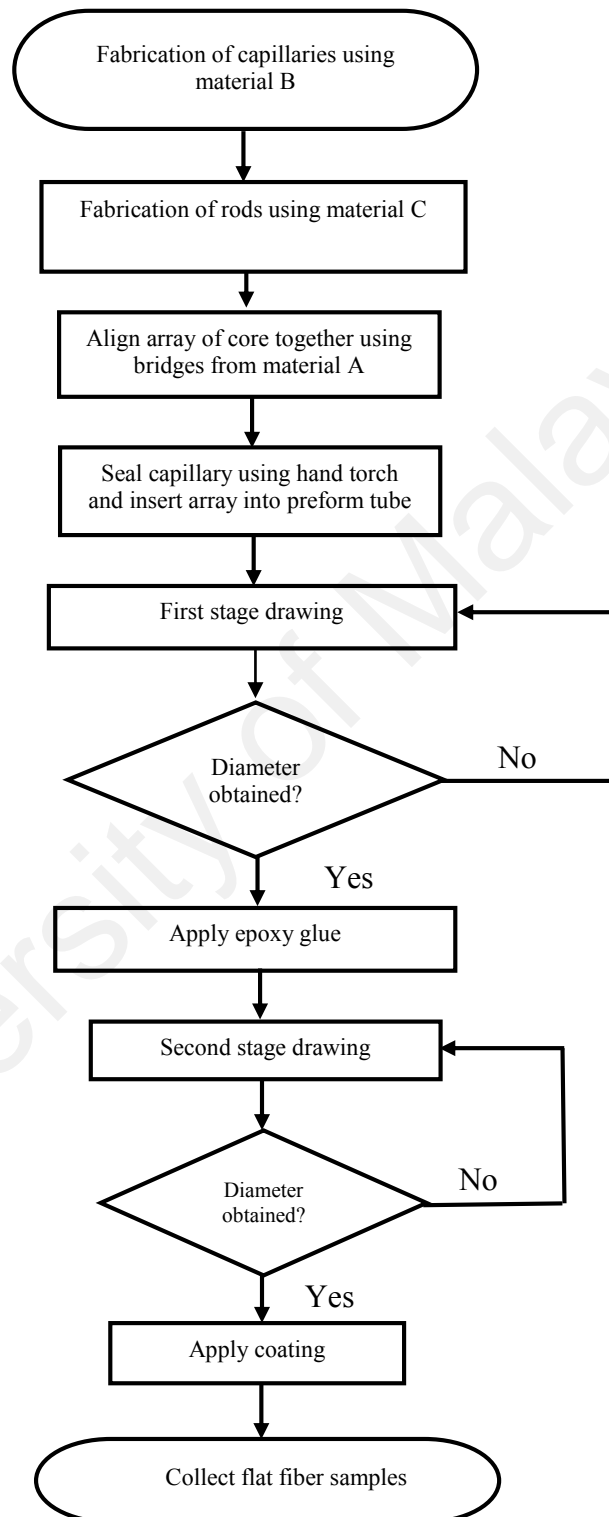


Figure 5.14: Flowchart of fabrication of doped flat fibers with dual airholes.

The detailed methodology for the fabrication of dual airholes doped flat fiber were described as below:

1. Fabrication of rod with an outer diameter of 2 mm from material D which originally has an outer diameter of 20 mm. The furnace temperature was initially set at 1000 °C for the initial material drop. This temperature was chosen as it was suitable for the borosilicate material. The feed speed was initially set as 7.21 mm/min and the draw speed was 0.7 m/min. The drawing process stabilized at the feed speed of 7.11 mm/min and the draw speed of 0.646 m/min. Then the furnace temperature was reduced to 980 °C. At this drawing condition, several 1 m length rods with an average diameter of 2 mm were fabricated.
2. Fabrication of capillary with an outer diameter of 2 mm from material B which has an outer diameter of 14.73 mm. The furnace temperature was set at 1100 °C with an initial feed speed of 12.90 mm/min and draw speed of 0.7 m/min. As the drawing process stabilized, the temperature of the furnace was increased to 1125 °C, the feed speed increased to 13.07 mm/min and the draw speed reduced to 0.658 m/min. At this drawing condition, several 1 m capillaries with an average outer diameter of 2 mm were fabricated. The capillaries were sealed at the top using a hand torch to ensure the airhole do not collapse when vacuum pressure was applied to flatten the fiber.
3. The array of rods and capillaries were arranged in a linear array as seen in Figure 5.15 using six rods from material A, two capillaries from material B and four rods from material C. Figure 5.15 shows the arrangement of the glass rods and capillaries array.
4. The linear array was fused together at top and bottom using hand torch and a few short pieces of borosilicate rods as bridges as seen in Figure 5.16.



Figure 5.15: Arrangement of the rod and capillaries linear array.



Figure 5.16: Applying bridges on linear array using hand torch.

5. The linear array was inserted into preform tube from material *D*. The length of the linear array was the same as the inner diameter of the preform tube which was 24.4 mm as there were 12 rods and capillaries in the linear array with a diameter of 2 mm each. Thus, the linear array fit nicely into the preform tube without swaying.
6. The preform tube with the core linear array was carefully positioned on the preform chuck as seen in Figure 5.17. First stage drawing method was performed.

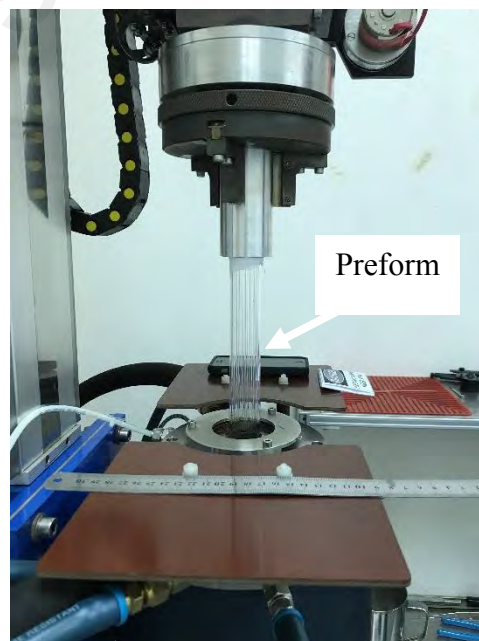


Figure 5.17: Preform drawing for first stage drawing.

7. The preform tube with the linear array was first pulled into a capillary with a diameter of 1.5 mm from the preform tube of 30 mm. The furnace temperature was set at 1100 °C, feed speed was at 17.78 mm/min and the draw speed was 1 m/min. Vacuum pressure was not applied at this stage. The capillary was successfully fabricated with an average diameter of 1.5 mm as can be seen from the microscope image shown in Figure 5.18. In Figure 5.18, we observed that the linear array of rods and capillaries were in a straight line and the two airholes for the capillary were not closed or collapsed. The diameter of the capillary was measured as 0.117 mm. From the original capillary diameter of 2 mm, the capillary reduced to 0.117 mm (117 μ m), which was a reduction of 17 times. The ratio of reduction was 17 for both the preform tube and capillary diameter.

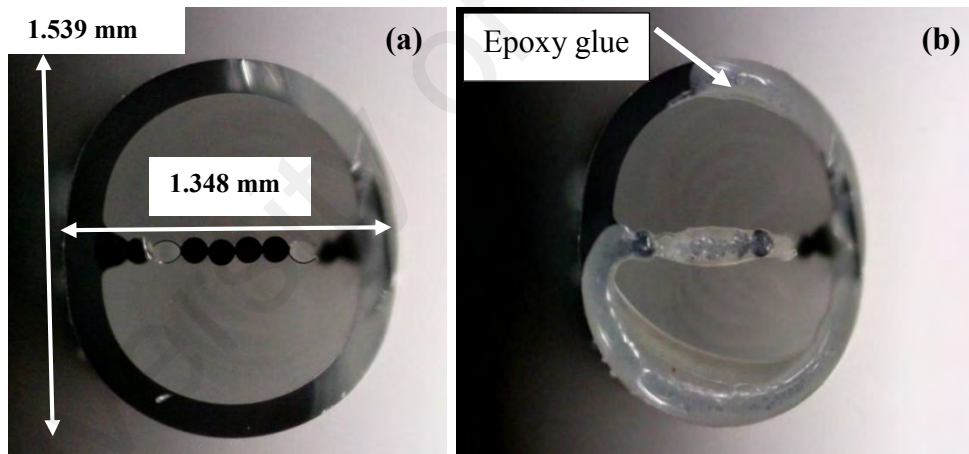


Figure 5.18: (a) Capillary with a dimension of 1.539 mm x 1.348 mm and airhole with a diameter of 0.117 mm. The two airholes were not closed. (b) Epoxy glue applied on top of the capillary.

8. Next, rapid steel epoxy glue was carefully applied to the capillary under the guidance of a microscope to ensure that the two airholes do not collapse when vacuum was applied. Figure 5.18 (b) shows the image of the capillary after the epoxy glue was applied. Next, the fiber capillary was drawn for the second stage

drawing as seen in Figure 5.19. Vacuum pressure was applied at this stage to ensure the capillary was flattened to a flat fiber shape.

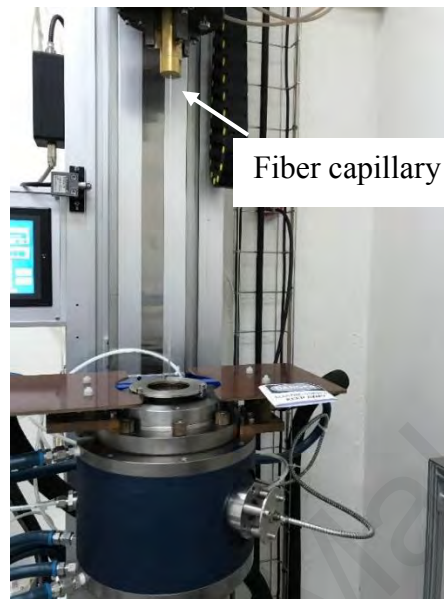


Figure 5.19: Drawing of the fiber capillary for second stage drawing.

9. The drawing conditions for the fabrication of the flat fiber were a feed speed of 5 mm/min and a draw speed of 0.8 m/min. The temperature was gradually increased from 1100 °C to 1150 °C. The applied vacuum pressure was initially 3 kPa before being increased to 6 kPa to close any eye holes. The flat fiber dimensions obtained were an average of 180 μm x 60 μm and the average tension was 20 g. Coating was applied to the flat fiber fabricated. The final fabricated flat fiber had a length of 24 m.

The microscope and SEM images obtained for the flat fiber were shown in Figures 5.20 – 5.22. Descriptions of the images were given at the figure captions. Figure 5.23 shows a microscope image of the flat fiber seen with applied light.

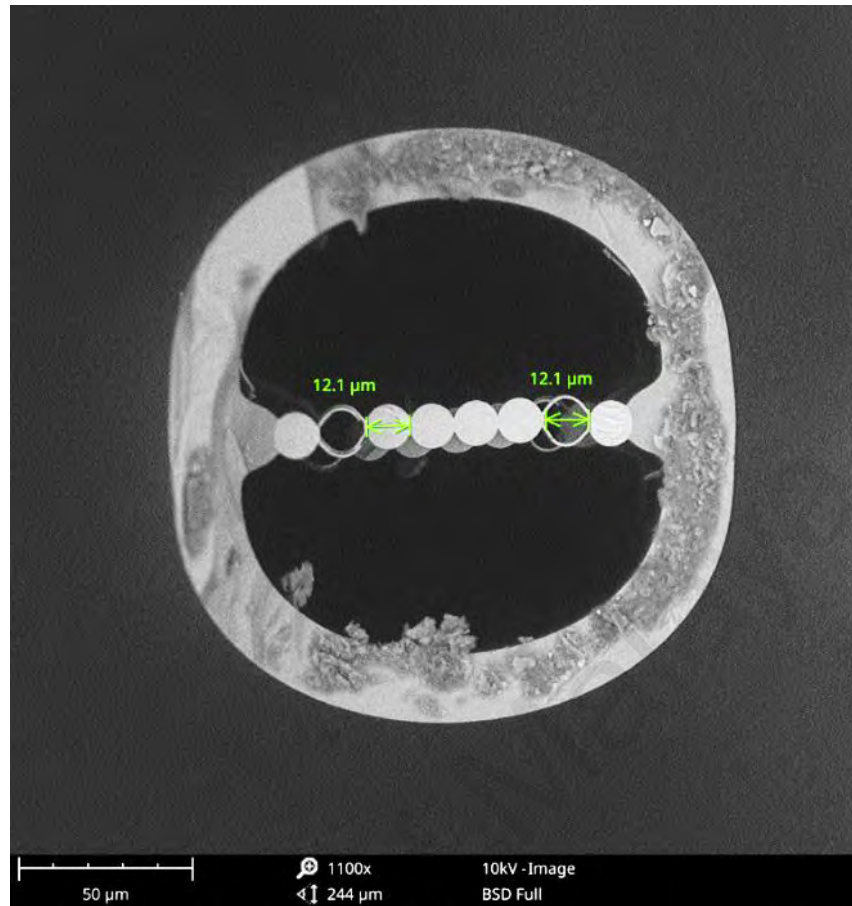


Figure 5.20: SEM image of flat fiber with dual airholes before vacuum pressure was applied. Airhole diameter was $12.1\ \mu\text{m}$ and outer diameter was $163\ \mu\text{m}$.

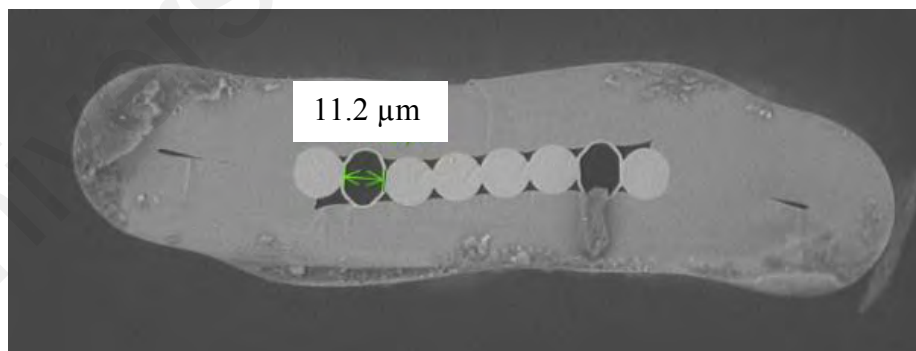


Figure 5.21: SEM image of flat fiber with dual airholes after vacuum pressure applied at $3\ \text{kPa}$. Airhole diameter was $11.2\ \mu\text{m}$ and flat fiber was $237\ \mu\text{m} \times 51.8\ \mu\text{m}$. The width of the core was $109\ \mu\text{m}$. There were some holes at the sides of the flat fiber and interstitial holes between the cores. This image was taken before coating was applied.

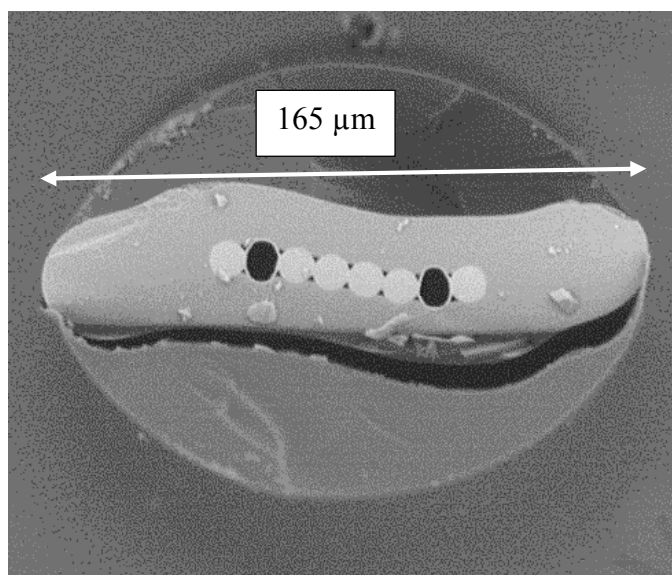


Figure 5.22: SEM image of flat fiber with dual airholes after vacuum pressure applied at 6 kPa. Airhole diameter measured was 10.8 μm and flat fiber 165 μm x 33 μm . No more holes observed at the sides and smaller interstitial holes. This image was taken after coating was applied.



Figure 5.23: Flat fiber with dual airholes seen using microscope with applied light. Airholes remain as light does not pass the airholes.

In conclusion, the fabrication successfully demonstrated the fabrication of doped flat fibers with dual airholes as a proof of concept. Although the flat fiber shape was not perfect, an airhole diameter of 10.8 μm was obtained as planned. The fabrication process and knowledge obtained from this experiment could be used to fabricate doped flat fibers with a single airhole and multiple airholes. Therefore, complex structure of flat fibers could also be fabricated in the future.

5.4.3.3 Characterization results

In this section, the near field characterization of the fabricated doped flat fiber with airholes was performed to observe the light guiding properties of the fiber. The expected results were illustrated in Figure 5.24. The experimental setup and procedures were similar to the setup shown in Figure 4.17 (b), Chapter 4. For this experiment, the multichannel laser source in Figure 4.17 (b) was replaced with a tunable laser source, the WSL-100 Santec (wavelength selectable laser) working in the C-band (1528.773 nm to 1566.723 nm). The infrared imaging camera was Micronviewer 7290A from Electrophysics (Lambda Photometrics). For this characterization, the wavelength chosen was 1550 nm. Figure 5.25 shows the actual experiment setup used. The length of the fabricated doped flat fiber with airholes initially used was approximately 30 cm. The butt coupling alignment was first tested using a visible laser source (model FOD 111 from FOD) which has an output of 1 mW at 650 nm.

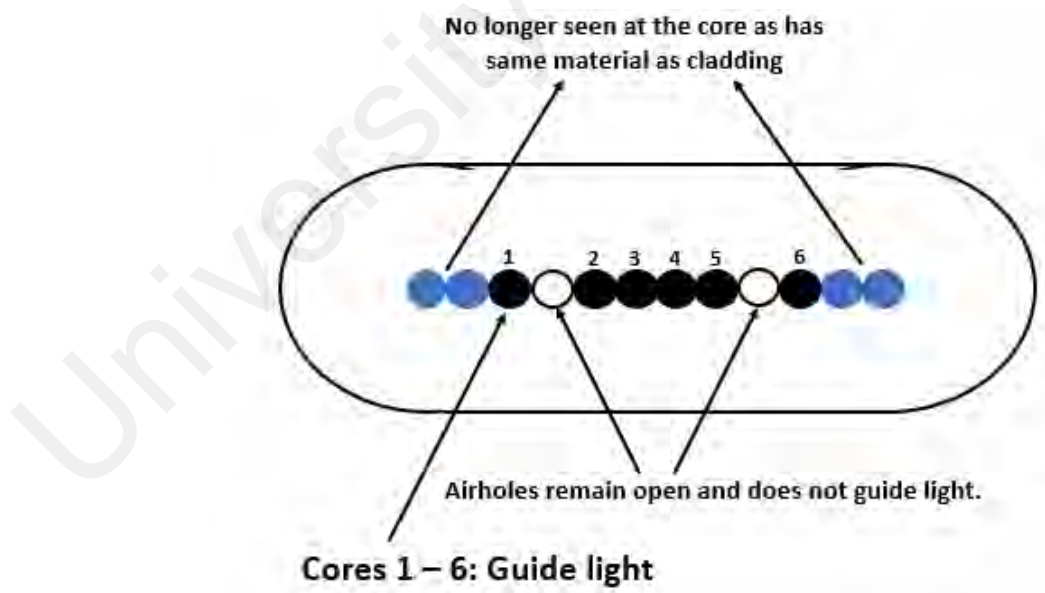


Figure 5.24: Expected results from characterization.

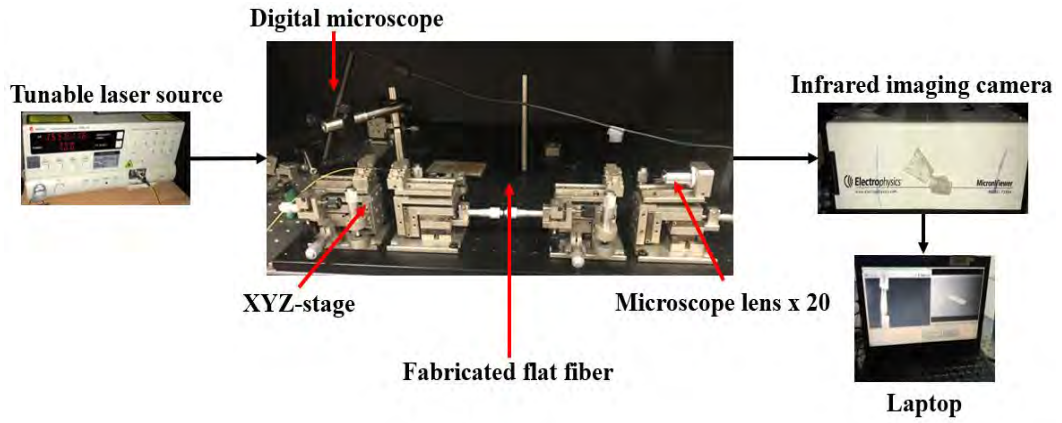


Figure 5.25: Actual experiment setup for near field characterization.

The diameter of the standard single mode fiber from the laser source was $125\ \mu\text{m}$ and from the digital microscope measurement, the dimension of the flat fiber (top view) was approximately $141\ \mu\text{m}$. The laser output from the single mode fiber is a Gaussian beam and to minimize coupling losses, the spot radius of the input beam should be similar to the fiber mode field radius (Buck, 1995). For single mode fiber with a core diameter of $8\ \mu\text{m}$, the spot radius is 10% larger than the core diameter, which is $8.8\ \mu\text{m}$. Thus, the distance A between the single mode fiber and flat fiber was set to $9\ \mu\text{m}$ for optimized distance as seen in Figures 5.26 and 5.27.



Figure 5.26: Determination of optimized distance for coupling.



Figure 5.27: Optimized distance at $9\ \mu\text{m}$.

Next, the single mode fiber launching position was varied horizontally, similar to the work done in Section 4.5.2 in Chapter 4. The previous results from Chapter 4 show that with a standard flat fiber structure, even with different launching position, all the modes can be seen at the core of the fiber. Figure 5.28 shows that with different launching position, Core 1 and Core 6 (seen in Figure 5.24) can be selectively excited as seen in the top and bottom pictures. For Cores 2,3,4 and 5, all the cores can be excited at the same time and can be seen individually with optimised alignment. The cores at the sides of Core 1 and Core 2 were no longer seen as they have the same refractive index and material as the preform tube. The significance of these results will be discussed in the next section.

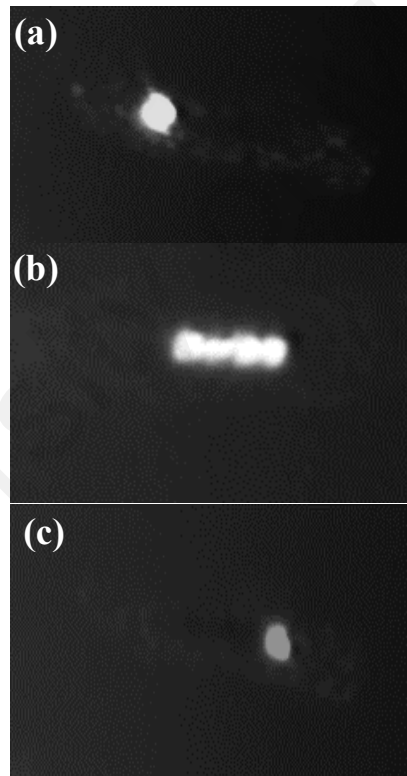


Figure 5.28: CCD images at different launching conditions (a) left (b) middle and (c) right

5.4.3.4 Discussion on fabrication and characterization results

Due to limited doped preforms available, the author had proposed a new and improved fabrication method to fabricate the core structure in a doped flat fiber with dual airholes. Previously, the core array on multicapillary flat fiber consisted a linear array of capillaries

and multicore flat fiber consisted of a linear array of step index glass rods. Both core structures were hung on a custom made mount before being drawn into fiber size. In particular, for multicapillary flat fiber, the current fabrication method does not allow control of the core array as the drawing conditions discussed in Chapter 3 and 4 can affect the formation of the core array. Optimization of the current fabrication method thus required multiple experimental runs in order to produce the desired fiber dimension and core structure. Using the method proposed in Section 5.4.3, only one experimental run was performed to achieve the desired core structure and dimension, which proved greater control on the fabrication process. The improved fabrication methods introduced in Section 5.4.3 were:

1. Introducing a glass rod with a higher refractive index as the waveguide in the core region. Previous work on multicore flat fiber used step index glass rods as channels. By using a rod, the size of the core can be controlled easily and reduced the cost of fabrication. The refractive index of the core can also be controlled by selecting from commercial ready-made glass rods. The fabrication results in Section 5.4.3.2 proved this.
2. Introducing airholes in between the rods. The airholes essentially act to separate the waveguide channels as light can only propagate in the rods which has a higher refractive index. Characterization results shown in Figure 5.28 proved that light was successfully guided in the rods while the airholes act as a barrier between each channel.
3. Introducing rods with refractive index similar to the cladding at the sides of the core structure. This allows the flexibility to arrange the core array so that it fits exactly into the center of the preform tube. The arrangement of core and airholes can also be easily designed to suit multiple potential applications which will be discussed in the next section. Results obtained from the fabrication process show

that the linear array maintained its structure and desired dimension at the end of the fabrication process. By fitting it exactly into the preform tube, there were less gap or disruption affecting the core structure.

The characterization results from Section 5.4.3.3 confirmed the hypothesis that the fabrication technique introduced in Section 5.4.3.2 allow additional waveguide channels to be added on a flat fiber, without the need for additional technology. In terms of loss measurements, this proof-of-concept fabrication process used commercially available grade rods and capillaries which have a high loss and this would also influence the fabricated fiber. However, if a pure silica flat fiber with 6% Ge doped core is used, it can be estimated that the attenuation loss will be 0.11 dB/cm if butt coupling is used as stated in Chapter 4, Section 4.5.1.

The method proposed and shown in this work is simple, cost effective and only require the use of a drawing tower. In order to fabricate waveguide channels on the flat fiber, rods with a higher refractive index than the cladding can be arranged in a linear or predefined shape that alternately with a capillary and rod with lower refractive index. In the next section, potential applications of complex flat fiber structures that can be fabricated using this new and improved fabrication method will be discussed.

5.5 Potential Multistructured Flat Fibers

This section proposed potential multistructured flat fiber that can be fabricated using the fabrication method introduced in Section 5.4.3. The core structure can be arranged in a variety of arrangement to provide different types of flat fibers. The new and improved fabrication method allow the control of the following parameters:

1. Dimension of the core structure including individual core diameter, individual capillary diameter and number of the total core and cladding structure. This

flexibility allows us to design a wide array of core structures as shown in Figure 5.29 which include single core flat fiber, dual core flat fiber, multicore flat fiber, multicore and multicapillary flat fiber and multi-index flat fiber. The designs proposed solves the problem of collapsed airholes (Fitt *et al.*, 2001) which was discussed in Section 5.2. The development of single core flat fiber can provide an alternative solution to providing single mode propagation in flat fibers (Poh *et al.*, 2017). It may also be possible to design individual cores with different diameters. The airholes in both the preform, rod and fiber can also be used to store /flow analytes for sensing purposes.

2. Core refractive index. This can be easily controlled by acquiring ready-made collapsed rods with specific refractive index. The problem of difficulty in fabrication of multidopant flat fibers seen in Section 4.6, Chapter 4 can be solved with this fabrication method. These designs also solve the problem of diffused dopants during optical fiber drawing process (Lyytikainen *et al.*, 2004).
3. Cladding diameter and refractive index. In order to achieve certain optical propagation properties, the cladding diameter and refractive index can also be controlled by selecting suitable preform tubes.
4. Distance between the cores. This is done by arranging rods which have the same refractive index as the cladding in between the cores with the higher refractive index. Thus, distance between the cores for specific optical application can be accurately controlled.

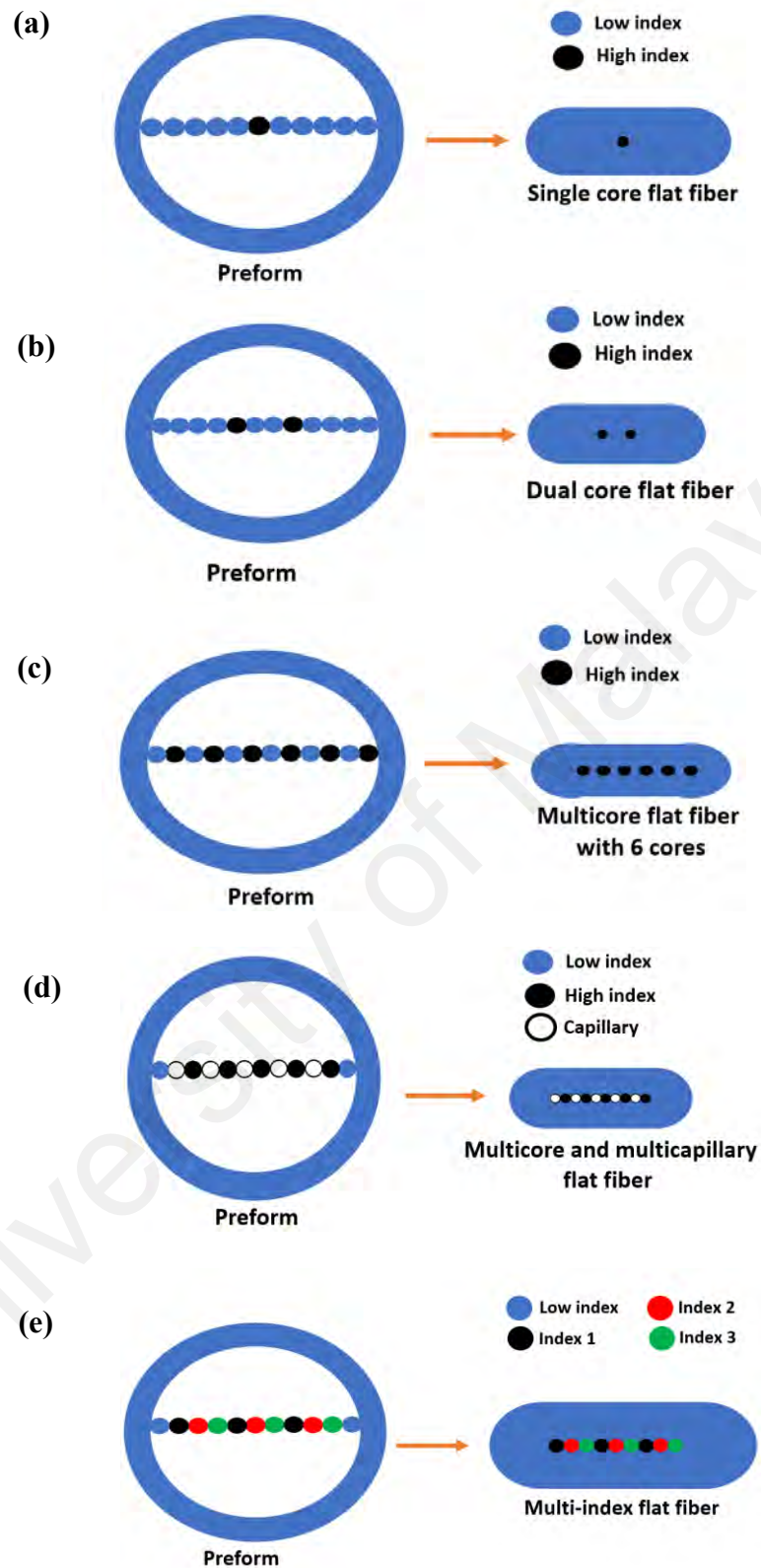


Figure 5.29: Different flat fiber structure. (a) Single core flat fiber (b) Dual core flat fiber (c) Multicore flat fiber (d) Multicore and multicapillary flat fiber (e) Multi-index flat fiber

5.6 Potential Applications

This section proposed several potential applications and optical devices that can be developed from the flat fiber structures proposed in the previous section.

1. Single core flat fiber

A single core flat fiber can be used as a single mode flat fiber that is comparable to single mode planar waveguides. Applications for single mode planar waveguides include optical sensing applications that conventionally required a stringent requirements and multiple fabrication steps (Mukundan *et al.*, 2009). In Poh *et al.*, 2017, the single mode propagation demonstrated in a flat fiber had a thin core (for high sensitivity sensing ability) and required defect holes filled with liquid with higher index matching oil. With optimized design, the single core flat fiber can also be used as a channel waveguide such as straight waveguide (Saleh & Teich, 2007) which can be manipulated for applications in sensing and integrated optics. The core diameter of a single mode flat fiber core diameter can also be made very thin (less than 5 μm) and combined with a multimode flat fiber (with a longer core width) to be used in a Mach-Zehnder interferometer for refractive index sensing purposes (Xia *et al.*, 2010 & Shao *et al.*, 2014) such humidity sensor based on a hetero- core optical fiber (Akita *et al.*, 2010), a fiber optic pH sensor (Gu *et al.*, 2009) and a metal ion sensor (Gu *et al.*, 2011). A high temperature sensor has also been demonstrated using a thin core fiber modal interferometer (Zhu *et al.*, 2010).

2. Dual core flat fiber

A dual core flat fiber is similar to planar waveguides with the core structure in close proximity to each other, which may exchange power or be used as a directional coupler (Saleh & Teich, 2007). However, further investigation is

required to determine its coupling length for use as a passive optical coupler (Drolet & Vallée, 1994 & Vallee & He, 1993). In Ribeiro *et al.*, 2017, a dual core single mode fiber can also be used as an optical amplifier to provide flat gain when certain design parameters are met. An integrated in-fiber Michelson interferometer had also been demonstrated based on a poled hollow twin-core fiber (Liu *et al.*, 2011).

3. Multicore flat fiber

Multicore fiber can be used to increase the optical fiber capacity by allowing several different signals to transmit simultaneously through multiple spatial paths (Mizuno *et al.*, 2016, Saitoh & Matsuo, 2016 & Sakamoto *et al.*, 2017). Research on multicore has generated a huge interest, with work focusing to increase the bit rate (Zhu *et al.*, 2011, Sakaguchi *et al.*, 2013 & Soma *et al.*, 2018), transmission distance (Takara *et al.*, 2012 & Sakamoto *et al.*, 2018) and number of cores (Stone *et al.*, 2014 & Sakaguchi *et al.*, 2015). One of the main issues with multicore fiber is to control the signal crosstalk between the cores which require further investigation (Francois & Laramée, 2013, A. Samir & Batagelj, 2016), Hayashi *et al.*, 2012 & Zhou *et al.*, 2016). It had been demonstrated in Egorova *et al.*, 2014 that a multicore fiber with eight cores in a rectangular cross section had no core-to-core coupling and crosstalk value of -60 dB. A multicore fiber with a concaved double-D shape cross section has also been developed for passive fiber alignment for connector assembly (Nagashima *et al.*, 2017). The core distance can determine whether the multicore fibers are weakly-coupled or strongly-coupled (Saitoh & Matsuo, 2016). In Mahdiraji *et al.*, 2014 fabrication of a multicore flat fiber was performed using standard step index fibers as the core and the average fabricated core size was 5.1 μm with an average core-to-core pitch of 77.8 μm , which was dependent on the dimensions of the step index fiber. With the improved

fabrication technique, the core size and spacing between each core can be controlled in a simple method.

4. Multicore and multicapillary flat fiber and multi-index flat fibers

These fibers are novel optical devices, and further investigation is required to see its feasibility and suitability to be used for sensing purposes, waveguide devices (Hunsperger, 2009), grating-based devices, lab-on-chip devices, microfluidic based devices (Monat & Eggleton, 2007), photonic lanterns (Leon-Saval *et al.*, 2014 & Huang *et al.*, 2015), optically passive and active devices and few-mode fibers (Wu & Chiang, 2016).

5.7 Summary

In this chapter, multicapillary flat fiber and multicore flat fiber have been discussed. Multicapillary flat fiber cannot propagate light in the air holes and further investigation was required to determine its potential applications. Multicore flat fiber can potentially be used for long haul optical fiber communications. A new flat fiber design had been proposed in this chapter. The design was a doped flat fiber with dual airholes. This design aimed to improve the multicapillary flat fiber previously fabricated by adding a doped layer into the core. Simulation using COMSOL was performed to optimize the design of the new flat fiber design in terms of its core geometry, refractive indices and number of airholes. Due to limited doped preforms available, the author had proposed a new and improved fabrication technique to fabricate the new flat fiber design. The proof of concept fabrication technique was successfully demonstrated. Light was also successfully guided in the core. This novel fabrication method allows the control the dimensions of the core structure, the refractive index of the core structure, the cladding dimensions and refractive index and the arrangement of the core structure. This fabrication technique is simple, cost effective and only require the use of drawing tower. For the core arrangement, preform rods and tubes of varying dopant concentration can be used.

CHAPTER 6: CONCLUSION AND FUTURE WORKS

In this chapter, the main findings from this thesis will be summarized and its implications will be discussed. The author's research achievements and main contributions will be outlined. Suggestions for future work will also be presented in this chapter.

6.1 Conclusions

The aim of this study was to characterize drawing parameters related to the fabrication of flat fibers, which can lead to the development of novel multistructured flat fibers. In order to achieve this, this research focused on the effects of drawing parameters on the flat fiber dimensions and the control of the flat fiber dimensions. This was done by fabrication of flat fibers using pure silica and doped preform tubes. Geometrical and basic optical characterization were also performed on the fabricated flat fibers. Novel multistructured flat fibers were developed and fabricated, in particular the fabrication of doped flat fiber with dual airholes led to a new and improved fabrication technique for the development of novel multistructured flat fibers. Fabrication know-how including the drawing recipe obtained in this work is useful as it improves fabrication process, reduces preform wastage and minimizes experimental runs which leads to cost and time saving.

In this thesis, the main findings for each objective are summarized as below:

1. Objective 1 - To propose and fabricate flat fibers (with no core) with different thickness in order to investigate and characterize related drawing parameters (furnace temperature, draw speed, feed speed and vacuum pressure).
 - a) In the drawing of 1 mm capillaries from a pure silica preform with a thickness of 3 mm, the furnace temperature was varied between 1990 °C to 2200 °C. To achieve a 1 mm pure silica capillary with a 5% error, the range of furnace

temperature was approximately 2110 °C to 2170 °C. As the furnace temperature increased, the viscosity and draw tension reduced and this effect resulted in a smaller outer diameter for the capillary. This conclude that furnace temperature plays an important role in controlling the outer diameter of a capillary and the final flat fiber dimension.

- b) In the drawing of 1 mm capillaries from a pure silica preform with a thickness of 1 mm and 3 mm, the furnace temperature was varied between 1980 °C to 2205 °C. An increase of 2 mm in the preform thickness resulted in an outer diameter that was twice as sensitive to the effect of furnace temperature. The measured inner diameter of the thin preform showed that if the temperature was increased to 2230 °C, the capillary would completely collapse. It was found that the capillaries drawn from the thin preform were more sensitive to temperature deviations. For better control of the capillary dimension, a thick preform was recommended. Thus, it can be concluded that in addition to furnace temperature, preform wall thickness also influenced the thickness of the capillary and the final flat fiber dimension.
- c) In the drawing of 1 mm capillaries from a pure silica preform with a thickness of 1 mm and 3 mm, the draw speed was varied from 1 m/min to 2.0 m/min at steps of 0.2 m/min. After 1.2 m/min and above, the outer diameter was nearly the same despite different preform wall thickness. The feed speed for the preform with thickness of 3 mm were varied between 2 mm/min and 6.48 mm/min. At the same draw speed with two different feed speeds, the higher feed speed resulted in a larger outer diameter. It was observed that the outer diameter of the capillary decreased as the draw speed was increased. A higher feed speed was also proportional to a high draw speed. The draw speed and

feed speed using different preform wall thickness had nearly similar effect on the outer diameter capillary and the final flat fiber dimension.

- d) In the drawing of flat fibers from a pure silica preform with a thickness of 1 mm and 3 mm, the vacuum pressure was varied from 0 kPa to 20 kPa (thin preform) and 0 kPa to 59 kPa (thick preform). It was found that a vacuum pressure of 1.5 kPa (thin preform) and 2.0 kPa (thick preform) was required for the flat fiber to flatten. For the thin preform, increasing the vacuum pressure up to 2 kPa had further deformed the flat fiber. For the thick preform, a high vacuum pressure of 59 kPa was required to further deform the flat fiber. Thus, vacuum pressure affects flat fiber with a different preform wall thickness differently due to the different volume of the preform. In a thin preform, the hole where vacuum was applied was larger and the volume was smaller, so the influence of surface tension was more significant compared to a thick preform which has a smaller hole and larger volume. A thick preform with more volume was less sensitive to deviations in the vacuum pressure due to lower surface tension effects and thus it would be easier to control the size of its fabricated flat fiber.
2. Objective 2 - To propose and fabricate doped flat fibers in order to investigate and characterize related drawing parameters (furnace temperature, draw speed, feed speed and vacuum pressure).
- a) In the drawing of flat fibers from preforms doped with high concentration of germanium oxide, the flat fiber was collapsed at a vacuum of 1 kPa, average draw speed of 0.07 m/min, average feed speed of 0.34 mm/min and temperature of 2100 °C. However, there was a hole in the center of the core, which still existed despite increasing the vacuum to 5 kPa. Core aspect ratio of 5.20: 1 had been achieved when the flat fiber dimension was 310 μm x 190

μm . By varying the vacuum pressure, dimension of the flat fiber and its core was varied as well. Adding dopants into the pure silica preform decreased its viscosity and a higher temperature was required for its melting temperature. Due to dopant diffusion into the cladding of the flat fiber, the core structure was pulled to the side before being fully collapsed, thus creating an airhole in the center of the core. Applying more vacuum had no effect on collapsing the airhole due to the diffused cladding. In conclusion, for doped flat fiber, optimum temperature was required to ensure the desired flat fiber dimension was achieved.

- b) Single stage drawing of capillaries was performed to get a desired diameter of $125\ \mu\text{m}$ and $1.25\ \text{mm}$ from a preform with an outer diameter of $25\ \text{mm}$ and inner diameter of $19\ \text{mm}$. It was difficult to control the drawing process of the $125\ \mu\text{m}$ capillary, with multiple breaks occurring despite varying the temperature, draw speed and feed speed. The $1.25\ \text{mm}$ capillary was achieved much easier and no fiber breaks were observed during the drawing process. Dual stage drawing was performed for flat fibers doped with 6%mol germanium oxide. Thus, dual stage drawing for flat fibers were proposed to overcome the difficulties in drawing to a smaller desired diameter.
- c) Basic characterization was performed for samples of flat fibers with 6%mol germanium oxide. The near field intensity profiles were obtained at wavelengths of $635\ \text{nm}$, $1310\ \text{nm}$ and $1550\ \text{nm}$ for samples with lengths of $60\ \text{cm}$. The intensity profile showed multimode propagation in flat fibers. The flat fibers were not single mode due to its large core thickness. This was a limitation due to core dimension. Thus, to achieve single mode propagation, suitable preform core is required.

d) The drawing of thin preform tubes doped with germanium oxide and boron trioxide proved challenging. Fibers obtained include deformed fibers but some flat fibers were drawn from the capillaries fabricated using dual stage drawing. The flat fiber samples had a thin core which measured less than 1 μm . Germanium and boron were not detected in the samples using EDX measurement due to dopant diffusion. In the drawing process of flat fibers, the feed speed and draw speed can be controlled, which influenced the flat fiber dimensions to a certain extent. However, the previous results had shown that drawing parameters such as furnace temperature and vacuum pressure, relating to viscosity and surface tension, are a function of the preform material itself. Thus, knowledge of the preform material also influence the final flat fiber dimension and is important before starting any fabrication process.

3. Objective 3 and Objective 4 - To propose and fabricate a new type of multistructured flat fiber including multicore flat fiber and to propose and demonstrate improved fabrication technique for fabrication of multistructured flat fibers including multicore flat fibers.

a) Novel multistructured flat fiber such as multicapillary flat fiber were fabricated but it was found that the multicapillary flat fiber does not guide light due to no dopants in the core and the arrangement of the airholes do not allow light propagation to occur.

b) A novel multistructured flat fiber which is doped flat fiber with dual airholes had been designed and developed to overcome the limitations of the multicapillary flat fiber. The design process used the software COMSOL to design a single mode flat fiber. The parameters that were investigated during the simulation work were core thickness, refractive index of the core and

cladding, number of airholes, wavelength of light propagating in the flat fiber and airhole diameter.

- c) A new and improved fabrication technique had been proposed to fabricate the doped flat fiber with dual airholes. The proof-of-concept fabrication for the doped flat fiber was successfully demonstrated. This improved fabrication method allows the control the dimensions of the core structure, the refractive index of the core structure, the cladding dimensions and refractive index, the arrangement of the core structure and the distance between the cores. This fabrication technique is simple, cost effective and only require the use of drawing tower. For the core arrangement, preform rods and tubes of varying dopant concentration can be used.

6.2 Future Work

The new and improved fabrication technique can potentially be used to develop a wide range of multistructured flat fibers. Suggestions for future work are outlined as follows:

- a) Fabrication of doped flat fiber with dual airhole using pure silica material as the cladding material and glass rods with 0.1% dopant concentration of GeO_2 to observe single mode propagation in the flat fiber. This can be done using the new and improved fabrication technique that was successfully demonstrated in this thesis. Characterization of light guiding properties can be done to confirm single mode propagation. The feasibility of the multistructured flat fiber as a sensor can also be done as the dual airholes can be used to store the analyte to be sensed. Simulation can be done to determine what kind of analyte that can be stored inside the dual airholes by investigating its optical properties with materials that have different refractive indices.

- b) Fabrication of single core, dual core and multi core flat fiber using pure silica material as the cladding material and a higher index rod as the core using the new and improved fabrication technique. Simulation can be done to optimize the designs of these multistructured flat fibers including its core structure arrangement. Characterization of the fabricated multistructured flat fibers can be done to observe its attenuation and light guiding properties. The crosstalk between the cores in multicore flat fibers can also be investigated in order to assess its suitability for long haul communications.
- c) Fabrication of multicapillary flat fiber using pure silica material as the cladding material and a higher index rod as the core using the new and improved fabrication technique. Simulation will be done to determine optimum core structure arrangement with airholes and rods. The core dimension could be designed so that it becomes single mode propagation. Once fabricated, characterization will be done to observe the feasibility of the multicapillary flat fiber as a sensor.
- d) Fabrication of multi-index flat fiber using pure silica material as the cladding material and two different types of refractive index rods as the core using the new and improved fabrication technique. Characterization of the fabricated flat fiber will be done observe its attenuation and light guiding properties.
- e) The multistructured flat fibers can be developed into sensors and integrated optics devices such as optical coupler, beam combiner and straight waveguides. Simulation can be done to optimize the designs of these multistructured flat fibers. Further research is required to determine its functionality. As sensors, related parameters such as accuracy, sensitivity and repeatability tests can be characterized. For straight waveguides, the waveguide parameters and propagation characteristics can be investigated.

Other suggestions for future work include detailed optical characterization of the flat fiber fabricated to study its optical performance. Characterization work that can be done are fiber bending loss, fiber birefringence and beat length. Further work can also be done to investigate the potential of the flat fiber for applications such as MMI based power splitters.

6.3 Outcome and Author's Achievements

In this thesis, the author had outlined several significant findings related to the fabrication of flat fibers and multistructured flat fibers. Methods were also proposed to solve issues in controlling the flat fiber dimensions such as using dual stage drawing.

The significant contributions to the body of knowledge in the field of specialty optical fiber fabrication, in particular fabrication of flat fibers and multistructured flat fibers, from this thesis are outlined as follows:

- a) Successfully designed and developed a new multistructured flat fiber which was doped flat fiber with dual airholes.
- b) Successfully demonstrated proof-of-concept fabrication of a new multistructured flat fiber which was doped flat fiber with dual airholes using a new and improved fabrication technique. The novel fabrication technique allows a wide range of multistructured flat fibers to be fabricated without the need of a doped preform. The technique can be used to control the dimensions of the core structure, the refractive index of the core structure, the cladding dimensions and refractive index and the arrangement of the core structure. The technique is simple, cost effective and only require the use a drawing tower.
- c) Successfully developed flat fiber fabrication know-how for drawing parameters such as furnace temperature, preform wall thickness, draw speed and vacuum pressure that influenced the final flat fiber dimension. The furnace temperature

and vacuum pressure will also be greatly affected by the preform material used. Higher furnace temperature and higher draw speed result in capillaries with smaller outer diameter, thinner wall thickness preform is more sensitive to changes in drawing parameters, a higher draw speed is proportional to a higher feed speed and only low vacuum pressure is required to flatten flat fiber.

- d) Demonstrated that control of flat fiber dimension is achievable when drawing to a diameter of 1.25 mm compared to 125 μm . Thus, dual stage drawing technique was proposed for the fabrication of flat fibers.
- e) Fabricated GeO_2 doped flat fibers using single stage and dual stage drawing method and GeO_2 & B_2O_3 doped flat fibers using dual stage drawing method. Basic optical characterization was also performed on the GeO_2 doped flat fibers.

In conclusion, this research had successfully achieved its objective to characterize drawing parameters in the fabrication of flat fiber, which led to the development of a new and improved fabrication technique for the fabrication of novel multistructured flat fibers.

REFERENCES

- Adikan, F. R. M. (2007). *Direct UV-written waveguide devices*. University of Southampton.
- Adikan, F. R. M., Sandoghchi, S. R., Yi, C. W., Simpson, R. E., Mahdi, M. A., Webb, A. S., . . . Holmes, C. (2012). Direct UV Written Optical Waveguides in Flexible Glass Flat Fiber Chips. *IEEE Journal of Selected Topics in Quantum Electronics*, 18(5), 1534-1539.
- Agrawal, G. P. (1995). Nonlinear fiber optics. *the Institute of Optics, University of Rochester, Optics and Photonics, Academic Press, ISBN: 0-12045143-3*.
- Akita, S., Sasaki, H., Watanabe, K., & Seki, A. (2010). A humidity sensor based on a hetero-core optical fiber. *Sensors and Actuators B: Chemical*, 147(2), 385-391.
- Alawiah, A., Bauk, S., Abdul-Rashid, H. A., Gieszczyk, W., Hashim, S., Mahdiraji, G. A., . . . Bradley, D. A. (2015). Potential application of pure silica optical flat fibers for radiation therapy dosimetry. *Radiation Physics and Chemistry*, 106, 73-76.
- Alessi, A., Agnello, S., Ouerdane, Y., & Gelardi, F. M. (2011). Dependence of the emission properties of the germanium lone pair center on Ge doping of silica. *Journal of Physics: Condensed Matter*, 23(1), 015903.
- Alessi, A., Girard, S., Marcandella, C., Cannas, M., Boukenter, A., & Ouerdane, Y. (2011). Raman investigation of the drawing effects on Ge-doped fibers. *Journal of Non-Crystalline Solids*, 357(1), 24-27.
- Ambran, A. S. W., Christopher, H., Faisal Rafiq Mahamd, A., James, C. G., Jayanta, K. S., Lewis, G. C., . . . Sumiaty. (2012). Fabrication of a Multimode Interference Device in a Low-Loss Flat-Fiber Platform Using Physical Micromachining Technique. *Journal of Lightwave Technology*, 30(17), pp. 2870-2875.
- Ambran, S., Holmes, C., Gates, J. C., Webb, A. S., Carpenter, L. G., Adikan, F. R. M., . . . Sahu, J. K. (2012). Fabrication of a multimode interference device in a low-loss flat-fiber platform using physical micromachining technique. *Journal of Lightwave Technology*, 30(17), 2870-2875.
- Ambran, S., Holmes, C., Gates, J. C., Webb, A. S., Sahu, J. K., & Smith, P. G. R. (2011, 22-26 May 2011). *UV-written Bragg gratings in a flat-fiber platform as a bending and twisting sensor*. Paper presented at the 2011 Conference on Lasers and Electro-Optics Europe and 12th European Quantum Electronics Conference (CLEO EUROPE/EQEC).
- Argyros, A. (2009). Microstructured Polymer Optical Fibers. *Journal of Lightwave Technology*, 27(11), 1571-1579.
- Bansal, N. P., & Doremus, R. H. (1986). Handbook of Glass Properties Academic. Orlando, FL, 550-551.

- Barton, G., van Eijkelenborg, M. A., Henry, G., Large, M. C. J., & Zagari, J. (2004). Fabrication of microstructured polymer optical fibres. *Optical Fiber Technology*, 10(4), 325-335.
- Barton, G. W., Law, S. H., & Phan, T. N. (2004). Limitations to the Manufacture of Specialty Optical Fiber. *Journal of Manufacturing Science and Engineering*, 127(3), 663-669.
- Buck, J. A. (1995). *Fundamentals of optical fibers*: Wiley.
- Center, Q. E. C. R. (2016). *2015 Specialty Optical Fibers Industry Report - Global and Chinese Market*.
- Chen, C., & Jaluria, Y. (2009). Effects of doping on the optical fiber drawing process. *International Journal of Heat and Mass Transfer*, 52(21-22), 4812-4822.
- Chen, Y., & Birks, T. A. (2013). Predicting hole sizes after fibre drawing without knowing the viscosity. *Optical Materials Express*, 3(3), 346-356.
- Cheng, X., & Jaluria, Y. (2002). Effect of draw furnace geometry on high-speed optical fiber manufacturing. *Numerical Heat Transfer: Part A: Applications*, 41(8), 757-781.
- Cheng, X., & Jaluria, Y. (2004). Feasibility of High Speed Furnace Drawing of Optical Fibers. *Journal of Heat Transfer*, 126(5), 852-857.
- Cheng, X., & Jaluria, Y. (2005a). Effect of Furnace Thermal Configuration on Optical Fiber Heating and Drawing. *Numerical Heat Transfer, Part A: Applications*, 48(6), 507-528.
- Cheng, X., & Jaluria, Y. (2005b). Optimization of a thermal manufacturing process: Drawing of optical fibers. *International Journal of Heat and Mass Transfer*, 48(17), 3560-3573.
- Choudhury, S. R., & Jaluria, Y. (1998a). Practical aspects in the drawing of an optical fiber. *Journal of materials research*, 13(2), 483-493.
- Choudhury, S. R., & Jaluria, Y. (1998b). Thermal transport due to material and gas flow in a furnace for drawing an optical fiber. *Journal of materials research*, 13(2), 494-503.
- Cordaro, M., Rode, D. L., Barry, T., & Krchnavek, R. R. (1994). Precision fabrication of D-shaped single-mode optical fibers by in situ monitoring. *Journal of Lightwave Technology*, 12(9), 1524-1531.
- Corning. SMF-28 Single mode fiber. from <https://www.corning.com/media/worldwide/coc/documents/Fiber/SMF-28%20Ultra.pdf>
- Davis, G. M., Zhang, L., Chandler, P. J., & Townsend, P. D. (1996). Planar and channel waveguide fabrication in LiB3O5 using MeV He+ ion implantation. *Journal of Applied Physics*, 79(6), 2863-2867.

- Derickson, D. (1998). *Fiber optic test and measurement*: Prentice Hall.
- Doremus, J. F. S. a. R. H. (2008). *Ceramic and glass materials: Structure, properties and processing*: Springer.
- Doremus, R. H., & Doremus, R. H. (1994). *Glass science*: Wiley New York.
- Dutton, H. J. (1998). *Understanding optical communications*: Prentice Hall PTR New Jersey.
- Dyott, R. B. (1995). *Elliptical Fiber Waveguides*: Artech House.
- Egorova, O. N., Semjonov, S. L., Senatorov, A. K., Salganskii, M. Y., Koklyushkin, A. V., Nazarov, V. N., . . . Dianov, E. M. (2014). Multicore fiber with rectangular cross-section. *Optics Letters*, 39(7), 2168-2170.
- Erickson, D., Mandal, S., Yang, A. H. J., & Cordovez, B. (2008). Nanobiosensors: optofluidic, electrical and mechanical approaches to biomolecular detection at the nanoscale. *Microfluidics and nanofluidics*, 4(1-2), 33-52.
- Fitt, A., Furusawa, K., Monro, T., Please, C., & Richardson, D. (2002). The mathematical modelling of capillary drawing for holey fibre manufacture. *Journal of Engineering mathematics*, 43(2-4), 201-227.
- Fitt, A. D., Furusawa, K., Monro, T. M., & Please, C. P. (2001). Modeling the fabrication of hollow fibers: capillary drawing. *Journal of lightwave Technology*, 19(12), 1924.
- Francois, V., & Laramée, F. (2013). Multicore Fiber Optimization for Application to Chip-to-Chip Optical Interconnects. *Journal of Lightwave Technology*, 31(24), 4022-4028.
- Furusawa, K. (2003). *Development of rare-earth doped microstructured optical fibres*. University of Southampton.
- Future Markets, I. (2013). *The world market for specialty optical fiber and fiber lasers*.
- Gawith, C. B. E., Webb, A. S., Standish, R. J., Sahu, J. K., Adikan, F. R. M., Gates, J. C., & Smith, P. G. R. (2007). *Flat fiber: the flexible format for distributed lab-on-a-chip*. Paper presented at the International Congress on Optics and Optoelectronics.
- Golam Kibria, B. B., J. Paulo Davim. (2017a). *Non-traditional Micromachining Processes*: Springer, Cham.
- Golam Kibria, B. B., J. Paulo Davim. (2017b). *Non-traditional Micromachining Processes: Fundamentals and Applications (Materials Forming, Machining and Tribology)*: Springer, Cham.
- Gu, B., Yin, M.-J., Zhang, A. P., Qian, J.-W., & He, S. (2009). Low-cost high-performance fiber-optic pH sensor based on thin-core fiber modal interferometer. *Optics Express*, 17(25), 22296-22302.

- Gu, B., Yin, M.-J., Zhang, A. P., Qian, J.-W., & He, S. (2011). Fiber-optic metal ion sensor based on thin-core fiber modal interferometer with nanocoating self-assembled via hydrogen bonding. *Sensors and Actuators B: Chemical*, 160(1), 1174-1179.
- Gubbi, J., Buyya, R., Marusic, S., & Palaniswami, M. (2013). Internet of Things (IoT): A vision, architectural elements, and future directions. *Future Generation Computer Systems*, 29(7), 1645-1660.
- Hanafusa, H., Hibino, Y., & Yamamoto, F. (1985). Formation mechanism of drawing-induced E' centers in silica optical fibers. *Journal of Applied Physics*, 58(3), 1356-1361.
- Hayashi, T., Taru, T., Shimakawa, O., Sasaki, T., & Sasaoka, E. (2012, 2012/09/16). *Low-Loss and Large-Aeff Multi-core Fiber for SNR Enhancement*. Paper presented at the European Conference and Exhibition on Optical Communication, Amsterdam.
- Heraeus. Fused silica tubes for fiber production. from https://www.heraeus.com/media/media/hqs/doc_hqs/products_and_solutions_8/optical_fiber/Fiber_Tubes_EN_2018_01.pdf
- Hetherington, G., Jack, K.H. and Kennedy, J. C. . (1964). The viscosity of vitreous silica. *Phys. Chem. Glasses*.
- Holmes, C., Adikan, F. R., Webb, A. S., Gates, J. C., Gawith, C. B., Sahu, J. K., . . . Payne, D. N. (2008, 2008/05/04). *Evanescent Field Sensing in Novel Flat Fiber*.
- Hoskova, S. & Vydra, V. (1999). Measuring the diffusion coefficient of water vapour permeability. *Acta Polytechnica*, 39(3), 33-38.
- Huang, B., Fontaine, N. K., Ryf, R., Guan, B., Leon-Saval, S. G., Shubochkin, R., . . . Li, G. (2015). All-fiber mode-group-selective photonic lantern using graded-index multimode fibers. *Opt Express*, 23(1), 224-234.
- Huang, H., Miura, R. M., & Wylie, J. J. (2008). Optical fiber drawing and dopant transport. *SIAM Journal on Applied Mathematics*, 69(2), 330-347.
- Huang, S., Wang, M., Huang, Y., Cao, R., Li, S., Zou, R., . . . Chen, K. P. (2017, 14-19 May 2017). *Fabrication of lightwave circuits on flat fibers: System-in-fiber*. Paper presented at the 2017 Conference on Lasers and Electro-Optics (CLEO).
- Hunsperger, R. G. (2009). *Integrated optics theory and technology*: Springer.
- IOM3 (2007). New 'flat' optical fiber. *Materials World*.
- Izawa, T., & Sudo, S. (1987). Optical fibers: materials and fabrication. *KTK Scientific Publishers*, 1987, 186.
- Jaluria, Y. (2018). *Manufacture of Optical Fibers: Drawing and Coating Processes*.
- Kalli, K., Riziotis, C., Posporis, A., Markos, C., Koutsides, C., Ambran, S., . . . Smith, P. G. R. (2015). Flat fibre and femtosecond laser technology as a novel photonic

integration platform for optofluidic based biosensing devices and lab-on-chip applications: Current results and future perspectives. *Sensors and Actuators B: Chemical*, 209, 1030-1040.

- Kasap, S. O. (2001). *Optoelectronics and Photonics: Principles and Practices*: Pearson.
- Keck, D. B. (2000). *Optical fiber spans 30 years*, Lightwave Special Reports: PennWell Corporation.
- Keiser, G. (2000). *Optical Fiber Communications* (3rd ed.): McGraw-Hill.
- Keiser, G. (2010). *Optical Fiber Communications* (4th ed.): McGraw-Hill Education.
- Kerbage, C., & Eggleton, B. (2003). Tunable microfluidic optical fiber gratings. *Applied physics letters*, 82(9), 1338-1340.
- Kim, K., Kwak, H. S., & Kim, D. (2012). THE ROLE OF HELIUM/ARGON GAS FLOW IN A GLASS FIBER DRAWING FURNACE. 4(3), 263-270.
- Kim, Y. K., Choi, J. S., Kwak, H. S., & Kim, K. (2017). Numerical modeling and analysis of glass fiber drawing process from large sized silica preform. *Journal of Thermal Science and Technology*, 12(2), JTST0030-JTST0030.
- Kostecki, R., Ebendorff-Heidepriem, H., Warren-Smith, S. C., & Monro, T. M. (2013). Predicting the drawing conditions for Microstructured Optical Fiber fabrication. *Optical Materials Express*, 4(1), 29.
- Kurkjian, C. R., Krause, J. T., & Matthewson, M. J. (1989). Strength and fatigue of silica optical fibers. *Journal of Lightwave Technology*, 7(9), 1360-1370.
- Laegsgaard, J., & Bjarklev, A. (2006). Microstructured Optical Fibers-Fundamentals and Applications. *Journal of the American Ceramic Society*, 89(1), 2-12.
- Lee, S. H., Kim, B. H., Son, D., Jeong, S., Kim, Y., & Han, W.-T. (2015). Effect of Cross-Sectional Structure on Optical Properties of Metal filled Side-Hole Fiber. *Journal of Lightwave Technology*, 1-1.
- Lee, S. H. K., & Jaluria, Y. (1997). Simulation of the transport processes in the neck-down region of a furnace drawn optical fiber. *International Journal of Heat and Mass Transfer*, 40(4), 843-856.
- Leon-Saval, S. G., Fontaine, N. K., Salazar-Gil, J. R., Ercan, B., Ryf, R., & Bland-Hawthorn, J. (2014). Mode-selective photonic lanterns for space-division multiplexing. *Opt Express*, 22(1), 1036-1044.
- Li, Y. P., & Henry, C. H. (1996). Silica-based optical integrated circuits. *IEEE Proceedings - Optoelectronics*, 143(5), 263-280.
- Liu, Z., Bo, F., Wang, L., Tian, F., & Yuan, L. (2011). Integrated fiber Michelson interferometer based on poled hollow twin-core fiber. *Optics Letters*, 36(13), 2435-2437.

- Luzi, G., Epple, P., Scharrer, M., Fujimoto, K., Rauh, C., & Delgado, A. (2011). Comparison Between an Analytical Asymptotic Fiber Drawing Model With Full Navier-Stokes Solution Taking Into Account the Effects of Inner Pressure and Surface Tension. *Journal of Lightwave Technology*, 29(11), 1638-1646.
- Luzi, G., Epple, P., Scharrer, M., Fujimoto, K., Rauh, C., & Delgado, A. (2012). Numerical Solution and Experimental Validation of the Drawing Process of Six-Hole Optical Fibers Including the Effects of Inner Pressure and Surface Tension. *Journal of Lightwave Technology*, 30(9), 1306-1311.
- Lyytikäinen, K., Huntington, S., Carter, A., McNamara, P., Fleming, S., Abramczyk, J., . . . Schötz, G. (2004). Dopant diffusion during optical fibre drawing. *Optics express*, 12(6), 972-977.
- M.R. Shenoy, S. K. K., Ajoy Ghatak and Bishnu P. Pal. (2009). *Fiber optics through experiments*: Viva Books.
- Mach, P., Dolinski, M., Baldwin, K., Rogers, J., Kerbage, C., Windeler, R., & Eggleton, B. (2002). Tunable microfluidic optical fiber. *Applied Physics Letters*, 80(23), 4294-4296.
- Mahdiraji, G. A., Amirkhan, F., Chow, D. M., Kakaie, Z., Yong, P. S., Dambul, K. D., & Adikan, F. R. M. (2014). Multicore Flat Fiber: A New Fabrication Technique. *IEEE Photonics Technology Letters*, 26(19), 1972-1974.
- Mawardi, A., & Pitchumani, R. (2010). Optical Fiber Drawing Process Model Using an Analytical Neck-Down Profile. *IEEE Photonics Journal*, 2(4), 620-629.
- Méndez, A., & Morse, T. F. (2011). *Specialty optical fibers handbook*: Academic Press.
- Mizuno, T., Takara, H., Sano, A., & Miyamoto, Y. (2016). Dense Space-Division Multiplexed Transmission Systems Using Multi-Core and Multi-Mode Fiber. *Journal of Lightwave Technology*, 34(2), 582-592.
- Monat, C., Domachuk, P., & Eggleton, B. (2007). Integrated optofluidics: A new river of light. *Nature photonics*, 1(2), 106.
- Mukundan, H., Anderson, A. S., Grace, W. K., Grace, K. M., Hartman, N., Martinez, J. S., & Swanson, B. I. (2009). Waveguide-based biosensors for pathogen detection. *Sensors*, 9(7), 5783-5809.
- Nagashima, T., Toyokawa, S., Hayashi, T., Morishima, T., Sakuma, H., & Nakanishi, T. (2017, 17-21 Sept. 2017). *Multi-Core Fibre with Concaved Double-D Shape Cross Section*. Paper presented at the 2017 European Conference on Optical Communication (ECOC).
- Nextrom. OFC 20 Fiber Draw Tower. from <http://www.rosendahlnextrom.com/fiber-optics/manufacturing-solutions/telecom-fibers-and-preforms/ofc-20/>
- Nummela, K. B. a. J. (2010). *Large optical fiber drawing furnace developments*. Paper presented at the International Wire and Cable Symposium (59th IWCS).

- O'Sullivan, R. H. a. M. (2009). *Fiber optic measurement techniques*: Elsevier.
- Oh, K., & Paek, U.-C. (2012). *Silica optical fiber technology for devices and components: design, fabrication, and international standards* (Vol. 240): John Wiley & Sons.
- Oh, P. S., McAlarney, J. J., & Nath, D. K. (1983). Effect of Fiber Drawing Tension on Optical and Mechanical Properties of Optical Fiber Waveguides. *Journal of the American Ceramic Society*, 66(5), C-84-C-85.
- Okamoto, K. (2006). *Fundamentals of Optical Waveguides*: Academic Press.
- Owyang, G. H. (1981). *Foundation of optical waveguides*: Edward Arnold.
- Paek, U. (1986). High-speed high-strength fiber drawing. *Journal of Lightwave Technology*, 4(8), 1048-1060.
- Paek, U. (1999). Free drawing and polymer coating of silica glass optical fibers. *Journal of Heat transfer*, 121(4), 774-788.
- Paek, U., & Runk, R. (1978). Physical behavior of the neck-down region during furnace drawing of silica fibers. *Journal of Applied Physics*, 49(8), 4417-4422.
- Pavesi, D. J. L. a. L. (2011). *Silicon Photonics II: Components and Integration*: Springer.
- Payne, D. N., & Gambling, W. A. (1976). A resistance-heated high temperature furnace for drawing silica-based fibres for optical communications. *American Ceramic Society Bulletin*, 55(2), 195-197.
- Poh, S. Y., Mahdiraji, G. A., Sua, Y. M., Amirkhan, F., Tee, D. C., Yeo, K. S., & Adikan, F. R. M. (2017). Single-Mode Operation in Flat Fibers Slab Waveguide via Modal Leakage. *IEEE Photonics Journal*, 9(3), 1-9.
- Ribeiro, V., Karlsson, M., & Andrekson, P. (2017). Parametric amplification with a dual-core fiber. *Optics Express*, 25(6), 6234-6243.
- Rockwell, D. A., Shkunov, V. V., & Marciante, J. R. (2011). Semi-guiding high-aspect-ratio core (SHARC) fiber providing single-mode operation and an ultra-large core area in a compact coilable package. *Optics Express*, 19(15), 14746-14762.
- Russell, P. (2003). Photonic Crystal Fibers. [10.1126/science.1079280]. *Science*, 299(5605), 358.
- Saitoh, K., & Matsuo, S. (2016). Multicore Fiber Technology. *Journal of Lightwave Technology*, 34(1), 55-66.
- Sakaguchi, J., Klaus, W., Mendingueta, J. M. D., Puttnam, B. J., Luis, R. S., Awaji, Y., . . . Kobayashi, T. (2015, 22-26 March 2015). *Realizing a 36-core, 3-mode fiber with 108 spatial channels*. Paper presented at the 2015 Optical Fiber Communications Conference and Exhibition (OFC).

- Sakaguchi, J., Puttnam, B. J., Klaus, W., Awaji, Y., Wada, N., Kanno, A., . . . Watanabe, M. (2013). 305 Tb/s Space Division Multiplexed Transmission Using Homogeneous 19-Core Fiber. *Journal of Lightwave Technology*, 31(4), 554-562.
- Sakamoto, T., Mori, T., Wada, M., Yamamoto, T., Yamamoto, F., & Nakajima, K. (2017). Coupled Few-Mode Multicore Fiber With Low Differential Mode Delay Characteristics. *Journal of Lightwave Technology*, 35(6), 1222-1227.
- Sakamoto, T., Saitoh, K., Saitoh, S., Shibahara, K., Wada, M., Abe, Y., . . . Nakajima, K. (2018). Six-Mode Seven-Core Fiber for Repeated Dense Space-Division Multiplexing Transmission. *Journal of Lightwave Technology*, 36(5), 1226-1232.
- Saleh, B. E., & Teich, M. C. (1991). *Fundamentals of photonics* (Vol. 22): Wiley New York.
- Saleh, B. E., & Teich, M. C. (2007). Semiconductor photon detectors. *Fundamentals of Photonics*, 644-695.
- Samir, Perpar, & Batagelj. (2016). *Fabrication of a single-mode seven-core optical fiber using the stack-and-draw procedure*. Paper presented at the 2016 International Workshop on Fiber Optics in Access Network (FOAN), Lisbon, Portugal.
- Samir, A., & Batagelj, B. (2016). *Seven-core optical fiber design and fabrication for space-division multiplexing optimized for low crosstalk*. Paper presented at the 2016 18th International Conference on Transparent Optical Networks (ICTON), Italy.
- Satoshi Kamo, T. S., Tetsuo Katsuta and Takahiko Kurosawa. (2006). *The effect of the fiber temperature during fiber drawing on the properties of primary coatings*. Paper presented at the International Wire and Cable Symposium (55th IWCS).
- Schartner, E. P., Tsiminis, G., François, A., Kostecki, R., Warren-Smith, S. C., Nguyen, L. V., . . . Monroe, T. M. (2015). Taming the Light in Microstructured Optical Fibers for Sensing. *International Journal of Applied Glass Science*, 6(3), 229-239.
- Schmidt, H., & Hawkins, A. R. (2011). The photonic integration of non-solid media using optofluidics. *Nature photonics*, 5(10), 598.
- Senior, J. M., & Jamro, M. Y. (2009). *Optical fiber communications: principles and practice*: Pearson Education.
- Shao, M., Qiao, X., Fu, H., Li, H., Jia, Z., & Zhou, H. (2014). Refractive Index Sensing of SMS Fiber Structure Based Mach-Zehnder Interferometer. *IEEE Photonics Technology Letters*, 26(5), 437-439.
- Shelby, J. E. (2005). *Introduction to Glass Science and Technology*: RSC.
- Singh, J. (1996). *Optoelectronics: An introduction to materials and devices*: McGraw-Hill College.
- Skutnik, B. J. (1989). How coating/polymer properties affect fiber/cable performance. *Polymer Engineering & Science*, 29(17), 1159-1164.

- Smith, A. S. W., Christopher, H., Corin, B. G., David, N. P., Adikan, F. R., James, C. G., . . . Peter, G. (2008). Evanescent Field Sensing in Novel Flat Fiber. *Conference on Lasers and Electro-Optics/Quantum Electronics and Laser Science Conference and Photonic Applications Systems Technologies (2008)*, paper CMJJ3.
- Soma, D., Wakayama, Y., Beppu, S., Sumita, S., Tsuritani, T., Hayashi, T., . . . Suzuki, M. (2018). 10.16-Peta-B/s Dense SDM/WDM Transmission Over 6-Mode 19-Core Fiber Across the C+L Band. *Journal of Lightwave Technology*, 36(6), 1362-1368.
- Stone, J. M., Yu, F., & Knight, J. C. (2014). Highly birefringent 98-core fiber. *Opt Lett*, 39(15), 4568-4570.
- Sugioka, K., & Cheng, Y. (2014). Femtosecond laser three-dimensional micro- and nanofabrication. *Applied Physics Reviews*, 1(4), 041303.
- Suzanne R. Nagel, J. B. M., Kenneth L. Walker. (1982). An Overview of the Modified Chemical Vapor Deposition (MCVD) Process and Performance. *IEEE Transactions on Microwave Theory and Techniques*, MTT-30.
- Tajima, K., Tateda, M., & Ohashi, M. (1994). Viscosity of GeO/sub 2/-doped silica glasses. *Journal of lightwave technology*, 12(3), 411-414.
- Takara, H., Sano, A., Kobayashi, T., Kubota, H., Kawakami, H., Matsuura, A., . . . Shikama, K. (2012). 1.01-Pb/s (12 SDM/222 WDM/456 Gb/s) crosstalk-managed transmission with 91.4-b/s/Hz aggregate spectral efficiency. Paper presented at the European Conference and Exhibition on Optical Communication.
- Thomson, R., Campbell, S., Blewett, I., Kar, A., & Reid, D. (2006). Optical waveguide fabrication in z-cut lithium niobate (LiNbO₃) using femtosecond pulses in the low repetition rate regime. *Applied Physics Letters*, 88(11), 111109.
- Thomson, R. R., Bookey, H. T., Psaila, N., Campbell, S., Reid, D. T., Shen, S., . . . Kar, A. K. (2006). Internal gain from an erbium-doped oxyfluoride-silicate glass waveguide fabricated using femtosecond waveguide inscription. *IEEE Photonics Technology Letters*, 18(14), 1515-1517.
- Vallée, R., & Drolet, D. (1994). Practical coupling device based on a two-core optical fiber. *Applied Optics*, 33(24), 5602-5610.
- Vallee, R., & He, G. (1993). Polarizing properties of a high index birefringent waveguide on top of a polished fiber coupler. *Journal of lightwave technology*, 11(7), 1196-1203.
- Vaskopoulos, T., Polymeropoulos, C., & Zebib, A. (1995). Cooling of optical fiber in aiding and opposing forced gas flow. *International Journal of Heat and Mass Transfer*, 38(11), 1933-1944.
- Voyce, C. J., Fitt, A. D., Hayes, J. R., & Monroe, T. M. (2009). Mathematical Modeling of the Self-Pressurizing Mechanism for Microstructured Fiber Drawing. *Journal of Lightwave Technology*, 27(7), 871-878.

- Voyce, C. J., Fitt, A. D., & Monro, T. M. (2004). Mathematical model of the spinning of microstructured fibres. *Optics Express*, 12(23), 5810-5820.
- Watts, S. P. (2002). *Flame hydrolysis deposition of photosensitive silicate layers suitable for the definition of waveguiding structures through direct ultraviolet writing*. University of Southampton.
- Webb, A. (2012). *Novel optical fibre fabrication techniques for Yb-doped high-power fibre lasers and sensing applications*. University of Southampton.
- Webb, A., Adikan, F. M., Sahu, J., Standish, R., Gawith, C., Gates, J., . . . Payne, D. (2007). MCVD planar substrates for UV-written waveguide devices. *Electronics Letters*, 43(9), 517-519.
- Wei, Z., Lee, K.-M., Tchikanda, S. W., Zhou, Z., & Hong, S.-P. (2004). Free Surface Flow in High Speed Fiber Drawing With Large-Diameter Glass Preforms. *Journal of Heat Transfer*, 126(5), 713.
- Wu, Y., & Chiang, K. S. (2016). Mode-selective coupling between few-mode fibers and buried channel waveguides. *Optics Express*, 24(26), 30108-30123.
- Xia, T.-H., Zhang, A. P., Gu, B., & Zhu, J.-J. (2010). Fiber-optic refractive-index sensors based on transmissive and reflective thin-core fiber modal interferometers. *Optics Communications*, 283(10), 2136-2139.
- Xue, S., Barton, G. W., Fleming, S., & Argyros, A. (2017). Analysis of Capillary Instability in Metamaterials Fabrication Using Fiber Drawing Technology. *Journal of Lightwave Technology*, 35(11), 2167-2174.
- Xue, S., Tanner, R., Barton, G., Lwin, R., Large, M., & Poladian, L. (2005). Fabrication of microstructured optical fibers-Part II: Numerical modeling of steady-state draw process. *Journal of Lightwave Technology*, 23(7), 2255.
- Xue, S. C., Large, M. C. J., Barton, G. W., Tanner, R. I., Poladian, L., & Lwin, R. (2006). Role of material properties and drawing conditions in the fabrication of microstructured optical fibers. *Journal of Lightwave Technology*, 24(2), 853-860.
- Xue, S. C., Poladian, L., Barton, G. W., & Large, M. C. J. (2007). Radiative heat transfer in preforms for microstructured optical fibres. *International Journal of Heat and Mass Transfer*, 50(7-8), 1569-1576.
- Xue, S. C., Tanner, R., Barton, G., Lwin, R., Large, M., & Poladian, L. (2005). Fabrication of microstructured optical fibers-Part I: Problem formulation and numerical modeling of transient draw process. *Journal of Lightwave Technology*, 23(7), 2245.
- Yan, Y., & Pitchumani, R. (2006). Numerical study on the dopant concentration and refractive index profile evolution in an optical fiber manufacturing process. *International Journal of Heat and Mass Transfer*, 49(13-14), 2097-2112.

- Yang, J., & Jaluria, Y. (2009a). Feasibility and optimization of the hollow optical fiber drawing process. *International Journal of Heat and Mass Transfer*, 52(17-18), 4108-4116.
- Yang, J., & Jaluria, Y. (2009b). Transport Processes Governing the Drawing of a Hollow Optical Fiber. *Journal of Heat Transfer*, 131(7), 072102-072102-072109.
- Yin, Z., & Jaluria, Y. (2000). Neck down and thermally induced defects in high-speed optical fiber drawing. *Journal of heat transfer*, 122(2), 351-362.
- Yoo, S.-Y., & Jaluria, Y. (2006). Fluid flow and heat transfer in an optical fiber coating process. *International Journal of Heat and Mass Transfer*, 50(5-6), 1176-1185.
- Zhou, H., Wang, F., Li, B., Tang, M., & Xin, X. (2016). Performance analysis of optical transmission based on seven cores fiber. *China Communications*, 13(9), 113-120.
- Zhu, B., Taunay, T., Fishteyn, M., Liu, X., Chandrasekhar, S., Yan, M., . . . Dimarcello, F. (2011). 112-Tb/s space-division multiplexed DWDM transmission with 14-b/s/Hz aggregate spectral efficiency over a 76.8-km seven-core fiber. *Optics Express*, 19(17), 16665-16671.
- Zhu, B., Taunay, T. F., Yan, M. F., Fishteyn, M., Oulundsen, G., & Vaidya, D. (2010). 70-Gb/s Multicore Multimode Fiber Transmissions for Optical Data Links. *IEEE Photonics Technology Letters*, 22(22), 1647-1649.
- Zhu, J.-J., Zhang, A. P., Xia, T.-H., He, S., & Xue, W. (2010). Fiber-optic high-temperature sensor based on thin-core fiber modal interferometer. *IEEE Sensors Journal*, 10(9), 1415-1418.

LIST OF PATENTS, AWARDS, PUBLICATIONS AND PAPERS PRESENTED

A. Patents Granted

1. “Apparatus and Method of Fabricating Flat Microstructured Fiber”, Seyed Reza Sandoghchi, Nizam Tamchek, Desmond Chow Ming Chia, **Katrina D. Dambul** and Faisal Rafiq Mahamd Adikan, Grant No: MY-163092.
2. “Apparatus for Mounting Capillary”, Seyed Reza Sandoghchi, Nizam Tamchek, Desmond Chow Ming Chia, **Katrina D. Dambul** and Faisal Rafiq Mahamd Adikan, Grant No: MY-163093-A.

B. Awards

1. Gold Medal in I-Innova 2014 for Multicore Flat Fiber.
2. ASM Innovation Award in I-Innova 2014 for Multicore Flat Fiber.

C. Journal Publication

1. **K.D. Dambul**, G.A. Mahdiraji, N. Tamchek, M.F. Azman, W.R. Wong and F.R. Mahamd Adikan, “Simple fabrication technique for novel multistructured flat fibers” (*Submitted*).
2. **K.D. Dambul**, N. Tamchek, G.A. Mahdiraji and F.R. Mahamd Adikan, “Dual stage drawing for fabrication of micron-sized flat fibers” (*Submitted*).
3. **K.D. Dambul**, S.Y. Poh, N. Tamchek, D.C. Tee, F. Amirkhan, K.S. Yeo, G.A. Mahdiraji, W.R. Wong and F.R. Mahamd Adikan, “Fabrication and characterization of Ge-doped flat fibers” (*Submitted*).
4. **K.D. Dambul**, G.A. Mahdiraji, N. Tamchek, M.F. Azman, W.R. Wong and F.R. Mahamd Adikan, “Effect of vacuum pressure on the shape of a flat fiber,” (*Submitted*).
5. G. A. Mahdiraji, F. Amirkhan, D. M. Chow, Z. Kakaie, P. S. Yong, **K.D. Dambul** and F.R. Mahamd Adikan, “Multicore flat fiber: a new fabrication technique,” *IEEE Photonics Technology Letters* 26, (19), 1972-1974.

D. Papers Presented at Conferences

1. **K.D. Dambul**, N. Tamchek, S.R. Sandoghchi, M.R. Abu Hassan, D.C. Tee and F.R. Mahamd Adikan, “Fabrication and characterization of Flat

Fibers”, 2011 IEEE 2nd International Conference on Photonics (ICP 2011), 01 October, 2011, Sabah.

2. **K.D. Dambul**, G. A. Mahdiraji, F. Amirkhan, D. M. Chow, Gabriel K.W. Gan, W.R. Wong, M.R. Abu Hassan, Sarahah Ismail, S.A. Ibrahim, N. Tamchek and F.R. Mahamd Adikan, “Fabrication and development of Flat Fibers”, Photonics Global Conference (PGC 2012), 13-16 December, 2012, Singapore.
3. G. A. Mahdiraji, F. Amirkhan, **K. D. Dambul**, P. S. Yong, K. S. Yeo and F. R. M. Adikan, “Low-crosstalk semi-trench-assisted multicore flat fiber,” Optical Fiber Communication Conference and Exhibition (OFC), Los Angeles, CA, USA, 22-26 March 2015.

E. Book Chapter

1. Flat Fibers: Fabrication and modal characterization, G. A. Mahdiraji, **K. D. Dambul**, P. S. Yong, and F. R. M. Adikan (*Submitted*).